UNIVERSITÀ DEGLI STUDI DI MILANO

SCUOLA DI DOTTORATO
Scienze e tecnologie chimiche

DIPARTIMENTO
Chimica fisica ed elettrochimica

CORSO DI DOTTORATO
Chimica Industriale

TESI DI DOTTORATO DI RICERCA

Diffraction Studies on Strongly Correlated Perovskite Oxides

DOTTORANDO
Mattia Allieta

TUTOR
Dr. Marco Scavini

COORDINATORE DEL DOTTORATO
Prof. Dominique Roberto

A.A. 2010/2011

Abstract

Diffraction Studies on Strongly Correlated Perovskite Oxides

by

Mattia Allieta

In recent years, a great interest has been devoted to the so called strongly correlated systems containing perovskite building blocks. These systems exhibit a complex interplay between charge, spin, orbital and lattice degrees of freedom paving the way for very attractive applications.

In this work, entitled "*Diffraction Studies on Strongly Correlated Perovskite Oxides*" the use of x-ray diffraction techniques to investigate the coupling between the structure and the physical properties of several bulk material based on perovskite structure is presented.

The thesis is organized in five chapters. Introduction presents a very general overview on strongly correlated perovskite oxides and the scope of the thesis. The first chapter reports technical details of the diffraction techniques involved in all the structural studies performed during the PhD.

Chapter 2 reports an accurate investigation performed on the magnetoresistive cobaltite $GdBaCo_2O_{5+\delta}$ (δ=0) using single-crystal and synchrotron powder X-ray diffraction. In this work, we assign the correct space group and we demonstrate that a very small tetragonal-to-orthorhombic lattice distortion is coupled to magnetic phase transition. In Chapter 3, we show the study of the temperature induced insulator-to-metal transition for $GdBaCo_2O_{5+\delta}$ (δ>0.5). By using a combined approach between electron

paramagnetic resonance and powder diffraction techniques we provide new interesting features about the spin – lattice interaction occurring in these systems. Chapter 4 presents synchrotron X-ray powder diffraction study on $EuTiO_3$ system. We show for the first time the existence of a new structural phase transition occurring in $EuTiO_3$ below room temperature. In addition, by performing the atomic pair distribution function analysis of the powder diffraction data, we provide evidence of a mismatch between the local (short-range) and the average crystallographic structures in this material and we propose that the lattice disorder is of fundamental importance to understand the $EuTiO_3$ properties. Finally, beyond the scope of the thesis, in Chapter 5, we review the basic procedure to get the differential pair distribution function obtained by applying the anomalous X-ray diffraction technique to total X- ray scattering method. We show an example of the application of this procedure by presenting the case of gadolinium doped ceria electrolytes.

This work will show that use of the powder diffraction techniques provides a powerful tool to unveil the coupling between the structure and the physical properties in strongly correlated perovskite oxides.

Acknowledgements

Over the course of my PhD, I have been fortunate to work with very extraordinary people. My supervisor Marco Scavini for introducing me to the fascinating world of diffraction and for being an advisor and a dear friend. My close colleague and friend Mauro Coduri for everything. My friends of many experiments Paolo Masala, Daniele Briguglio, Claudio Mazzoli, and Valerio Scagnoli. All the people at the University of Milano and Pavia: Serena Cappelli, Cesare Biffi, Ilenia Rossetti, Leonardo Lo Presti, Cesare Oliva, Laura Loconte, Paolo Ghigna, Monica Dapiaggi, and Alessandro Lascialfari. My supervisor at the ILL Michela Brunelli and all the people at ESRF Claudio Ferrero, Loredana Erra, Andy Fitch, Dmitry Chernyshov and Phil Pattison. The people that I met during my stage at the reactor of Grenoble: Mark Sigrist, Annalisa Boscaino, Adrian Hill, Jad Kozaily and Andrew Jones. I am especially grateful to Ekaterina Pomjakushina from Paul Scherrer Institut for her contribution to my thesis. Last but not least I would you like to thank my entire family: my parents, my brothers and my uncles and aunts for their support throughout the years.

Finally, I would like to thank Monica, my wife, and Laue, my little cat, for bearing with me and for being who they are: my new family.

To my grandfather Gigi

Contents

Introduction

Since the pioneered work of Mott,[1] that recognized the electron-electron interactions as the origin for the insulating behavior of many class of transition oxides, the research in condensed matter physics has shown the properties of a new class of materials called the strongly correlated electronic systems.

Strongly correlated electronic systems are a class of compounds where the effect of correlations among electrons plays a central role in such a way that the theoretical approaches based on the perturbative methods fail to describe even their very basic properties.[2] In this prospective the current status of correlated electrons investigations must be considered in the broader context of complexity.[2]

The main aspects of this complexity can be represented by: the competition between different phases; the stable phase is generally not homogeneous.[3] In particular, the phase competition implies that the systems form spontaneously complex structure and these structures vary in size and scales.[3] This leads to very complicated and rich phase diagrams where, in many cases, the average behavior of the structures involved have no relevance and the physics is dominated by the local spatial correlation. Hence, these materials can be considered *intrinsically inhomogeneous* explaining why the early theories methods based on homogenous systems were not successful.[3] The phase competition can arise also from the correlation between the degrees of freedom of the system. In particular, in many cases the crystal field splitting and the intra-atomic exchange interaction energy scales are close in value. This implies delicate balance of interactions between these contributions giving rise to a complex interplay between charge, spin, orbital and lattice degrees of freedom which is the driving force of many interesting phenomena.

This competition between different kinds of order involving charge, orbital, lattice, and spin degrees of freedom has dramatically challenged the ways to study the solids. In particular, over the last decades, the largest research efforts have been devoted to study the properties of one class of strongly correlated electronic systems: the oxides containing perovskite building blocks.

These systems exhibit a wide variety of interesting physical properties ranged from the intriguing high-T_c superconductivity to the well-known ferroelectricity.

We believe that in the last ten years of research on strongly correlated perovskite oxides, two main effects have attracted a lot of interest: the magnetoresistance (MR) and the quantum paraelectric or incipient ferroelectric effects.

MR is the property of a material to decrease its electrical resistivity when its magnetic moments order ferromagnetically either by lowering temperature or by applying weak magnetic field. This huge increase in the carrier mobility is both of scientific and technological interest. In particular the "half-metallic" behaviour associated with the MR effect could provide fully spin polarized electrons for use in "spintronics" applications, for sensors, and for read/write heads for the magnetic data storage industry.

The MR effect in perovskite-like material was discovered by R. von Helmolt *et al.*,[4] by measuring the resistivity as a function of temperature at different applied magnetic field on $La_{2/3}Ba_{1/3}MnO_3$ film. Later it has been found that the MR effect was a peculiar property of a broader set of bulk compounds called manganites, i.e. $La_{1-x}A_xMnO_3$ (A = Ca, Sr and Ba). The electronic transport in manganites is directly connected to the magnetic system through the double exchange mechanism, while the Jahn-Teller distortion couples the magnetic and lattice systems. Hence, the electronic, lattice and magnetic degrees of freedom being intimately intertwined and for these reasons in

general these compounds are very difficult for understanding. Thus, in this last decade, the research expanded towards other MR perovskites such as the layered cobalt oxides $R\mathrm{BaCo_2O_{5+\delta}}$ (R= lanthanoids).[5]

For many years the $\mathrm{ATiO_3}$ (A=metal transition ions or lanthanoids) ferroelectrics perovskite has been considered as the model systems for understanding the physics of soft phonon mode driven structural phase transitions in solids.[6] As an example in $\mathrm{BaTiO_3}$ or $\mathrm{PbTiO_3}$ perovksite is well established that the condensation of the polar mode at q=0 gives rise to the ferroelectric transition below the critical temperature.[6] On the contrary for $\mathrm{SrTiO_3}$ the condensation of polar soft mode never takes place down to lowest temperature resulting in a stabilized paraelectrics ground state even at T=0K.[7] Since in this state the fluctuations of wave vector q=0 are in same way quantum mechanically stabilized, the resulting ground state is called *quantum paraelectric*.[7] The *quantum paraelectric* state or Muller state, can be however perturbed on application of external electric field, magnetic field, or chemical substitutions giving rise to fascinating phenomena such as magnetoelectric and relaxor ferroelectrics effects. In particular, magnetoelectric materials are of fundamental interest since they present interplay of spin, optical phonons and strain, paving the way to attractive spintronics applications. In this context, the perovskite $\mathrm{EuTiO_3}$ has been widely considered as a model system for its unique property to be the only known quantum paraelectric material with a magnetic transition.

As already described above, the phase competition as well as the correlation of the different degrees of freedom gives rise to some kind of inhomogeneous phase in strongly correlated material. We consider the structure of the inhomogeneous phase as the result of a comprise between competing phases. These phases may or may not have different electronic density, but they usually have different symmetry breaking patterns.

Thus, the structural symmetry governs a number of the intensive physical properties and, as a precursor stage, it is mandatory to have a complete understanding of the structure of the phases involved.

Single crystal and powder diffraction techniques are applied to obtain information about the average structure and its behavior under chemical or physical pressures. On the other hand, there is growing evidence that the inhomogeneous phases can be characterized by nanoscale phase-separation or local deviations with respect to the average structural information. The recent development in pair distribution function treatment of powder diffraction data can fill the lacks of conventional diffraction techniques by providing structural information at different spatial scales.

The scope of this thesis is to show the use of diffraction techniques to investigate the structure and its coupling with physical properties of strongly correlated systems based on perovskitic structure. We considered the MR perovskite $GdBaCo_2O_{5+\delta}$ and the quantum paraelectric $EuTiO_3$. The former system is a model system for studying competing magnetic interactions and MR phenomenon while the latter has attracted a lot of interest for its magnetic-field-induced polarization property. Surprisingly, despite the very complete works dedicated to study the transport and the magnetic property of these materials, only few works about their structures are present in the literature. For example the most cited work reporting the temperature evolution of $EuTiO_3$ crystal structure is the paper of J. Brous *et al.* published on 1953.[8] In this work, which seems to be the only paper on the topic, the diffraction measurements were performed with the lab x-ray source available in the 50s.

As learned from the previous analysis on manganites, the radiation source could be fundamental to carefully study the structure of this material using diffraction techniques. Indeed, for example the structural phase transitions in perovskite are mainly

caused by periodic oxygen ions displacements. In order to detect both the splitting of diffraction peaks and/or the small superstructure peaks which should grow up in correspondence of phase transitions, a very high photon flux and angular resolution are needed. Nowadays, both neutron or synchrotron radiation facilities are available to this end but the high absorption of neutrons both by natural Gadolinium and Europium precludes carefully neutron diffraction investigations. Hence, all the powder diffraction experiments presented in this thesis were performed using the powder diffraction beamline of the European Synchrotron Radiation Facility (ESRF).

References

[1] N. F. Mott, Proc. Phys. Soc. London A **62**, 416 (1949).

[2] E. Dagotto, Science **309**, 257 (2005).

[3] E. Dagotto, in Nanoscale Phase Separation and Colossal Magnetoresistance, Springer (2003)

[4] R. von Helmolt, J. Wecker, B. Holzapfel, L. Schultz, and K. Samwer, Phys. Rev. Lett. **71**, 2331 (1993).

[5] A. A. Taskin, A. N. Lavrov, and Yoichi Ando, Phys. Rev. B **71**, 134414 (2005).

[6] J. F. Scott, Rev. Mod. Phys. **46**, 83 (1974).

[7] K. A. Muller, H. Burkard, Phys. Rev. B **19**, 3593 (1979).

[8] J. Brous, I. Fankuchen, and E. Banks, Acta Cryst. **6**, 67 (1953).

1. Diffraction: Theory and Practice

In this Chapter the basic concepts related to the X-ray diffraction techniques used in the thesis are presented. Our purpose is to show only the theoretical and practical aspects useful for this work. Hence, since in this thesis we deal mainly with powder diffraction, we will not give details about single crystal technique. For further background on this topic we suggest the book.[1]

In the first paragraph a very general overview on the diffraction theory as well as powder diffraction technique is given mostly following the book.[2] Last section presents the pair distribution function together with the procedure to analyze the diffuse scattering from the powder diffraction data.

1.1 Diffraction theory: the reciprocal space

X-rays are electromagnetic radiation with a wavelength (λ) placed between the ultraviolet region and the region of γ-rays emitted by radioactive substances. The λ is ranged from 0.1-10Å, which are the typical interatomic distances values. This makes the X-rays radiation an ideal probe to study the crystal structure of materials.

Let us now imagine that a particle with electric charge and mass, e.g. an electron, is placed in the electromagnetic field of a plane monochromatic X-ray beam. The particle will start to oscillate with the same frequency of the electric field of the radiation and, because of the acceleration of the particle, will start to emit radiation through a so called *scattering process*. We can represent this phenomenon elementarily in Fig.1.1 by sitting the particle at the origin *O* of our coordinates system.

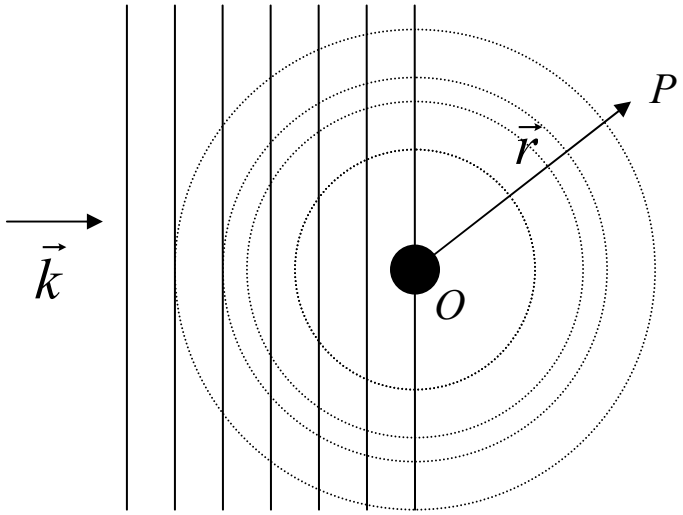

.

FIG.1.1 *Scattering of plane wave from point O to point P (identified by $\vec{r}$). The phase of the incident wave is assumed to be zero at the origin O.*

In this scattering process the amplitude of the diffused wave in *P* is proportional to the amplitude of the incident wave in *O*. Hence, the amplitude of the outcoming wave from $\vec{r}$ can be then written as:

$$A\frac{\exp(2\pi i\vec{k}\cdot\vec{r})}{r} \qquad (1.1)$$

The wave vector $\vec{k}$ has the direction of propagated wave and modulus $2\pi/\lambda$.

The *A* factor depends on the scattering phenomena and is related to the interaction potential and the angle Φ from the incident ($\vec{k}$) and diffusion ($\vec{r}$) directions. When the X-rays are scattered elastically without any loss of energy, the scattering amplitude is given by the Thompson formula:

$$A = \left(\frac{e^4}{m^2 c^4} \right) \frac{1 + \cos^2 \Phi}{2} \tag{1.2}$$

where $P=(1+\cos^2\Phi)/2$ is called the *polarization factor* and it suggests that the scattered radiation is maximum in the direction of the incident beam while it is minimum when perpendicular to it.

On the other hand, when some energy of the incident beam is lost to the crystal we have Compton scattering. In this case the incident beam is deflected by a collision from its original direction and transfers a part of its energy to the electron.[1] There is a difference in λ between the incident and the scattered radiation which can be calculated by:

$$\Delta\lambda = \frac{h}{m_e c}\left(1 - \cos 2\theta\right) \tag{1.3}$$

where h is the Planck constant, m_e is the rest mass of the electron, c is the speed of light and 2θ is the scattering angle.

From equation (1.3) emerges that $\Delta\lambda$ does not depend on the λ of the incident radiation and the maximum value of $\Delta\lambda$ is reached for $2\theta=\pi$, i.e. backcattering condition. Another important feature is that the Compton scattering is incoherent because it does not involve a phase relation between the incident and scattered radiation.

It should be noted that here we are not interested in the wave propagation processes, but only in the diffraction patterns produced by the interaction between radiation and system of atoms. Hence, let us assume a system of atoms where two scattering centers are located at *O* and at *O*' as shown in Fig.1.2.

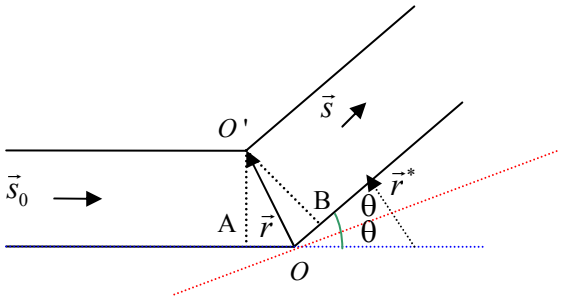

FIG.1.2 *Schematic representation of two scattering points phenomenon.*

Let $\vec{s}_0$ and $\vec{s}$ be the unit vectors associated with the scattered waves. The phase difference between the waves scattered by *O*' and *O* reads as:

$$\phi = \frac{2\pi}{\lambda}(\vec{s} - \vec{s}_0)\cdot\vec{r} = 2\pi\vec{r}^*\cdot\vec{r} \tag{1.4}$$

where $\vec{r}^* = \frac{1}{\lambda}(\vec{s} - \vec{s}_0)$ is a vector of the so called reciprocal space.

The modulus of $\vec{r}^*$ can be derived from Fig.1.2 as:

$$\vec{r}^* = 2\sin\theta/\lambda \tag{1.5}$$

where 2θ is the angle between the direction of incident X-rays and the direction of observation.

By considering A_O the amplitude of the wave scattered by the point *O*, the wave scattered by the *O*' is given by $A_{O'}\exp(2\pi i\vec{r}^*\cdot\vec{r})$. Hence, if there are *N* point scatters in the material, we can easily express the total amplitude of the scattered wave from these points as:

$$F(\vec{r}^*) = \sum_{j=1}^{N} A_j \exp(2\pi i \vec{r}^* \cdot \vec{r}_j) \tag{1.6}$$

where A_j stands for the amplitude of the wave scattered by the j^{th} point.

Dealing with atoms, we have to consider an ensemble of scattering centers which constitutes a continuum. We can then define an element of volume $d\vec{r}$ containing a number of scatters equal to $\rho(\vec{r})d\vec{r}$.

According to equation (1.7), the total amplitude of the scattered wave will be:

$$F(\vec{r}^*) = \int_V \rho(\vec{r}) \exp(2\pi i \vec{r}^* \cdot \vec{r}\,) d\vec{r} \tag{1.7}$$

Hence, the amplitude $F(\vec{r}^*)$ is the Fourier Transform (*FT*) of the $\rho(\vec{r})$ function and, for an atom, the *FT* of $\rho(\vec{r})$ is the atomic scattering factor denoted as *f* which defines the electron density. *V* is region of the space in which the probability of finding the electron is different from zero.

Generally the function $\rho(\vec{r})$ does not have spherical symmetry but for many crystallographic applications the deviations from it can be neglected by writing the scattering factor as:

$$f(r^*) = 4\pi \int_0^{\infty} r^2 \rho(r) \frac{\sin(2\pi r^* r)}{2\pi r^* r} dr \tag{1.8}$$

The $\rho(r)$ function can be calculated theoretically using Hartree-Fock methods or Thomas-Fermi approximation for heavier atoms.

Figure 1.3 reports $f(r^*)$ calculated for some atoms. The profile shows a maximum, equal to Z, at $\sin\theta/\lambda = 0$ and decreases with increasing $\sin\theta/\lambda$.

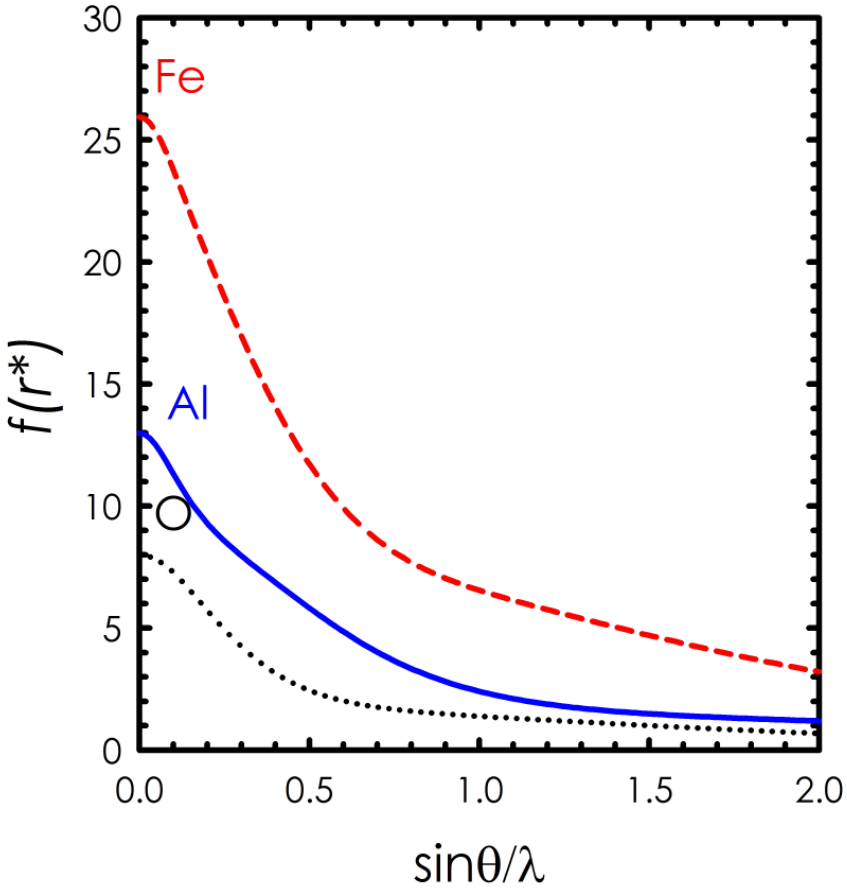

FIG.1.3 *Atomic scattering factors for Fe, Al and O.*[3]

Up to now, we introduced the concepts related to scattering from a general arrangement of atoms. Since most of the crystallographic problems are related to periodic three dimensional arrangements of atoms, we introduce periodicity. In this context, we define a *crystal* as a periodic three-dimensional arrangement of atoms. The crystal structure can be then described by a *lattice* which can fill all the space (direct space) by the

elementary translation vectors $\vec{a}_1, \vec{a}_2, \vec{a}_3$ of the so called unit cell. Associated to *L*, a second lattice can be always defined by the translation vectors $\vec{a}_1^{\,*}$, $\vec{a}_2^{\,*}$, $\vec{a}_3^{\,*}$ which satisfy the conditions:

$$\vec{a}_i \cdot \vec{a}_j^{\,*} = 2\pi\delta_{ij} \tag{1.9}$$

where $\delta_{ij} = 1$ if $i = j$ and $\delta_{ij} = 0$ if $i \neq j$.

This new space is the reciprocal space and is related to the direct space by the following equations:

$$\vec{a}_1^{\,*} = 2\pi \frac{\vec{a}_2 \wedge \vec{a}_3}{\vec{a}_1 \cdot \vec{a}_2 \wedge \vec{a}_3}$$

$$\vec{a}_2^{\,*} = 2\pi \frac{\vec{a}_3 \wedge \vec{a}_1}{\vec{a}_1 \cdot \vec{a}_2 \wedge \vec{a}_3} \tag{1.10}$$

$$\vec{a}_3^{\,*} = 2\pi \frac{\vec{a}_1 \wedge \vec{a}_2}{\vec{a}_1 \cdot \vec{a}_2 \wedge \vec{a}_3}$$

Finally, every point belonging to reciprocal lattice can be defined by a vector:

$$\vec{r}_H^{\,*} = h\vec{a}_1^{\,*} + k\vec{a}_2^{\,*} + l\vec{a}_3^{\,*} \tag{1.11}$$

where the *h*, *k*, *l* are integers.

These integers are called the Miller indices and they are both used in the reciprocal and in direct spaces to identify the family of crystallographic planes.

1.2 Scattering from a lattice: Diffraction condition

The three dimensional lattice defined by the unit vectors $\vec{a}_1, \vec{a}_2, \vec{a}_3$ can be represented by the so called lattice function:

$$L(\vec{r}) = \sum_{u,v,w=-\infty}^{\infty} \delta(\vec{r} - \vec{r}_{u,v,w}) \tag{1.12}$$

where δ is the Dirac delta function and $\vec{r}_{u,v,w} = u\vec{a}_1 + v\vec{a}_2 + w\vec{a}_3$ is a vector which defined points belonging to direct lattice. If we define $\rho_M(\vec{r})$ as the electron density in the unit cell of an infinite three-dimensional crystal, the electron density function in the whole crystal can described by the convolution of the $L(\vec{r})$ with $\rho_M(\vec{r})$:

$$\rho_L(\vec{r}) = \rho_M(\vec{r}) \otimes L(\vec{r}) \tag{1.13}$$

According to equation (1.7), to obtain the amplitude of the wave scattered by the whole crystal, we apply the *FT* operator to $\rho_L(\vec{r})$:

$$FT\left[\rho_L(\vec{r})\right] = FT\left[\rho_M(\vec{r}) \otimes L(\vec{r})\right] = FT\left[\rho_M(\vec{r})\right] \cdot FT\left[L(\vec{r})\right] \tag{1.14}$$

$FT\left[\rho_M(\vec{r})\right]$ coincides with the amplitude of the scattered wave related to one unit cell containing *N* atoms and it can be expressed as:

$$FT\left[\rho_M(\vec{r})\right] = F_M(\vec{r}^*) = \sum_{j=1}^{N} f_j(\vec{r}^*) \exp(2\pi i \vec{r}^* \cdot \vec{r}_j) \tag{1.15}$$

Considering that the FT of a lattice in direct space is the function $L(\vec{r}^{\,*})/V$ in the reciprocal space, $FT\left[L(\vec{r})\right]$ reads as:

$$FT\left[L(\vec{r})\right]=\frac{1}{V}\sum_{h,k,l=-\infty}^{+\infty}\delta(\vec{r}^{\,*}-\vec{r}_H^{\,*}) \tag{1.16}$$

Then from equation (1.14) results:

$$F_L(\vec{r})=F_M(\vec{r}^{\,*})\frac{1}{V}\sum_{h,k,l=-\infty}^{+\infty}\delta(\vec{r}^{\,*}-\vec{r}_H^{\,*}) \tag{1.17}$$

where V is the volume of the unit cell and $\vec{r}_H^{\,*}$ is defined by equation (1.11).

From equation (1.17) we derive that if the scatter object is periodic like a crystal, we observe a non-zero $F_L(\vec{r})$ only when:

$$\vec{r}^{\,*}=\vec{r}_H^{\,*} \tag{1.18}$$

In addition, by considering the definition (1.4), from the scalar product of equation (1.19) by $\vec{a}_1,\vec{a}_2,\vec{a}_3$ we obtain:

$$\begin{aligned}\vec{a}_1\cdot(\vec{s}\ -\vec{s}_0)&=h\lambda\\ \vec{a}_2\cdot(\vec{s}\ -\vec{s}_0)&=k\lambda\\ \vec{a}_3\cdot(\vec{s}\ -\vec{s}_0)&=l\lambda\end{aligned} \tag{1.19}$$

The equations (1.19) are the so called *Laue diffraction* conditions.

A qualitatively more simple method to obtain the diffraction condition was proposed by W. L. Bragg.[4] In his description, the diffraction is viewed as a consequence of collective reflections of the X-rays by crystallographic lattice planes belonging to the same family. The Bragg equation reads as:

$$2d\sin\theta = n\lambda \tag{1.20}$$

where d is the interplanar spacing between two lattice planes, θ is the angle between the primary beam and the family of lattice planes and n is the diffraction order.

Finally, by incorporating the condition (1.18) into equation (1.15), we obtain:

$$F_M(\vec{r}_H^*) = \sum_{j=1}^{N} f_j(\vec{r}^*)\exp(2\pi i\vec{r}_H^* \cdot \vec{r}_j) \tag{1.21}$$

$F_M(\vec{r}_H^*)$ is called the *structure factor*. If we consider the positional vector $\vec{r}_j$ with respect to the direct coordinates $[x_j\ y_j\ z_j]$ we can rewrite the equation (1.21) in a more explicit form:

$$F_{hkl} = \sum_{j=1}^{N} f_j \exp 2\pi i(hx_j + ky_j + lz_j) \tag{1.22}$$

F_{hkl} is the main important function in crystallography and it is directly related to the physics of diffraction generated from the crystal symmetry. Since in the kinematical approximation for diffraction the intensity of a diffracted beam is the square of the

amplitude of the scattered wave, the square of the modulus of the structure factor is proportional to the measured intensity. In the next section, we will present some details about the collection of these intensities diffracted by a powdered sample.

1.3 Powder diffraction

An ideal powdered material can viewed as an ensemble of randomly distributed crystallites. In order to show the effect of random orientation on the diffraction, we assume a sample with a crystal structure containing only one reciprocal lattice point defined by $\vec{r}_H^*$. If the sample is an aggregate of randomly oriented crystallites, the vector $\vec{r}_H^*$ is found in all the possible orientations with respect to the X-ray beam. In this case, the diffraction produces concentric cone. This cone represents all the possible directions in which diffraction is observed and its surface gives rise to diffraction.

One way to collect the powder diffraction pattern is by placing a two-dimensional flat detector perpendicular to the incident monochromatic beam. In this case, the diffraction cones can cause a series of concentric rings called powder rings or Debye rings. If the crystallite distribution in the sample is isotropic, the diffracted intensity along each ring is homogenous, and the measurement of a section of the diffraction cones can be considered representative of the reflection intensity profile in the reciprocal space. The parameters collected are then the angle 2θ made by any vector lying on the cone surface and the intensity of the diffracted radiation.

Alternatively of a flat detector, most of the modern instruments use a counter detector (scintillation or gas-ionization type) to measure the position and the relative intensity of the diffraction pattern produced by a powdered sample. During the data collection, the intensity of each diffraction cone is measured by scanning a series of contiguous

angular points. Hence, a continuous intensity profile is recorded by varying the angle 2θ that the detector makes with the incident X-ray beam.

In the next paragraph the powder diffractomer available at ID31 beamline of the ESRF will be briefly described. This instrument was used to perform all the X-ray powder diffraction experiments in the present work.

1.3.1 ID31 beamline at ESRF

ID31 is the high resolution powder diffraction beamline of ESRF.[5] The X-rays are supplied by means of three 11-mm-gap ex-vacuum undulators of the synchrotron which cover the entire energy range from 5 keV to 60 keV. This means that λ can be varied range between 2.48 Å and 0.21 Å.

Double-crystal monochromator is used to select the wavelength and two different Si single crystal cut in different directions can be chosen. In particular a Si (111) crystals for the standard operation mode and Si (311) crystals used for application for which an higher energy resolution is needed. The first monochromator crystal is side cooled by copper blocks through which liquid nitrogen flows. The second crystal is cooled by thermally conducting braids that link to the first crystal. Water-cooled slits define the size of the beam incident on the monochromator, and of the monochromatic beam transmitted to the sample, typically in the range 0.5 – 2.5 mm (horizontal) by 0.1 – 1.5 mm (vertical).

In order to get a so called good powder average, a large beam to illuminate a sufficient volume of sample is needed. Thus there is no focussing and the monochromatic beam from the source passes unperturbed to the sample.

In routine operation mode of the powder diffractometer shown in Fig 1.4 (*a*), a bank of nine detectors with an offset of ~2° between each other is scanned vertically to measure

the diffracted intensity as a function of 2θ. Each detector is preceded by a Si (111) analyser crystal. In order to combine the data from different channels, the offsets need to be calibrated accurately using a diffraction standard (Si standard NIST 640c) and this is done by comparing those parts of the diffraction pattern measured by all of the channels. The offsets and channel efficiencies are then computed in a manner that the signals superimpose as closely as possible.

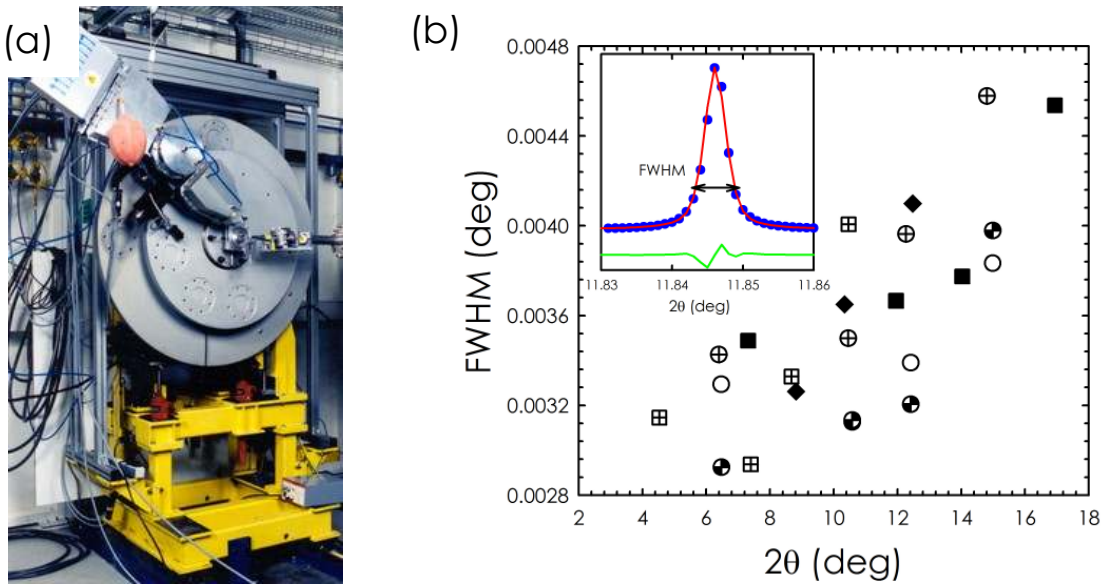

FIG.1.4 *(a) Powder diffractometer at ID31. (Picture taken from http://www.esrf.eu) (b) Angular dependence of FWHM related to diffraction peaks of Si standard sample collected during several experiments performed at ID31. The symbols refer to experiment where different λ ranged from 0.29 to 0.39 Å were used.*

One of the mandatory requirement of the data collection system, it is that the diffracted X-rays must arrive on the detector at precisely the correct angle. Generally, the conventional arrangements infer the angle from the position of a slit or a channel on a PSD (position-sensitive detector) but these set-ups in many cases gives rise to specimen

transparency and misalignment of the sample with respect to the axis of the diffractometer. The use of an analyser crystal renders the positions of diffraction peaks immune to aberrations increasing the accuracy and precision for determining the position of powder diffraction peak.

Finally, the excellent mechanical integrity of the ID31 diffractometer together with the high collimation of the beam gives rise to powder diffraction peaks with a very narrow nominal instrumental contribution to the FWHM (see Fig.1.5(*b*)) and accurate positions reproducible to few tenths of a millidegree.

1.3.2 Rietveld method

As described previously, powder diffraction pattern is a collection of diffracted intensity values plotted against the angular position. In order to get information from such data a process composed by six steps can be used to extract information about the sample crystal structure: (1) Diffraction peak search; (2) Indexing of the whole diffraction pattern; (3) Pattern decomposition; (4) Space group determination; (5) Crystal structure solution; (6) Structural refinement using Rietveld method. In this work, the analysis of all the powder diffraction data were performed using the last step: the Rietveld method.

This method allows one to obtain structural parameter values by refining the experimental data against a given structural model. In the following we give some details about this procedure.

The Rietveld method assumes that the diffraction pattern can be represented by a mathematical model containing both structural and instrumental parameters. When a structural model is available (i.e. from single crystal structure solution) the observed

intensity y_{oi} at the i^{th} angle may be compared with the corresponding intensity y_{ci} calculated as follows:

$$y_{ci} = S\sum_k m_k L_k \left|F_k\right|^2 G(2\theta_i - 2\theta_k) O_k A + y_{bi} \tag{1.23}$$

where S is a scale factor, m_k is the multiplicity factor, L_k is the Lorentz-polarization factor, F_k is the structure factor for the k reflection, $G(2\theta_i\text{-}2\theta_k)$ is the profile function where $2\theta_k$ is the calculated Bragg angle corrected for the zero-point shift error, O_k is the correction term for a non-ideal crystallites distribution, A is the linear absorption correction coefficient and y_{bi} is the background intensity related to the i^{th} intensity.

The goal of the Rietveld refinement is to minimize the residual M between y_{oi} and y_{ci} by a non linear least-squares refinement. The M parameter is defined as:

$$M = \sum w_i \left|y_{oi} - y_{ci}\right|^2 \tag{1.24}$$

where w_i is a weight depending on the standard deviation associated with the peak and with the background intensity.

The accurate determination of the model to describe the profile function $G(2\theta)$ is one of the most crucial step in the Rietveld method. This function can be represented as follows:

$$G(2\theta) = \left[L(2\theta) \otimes g(2\theta)\right] \otimes f(2\theta) \tag{1.25}$$

where the $f(2\theta)$ is a specimen function and $L(2\theta) \otimes g(2\theta)$ is the profile function. The former depends on the specimen characteristics such as size, strain, or structural defects (if any) whereas the latter depends mainly on the radiation source, the wavelength distribution in the primary beam, the beam characteristic as well as the detector system.

A lot of efforts have been devoted to describe the profile function and many analytical peak-shape functions are now available like parameterized Gaussian, Lorentzian functions and several modifications or the convolution of these (i.e. Voigt function). In particular, among all the pseudo-Voigt (an approximation of Voigt function) is the widely used to account for both the Gaussian and the Lorentzian components contributing to the diffraction peak.

The common characteristic of all the profile functions is represented by the way to describe the angular dependence of FWHM. In the Rietveld method this parameter for the Gaussian component is calculated according to:

$$\left[FWHM(\theta)\right]_G = (U\tan^2\theta + V\tan\theta + W)^{1/2} \tag{1.26}$$

whereas for the Lorentzian component, according to:

$$\left[FWHM(\theta)\right]_L = X\tan\theta + Y/\cos\theta \tag{1.27}$$

During the Rietveld refinement the U, V, W and/or X, Y are variable parameters together with the unit cell, atomic positional and thermal parameters. The agreement between the observations and the model can be estimated by several indicators. To

evaluate the goodness of Rietveld refinement presented in this thesis, we have considered the profile (R_p), the weighted (R_{wp}) and the Bragg (R) indicators defined as:

$$R_p = \sum |y_{oi} - y_{ic}| / \sum y_{oi}$$

$$R_{wp} = \left[M / \sum w_i y_{oi}^2 \right]^{1/2} \qquad (1.28)$$

$$R = \sum \left| |F_O| - |SF_c| \right| / \sum |F_O|$$

1.4 Diffuse scattering and the pair distribution function

As previously described, the scattering from a periodic arrangement of atoms (i.e. long range structure) gives rise to the Bragg diffraction. However in same material the deviations from the periodicity of the structure may be important and gives rise to the so called *diffuse* scattering.

Diffuse scattering is due to inelastic scattering generated by electronic excitations, to thermal scattering related to atomic motions and to scattering from structural disorder or more generally structural modifications with respect to the long range structure.[2] We need to point out that here we refer only to diffuse scattering generated by the latter effect.

In order to account for the aperiodicity of the structure, we assume that the total electron density of a crystal can be represented by adding to an average electron density $<\rho>$, a electron density $\Delta\rho$ caused by the fluctuations from $<\rho>$. In order to reduce the electron density to a function of structure factor and, thus, derivable from the measured intensities, we write the follows autoconvolution product (i.e. Patterson function) of $<\rho> + \Delta\rho$ function:[2]

$$\left[<\rho(\vec{r})>+\Delta\rho(\vec{r})\right]\otimes\left[<\rho(-\vec{r})>+\Delta\rho(-\vec{r})\right]$$

$$=<\rho(\vec{r})>\otimes<\rho(-\vec{r})>+\Delta\rho(\vec{r})\otimes\Delta\rho(-\vec{r}) \quad (1.39)$$

For powdered materials the electron density is isotropic so the vector $\vec{r}$ can be substituted by its modulus. By taking the Fourier transform of such Patterson Function we obtain that the measured intensity $I(r^*)$ is expressed as follows:

$$I(r^*)=<|F(r^*)|>^2-|<F(r^*)>|^2+<|F(r^*)|^2> \quad (1.30)$$

Multiplying both the side of equation (1.30) for 2π, substituting $2\pi r^*=4\pi\sin\theta/\lambda=Q$ and considering the scattering factor f, we can rearranged equation (1.30) to define a so called total scattering function $S(Q)$ as:[7]

$$S(Q)=\frac{I^{coh.}(Q)-<f^2(Q)>+<f(Q)>^2}{<f(Q)>^2} \quad (1.31)$$

where $I^{coh.}(Q)$ is the experimental coherent X-ray scattering intensity obtained from the corrected $I(Q)$ for the aberrations, $<f(Q)>^2=[\Sigma_i c_i f(Q)_i]^2$ and $<f^2(Q)>=\Sigma_i c_i[f(Q)_i]^2$ are the square of the mean and the mean of square scattering factors weighted over the concentration of i^{th} atom in the sample.

In order to get the $I^{coh.}(Q)$, we consider that the measured intensity $I(Q)$ is expressed as:

$$I(Q)=P\,A\,N[I^{coh.}(Q)+\underline{I}^{inc}(Q)+I^{mul}+\ldots] \quad (1.32)$$

where the P is the polarization factor, A is the absorption factor, N normalization factor and $I^{coh.}(Q)$, $I^{inc}(Q)$, and I^{mul} are the coherent, incoherent Compton and multiple scattering intensities. The dots stand for other intensities such as the background intensities due to the scattering from air and sample environment.

Among all the corrections, the Compton correction is very important and difficult to apply in X-ray diffraction data. Figure 1.5 shows Q dependence coherent intensity obtained from room temperature diffraction data collected at ID31 (λ= 0.354220Å) on α-Fe_2O_3 crystalline sample together with the calculated incoherent Compton intensity profile.

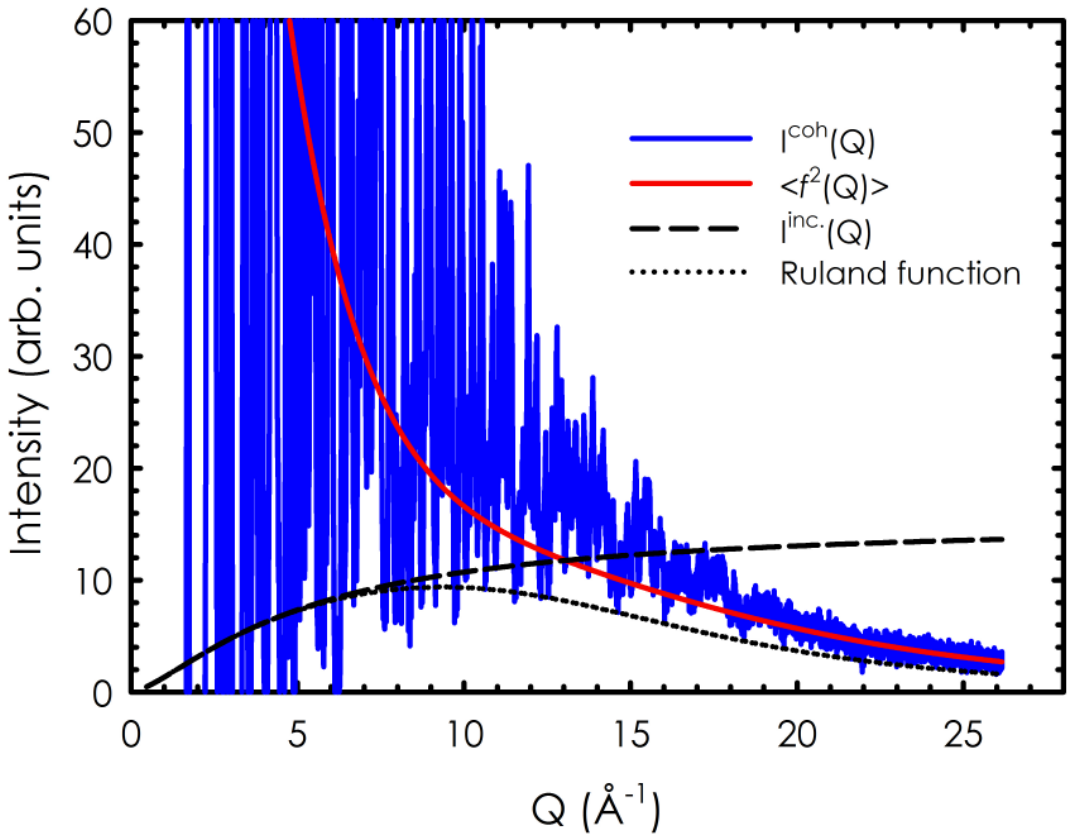

FIG. 1.5 *Comparison between coherent intensity, mean-square atomic scattering factor, $<f^2(Q)>$, incoherent Compton intensity and Ruland function. (Data collected by Adrian Hill).*

We can see that the incoherent Compton intensity becomes much larger than coherent one at high Q value. In addition the scattering from the sample is almost incoherent at high Q and is approximately equal to $\langle f^2(Q)\rangle$ in Fig. 1.7. So in this Q region even small error in the Compton correction could give rise to big error in the extraction of coherent scattering. Experimentally the Compton scattering can be removed by using analyzer crystal in the diffracted beam as available for the ID31 instrument. On the other hand, when this correction is not possible, the theoretical Compton profile at high Q have to be calculated and subtracted from the measured data. For example the profile shown in Fig.1.5 was calculated using the Compton scattering analytical formula.[7] This approach is reliable only to discriminate the Compton at high Q and in order to remove the Compton in the middle-low Q region the method suggested by Ruland can be applied. In this method the Compton intensity is smoothly attenuated with increasing Q (dotted line in Fig. 1.5) by applying a monochromator cut-off function $Y(Q)$ with a given window value. The incoherent intensity is then calculated by multiplying the $Y(Q)$ with the theoretical Compton profile and subtracted from the experimental data.

In Fig.1.6(*a*) we plot the $S(Q)$ function obtained from the corrected coherent intensity shown in Fig.1.5. It should be noted that at high Q the $S(Q)$ oscillates around the unity (inset of Fig.1.6). Indeed, as the $I^{coh}(Q)$ tends to $\langle f^2(Q)\rangle$ at high Q (Fig. 1.5), the $S(Q)$ reduces to 1 according to equation (1.31).

Hence, the $S(Q)$ contains both the Bragg scattering and the diffuse scattering (if any) and one way to get information from this data it is to apply the so called Pair Distribution Function method (PDF). The PDF, $G(r)$ function, is obtained through the $S(Q)$ via the sine Fourier Transform (*FT*):[7]

$$G(r) = \frac{2}{\pi} \int_{Q=0}^{Q_{max}} Q[S(Q) - 1] \sin(Qr) dQ \tag{1.33}$$

where $Q[S(Q)-1]$ is often defined as $F(Q)$ function and the upper integration limit Q_{max} is the reciprocal space cut-off.

In Fig. 1.6(*b*) we show the $G(r)$ calculated up to 200 Å for α-Fe_2O_3 sample with a Q_{max}~ 26 $Å^{-1}$. Each positive $G(r)$ peak indicates r value where the probability of finding two atoms separated by a certain distance is greater than that determined by the so called number density, i.e. total number of atoms in the unit cell volume. Hence, the $G(r)$ gives the probability of finding two atoms separated by a distance r averaged over all pairs of atoms in the sample. In this context, the structure of the material is studied in terms of the distances between atoms though the PDF method, and since no periodicity is assumed, both the long range structure and the local deviations with respect to this average structure can be explored.

As in the case of powder diffraction data, full structure profile refinements can be carried out also using PDF data. The PDF of a given structure can be calculated using the relation:[8]

$$G^c(r) = \frac{1}{r} \sum_i \sum_j \left[\frac{f_i f_j}{< f >^2} \delta(r - r_{ij}) \right] - 4\pi r \rho_0 \tag{1.34}$$

where the sum runs over all pairs of atoms I and j separated by rij in the structural model. The X-ray atomic scattering factor here are evaluated at a defined value of Q which in many case is zero. Hence, these factors correspond to the number of electrons of atom *i* and *j*.

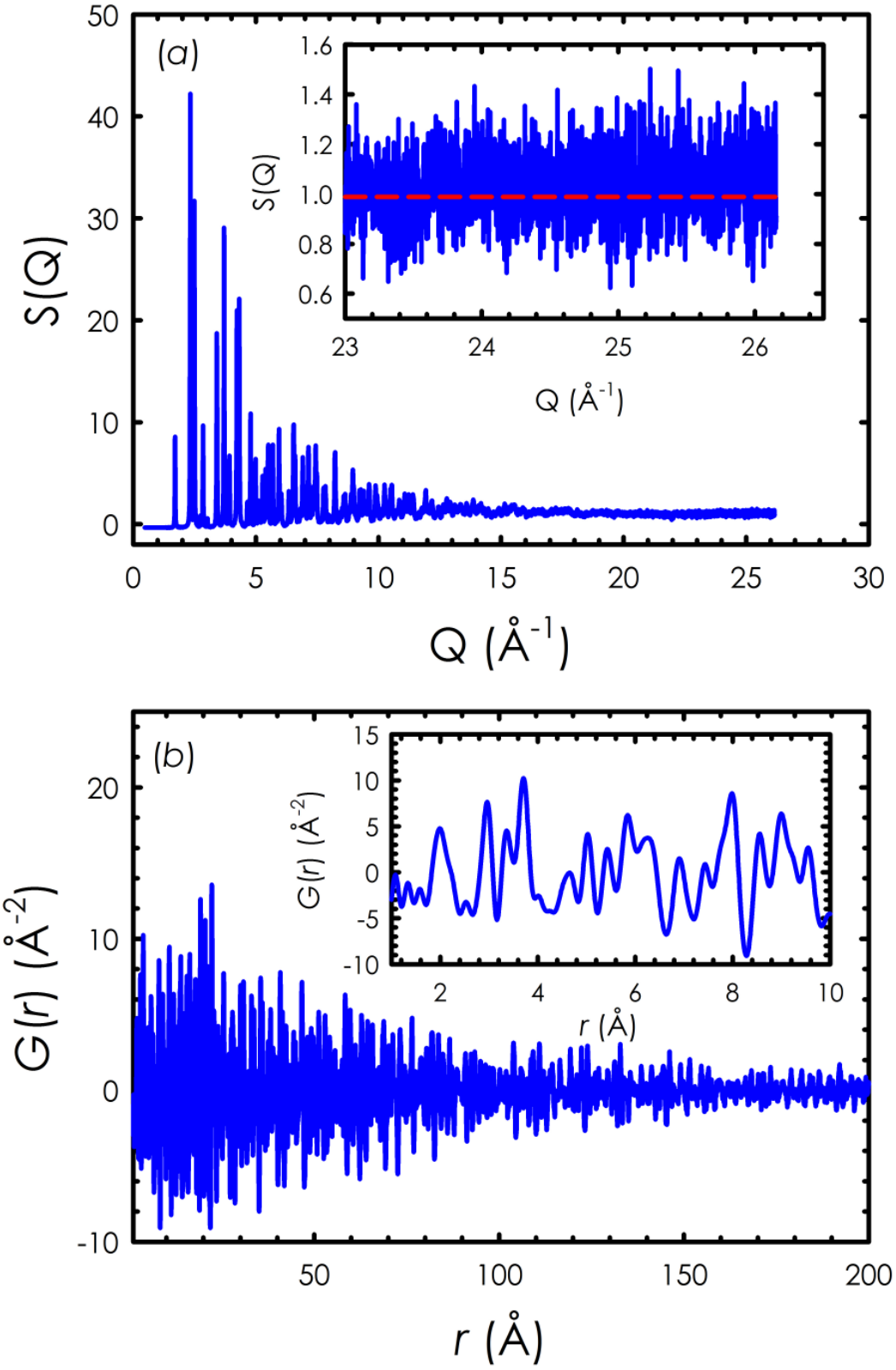

FIG 1.6 *(a) S(Q), (b) G(r) functions of α-Fe_2O_3 obtained from room temperature diffraction data collected at ID31.*

In order to account for the atom displacements from the average position two methods can be used. One can simulate a large enough model containing all the desired and perform an ensemble average. Alternatively one can convolute the Dirac functions in equation (1.34) with a function accounting for the displacements. In particular, in the simplest case the $\delta(r - r_{ij})$ is replaced by a modified Gaussian function of type:

$$T_{ij}(r) = \frac{1}{\sqrt{2\pi}\sigma_{ij}(r)} \exp\left[-\frac{(r - r_{ij})^2}{2\sigma_{ij}^2(r)} \right] \cdot \left[1 + \left(\frac{r - r_{ij}}{r_{ij}} \right) \right] \tag{1.35}$$

The width $\sigma_{ij}(r)$ of $T_{ij}(r)$ is given by the atomic displacement parameters of atoms *i* and *j*.

The observed $G(r)$ can be then fitted against the $G_c(r)$ by applying suitable symmetry constrains and varying cell parameters, atomic positions and thermal parameters.

The degree of accuracy of the PDF refinement can be assesses by agreement factor of type:

$$R_W = \left[\frac{\sum w_i (G_i - G_i^c)^2}{\sum w_i (G_i)^2} \right]^{1/2} \tag{1.36}$$

where $w_i = 1/\sigma^2(r_i)$ and $\sigma(r_i)$ is the standard deviation at a distance r_i.

References

[1] G. H. Stout, and L. H. Jensen, in *X-ray Structure Determination: A Practical Guide*, Wiley-Interscience (1989).

[2] C. Giacovazzo, in *Fundamentals of crystallography*, Oxford University Press (2002), Chap. 2, 3, 4.

[3] M. Sánchez del Río, R. J. Dejus, 2004, *XOP 2.1: A new version of the X-ray optics software toolkit*, "Synchrotron Radiation Instrumentation: Eighth International Conference, edited by T. Warwick et al. (American Institute of Physics), pp 784-787.

[4] W. L. Bragg, Proc. Camb. Phil. Soc. **17**, 43 (1913).

[5] A. N. Fitch, J. Res. Natl. Inst. Stand. Technol. **109**, 133 (2004).

[6] Young, R.A., in *The Rietveld Method*, Oxford: University Press (1993).

[7] T. Egami, S. J. L. Billinge, in *Underneath the Bragg Peaks, Volume 16: Structural Analysis of Complex Materials*, Pergamon (2003).

[8] R. B. Neder, T. Proffen, in *Diffuse scattering and defect structure simulations: a cook book using the program DISCUS*, Oxford: University Press (2009).

2. Crystal structure of $GdBaCo_2O_{5.0}$

In this Chapter we present an accurate investigation of the prototypical rare-earth cobaltite $GdBaCo_2O_{5.0}$ by complementary synchrotron powder and conventional source single-crystal X-ray diffraction experiments. We assign the correct space group (*Pmmm*) and the accurate crystallographic structure of this compound at room temperature. By increasing temperature, a second order structural phase transition to a tetragonal structure with space group *P4/mmm* at $T \sim 331$ K is found. Close to the Néel temperature ($T_N \sim 350$ K), anomalies appear in the trend of the lattice constants, suggesting that the structural phase transition is incipient at T_N. A possible mechanism for this complex behaviour is suggested. These results were published in reference: L. Lo Presti, M. Allieta, M. Scavini, P. Ghigna, V. Scagnoli, and M. Brunelli, Phys. Rev. B **84**, 104107 (2011).

2.1 Introduction

It is well known that the crystal structure and the bulk physics of correlated materials, such as band gap, orbital, charge ordering and magnetic properties, are often coupled.[1,2,3,4] It may also happen, on the other hand, that electronic and magnetic phase transitions are associated to somewhat hardly detectable structural distortions, that nevertheless may imply important symmetry changes. This is just the case of the cobaltites of general formula $LnBaCo_2O_{5+\delta}$, where $0 < \delta < 1$ and Ln may be a trivalent lanthanide ion or yttrium. Such compounds have raised in the last decade a great deal of interest due to their intriguing magnetic and transport properties,[4,5,6,7,8] which can furthermore be varied as a function of temperature[7,8,9] or even pressure.[7] Recently, these compounds turned out to be attractive also for the development of new

intermediate-temperature solid oxides fuel cells (IT-SOFC).[10,11] They display the so-called "112"-type perovskite structure[5] (Fig. 2.1), that consists of alternating layers where the three metals are piled up along the *c* axis, each of them being coordinated by oxygen anions arranged in squares through the sequence ...-BaO-CoO_2-LnO_{δ}-CoO_2-.... It should be noted that the δ-molar excess of oxygen ions is invariably accommodated in the rare-earth layer, which is totally oxygen-free in the stoichiometric $LnBaCo_2O_{5.0}$ compounds. Such variability in the oxygen stoichiometry influences the oxidation state of cobalt, making possible the coexistence of Co(II)/Co(III) ($\delta < 0.5$) or Co(III)/Co(IV) ($\delta > 0.5$) both in octahedral (CoO_6) and square pyramidal (CoO_5) environments. In general, the possibility of tuning with great accuracy the effective oxygen content[12] and/or selecting lanthanide ions of different radii[13] within the $LnBaCo_2O_{5+\delta}$ structure, provides the opportunity to control several macroscopic key features such as resistivity, thermoelectric power and magnetoresistance (MR).[12,14,15,16,17]

Approximately a decade ago, the crystal structure of oxygen-deficient $LnBaCo_2O_{5.0}$ (Ln=Y,[18] Tb,[4] Dy,[4] Ho,[4] and Nd[19]) compounds was accurately determined by powder neutron diffraction studies, concluding that they are all paramagnetic with tetragonal space group *P*4/*mmm* above the Néel temperature (T_N), that ranges from 330 to 380 K, depending on Ln^{3+} ionic radii. Concerning the Ln = Gd compound, in particular, a reasonable estimate of $T_N \approx 350$ K comes from both magnetic[12] and shear modulus[20] measurements. In any case, it is reported that below T_N these cobaltites "*undergo a magnetic transition to an antiferromagnetic structure which itself induces an orthorhombic distortion of the unit-cell*",[4] leading to a different structure that can be more accurately described by the orthorhombic *Pmmm* space group. Actually, also the room temperature (RT) structure of the Ln = Gd stoichiometric cobaltite

($GdBaCo_2O_{5.0}$) was described as orthorhombic (*Pmmm*) by X-ray powder diffraction experiments.[17] More recently, however, the same compound was assigned to higher tetragonal symmetry on the basis of single-crystal X-ray diffraction results at RT.[12] Such conflicting outcomes between single-crystal and powder diffraction techniques raise the question on what is the correct space group of $GdBaCo_2O_{5.0}$ below $T_N \approx 350$ K,[12] and, as a consequence, the pertinent temperature scales for the magnetic and structural phase transitions. This is a central point, as the structural symmetry governs a number of intensive physical properties of the condensed matter.[21,22,23] Moreover, several authors emphasize the importance of the crystal structure to rationalize the orbital and spin states of the transition-metal ions in these materials.[9,20,23,24,25] Neutron diffraction studies on the Ln = Gd compound may solve the issue, but the considerable neutron absorption coefficient of gadolinium makes them quite difficult if compared to earlier experiments on structurally-related compounds.[4] Anyhow, it should be noted that the orthorhombic distortions in the above mentioned $LnBaCo_2O_{5.0}$ cobaltites are very small, the difference between the *a* and *b* parameters being roughly 0.2-0.3 % (see Table 1 in Refs. 4 and 17), *i.e.* of the same order of magnitude as the estimated standard deviations (esd's) on cell parameters typically retrieved by conventional single-crystal X-ray diffraction experiments: in fact, Taskin *et al.* described $GdBaCo_2O_{5+\delta}$ as tetragonal for $0 < \delta < 0.45$ at room temperature, even though they dealt with carefully prepared and detwinned specimen.[12] Last but not least, it should be noted that in the Literature concerning correlated materials, quite often the claim emerges of having obtained "*high-quality single crystals*", and several physical properties are then measured on these specimens, usually throughout a large *T* (or *p*) range. It should be stressed, however, that the term '*single crystal*' has the precise meaning of '*any solid object in which an orderly three-dimensional arrangement of the atoms, ions, or*

molecules is repeated throughout the entire volume'.[26] In other words, when the 'quality' of single crystals is to be assessed, it is important to consider not only the chemical purity of them, but also the degree of perfection, in terms of how many independent coherent scattering domains give rise to the observed diffraction signals. On the contrary, however, to the best of our knowledge, *quantitative* crystallographic information are rarely provided, despite their importance in assessing the actual sample quality or in ensuring that the specimen is truly *single*, i.e. not twinned, or even polycrystalline. It should be stressed that even well-shaped crystals, with a homogeneous appearance of their surface, may be in fact severely twinned.[27] Therefore, a great deal of caution should be employed in assessing the nature (monodomain or polydomain crystals?) of the specimen, especially when the overall measured physical properties of the material may depend on the effective degree of crystallinity or on its microstructure. Actually, this is just the case when the underlying physics manifests a significant anisotropic behaviour.[6,12] Sometimes in the Literature, on the contrary, samples claimed as '*high-quality single crystals*' do not resemble 'single crystals' at all, even by visual inspection, as they display inhomogeneities (e.g. differently coloured zones), breaks with misaligned regions or significant amounts of their surface characterized by highly irregular shape together with clearly well-formed faces.[28,29] On the other hand, if only a true monodomain part of the sample was selected and then investigated by X-ray diffraction, the claim that the overall specimen is a *'high-quality single crystal*' appears to be absolutely not justified.

The present contribution aims at (*i*) shedding light on the correct crystal symmetry of $GdBaCo_2O_{5.0}$ across the Néel temperature; (*ii*) finding the pertinent temperature scales for the magnetic and structural phase transitions; and (*iii*) illustrating what are the pros

and cons of single-crystal (SCD) and high-resolution X-ray powder diffraction (XRPD) techniques when applied to the test case here described.

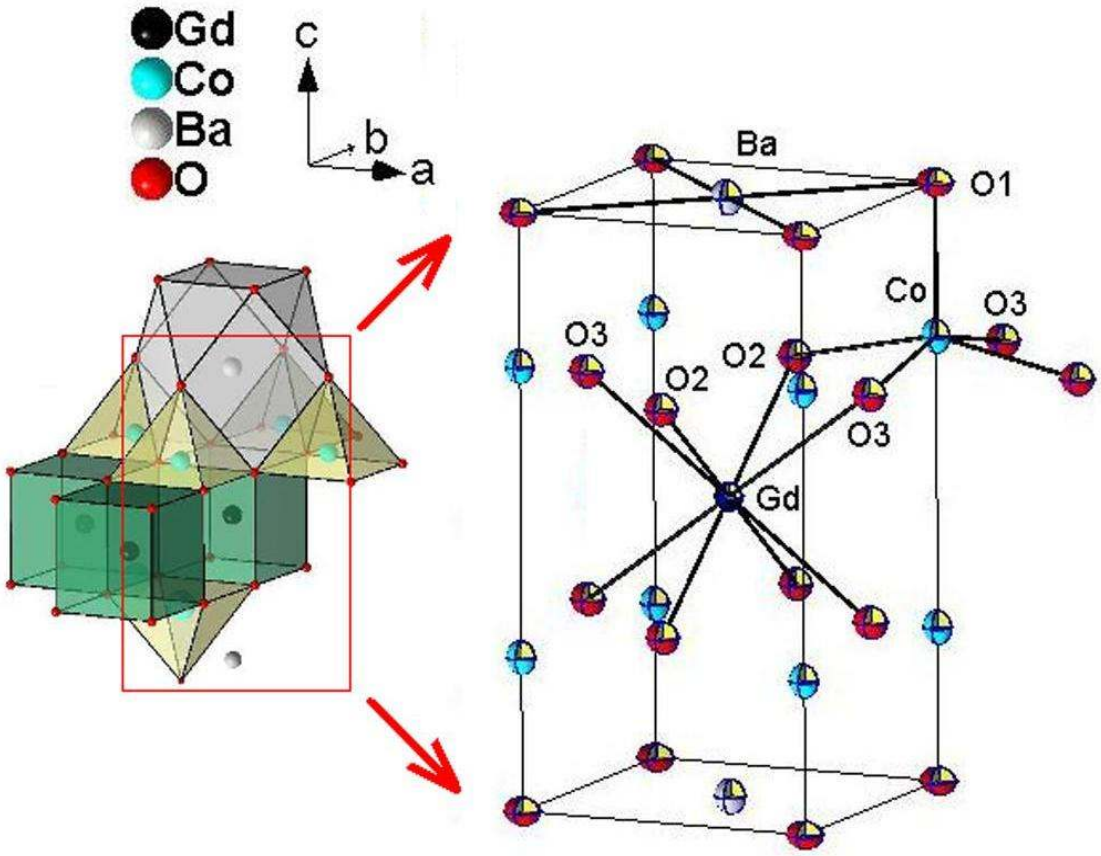

FIG. 2.1 *Packing scheme and atom numbering of $GdBaCo_2O_{5.0}$ at T = 298 K, with coordination polyhedra of Ba (cuboctahedron), Co (square pyramid) and Gd (cube) highlighted. The frame encloses the region of space occupied by the conventional "112" unit cell.*

2.2 Powdered and single crystal sample preparation

A batch of microcrystalline $GdBaCo_2O_{5+\delta}$ was prepared by solid state reaction in air. Stoichiometric amounts of high-purity powders of Gd_2O_3 (Aldrich 99.9%), $BaCO_3$ (Aldrich 99.98%) and CoO (Aldrich 99.9%) were thoroughly mixed and pressed into pellets. After a decarbonation process (24 h at T = 1000 °C), the mixtures were ground,

pressed into pellets, fired in air at T = 1100 °C for 48h and eventually, according to Taskin *et. al*.,[12] annealed at T = 850 ºC for 72 h in a flow of pure nitrogen. To check the oxygen content in the synthesized powdered material, we performed some thermogravimetric (TGA) measurements as a function of temperature and time in a flow of air (30mL/min) and N_2 (30mL/min). TGA outcomes show that keeping the material for some hours at T > 800 ºC (Fig. 2.2) in inert atmosphere ensures that the lowest oxygen concentration can be actually obtained. Subsequent XRPD analysis was performed on freshly prepared samples and no evidences of tetragonal / orthorhombic phase coexistence attributable to minute oxygen content variations[18] were detected at room temperature.

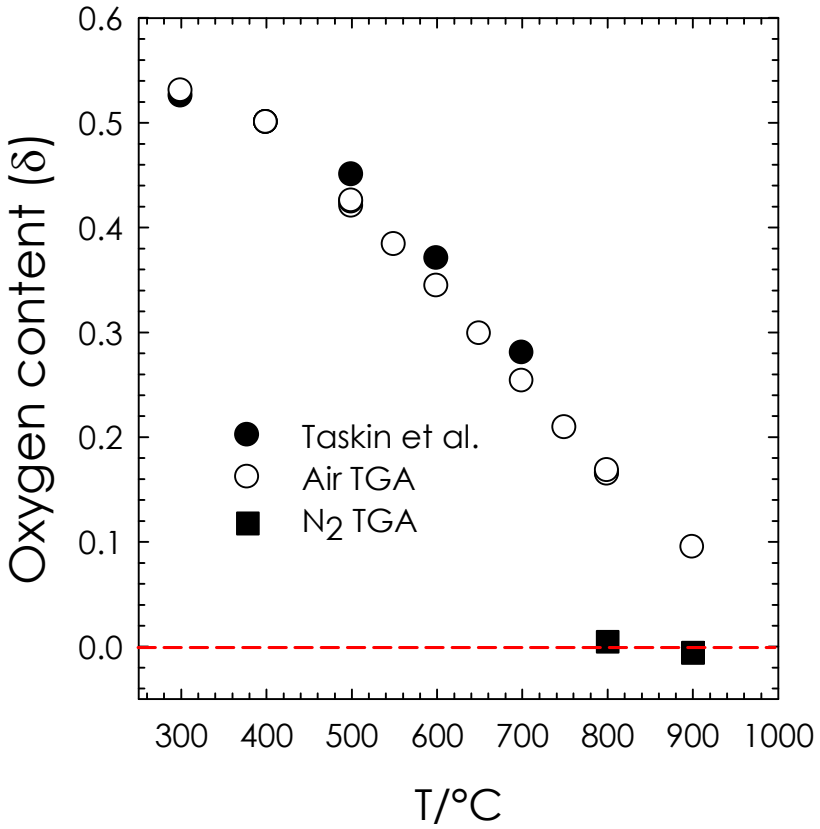

FIG. 2.2 *Oxygen molar content δ as a function of T. Full circles: data from Ref.12; empty circles: heating in air; black squares: heating in N_2.*

$GdBaCo_2O_{5+\delta}$ single crystals have been grown from the above prepared powdered material using a Cyberstar image furnace in flowing air at a constant displacement rate of 0.5 mm/h. The final, black rod of material had a glass-like appearance, with a lot of very small, well-formed crystals grafted in an amorphous matrix on its top. The same annealing procedure as described before was applied to ensure the desired $\delta = 0$ oxygen stoichiometry. Eventually, the rod was broken into pieces and the fragments carefully examined under a stereomicroscope. A ~ 80 μm large sample was found to be of suitable quality for the single crystal X-ray analysis and mounted with epoxy glue on the top of a glass fibre.

In addition, to testify the good quality of the crystal and that the crystal is not twinned, we show some diffraction spots in the frames collected using synchrotron radiation diffraction at room temperature. In particular, on the same single crystal $GdBaCo_2O_{5.0}$ sample, we performed some quick measurements at the six circle KUMA6 diffractometer using an charge coupled device (CCD) detector with λ=0.70826 Å at BM01A beamline of the ESRF (European Synchrotron Radiation Facility). From the selected frames collected at room temperature shown in FIG. 2.3, it is evident that none diffraction spots are splitted.

2.3 Powder diffraction experiment

Powder diffraction patterns between T = 400 K and RT were collected at the ID31 beamline of the European Synchrotron Radiation Facility (ESRF) in Grenoble. A powdered sample of $GdBaCo_2O_{5.0}$ was loaded in a 0.67 mm diameter kapton capillary and spun during measurements to improve powder randomization. A wavelength of λ=0.39620(5) Å was selected using a double-crystal Si(111) monochromator. Diffracted intensities were detected through nine scintillator counters, each equipped

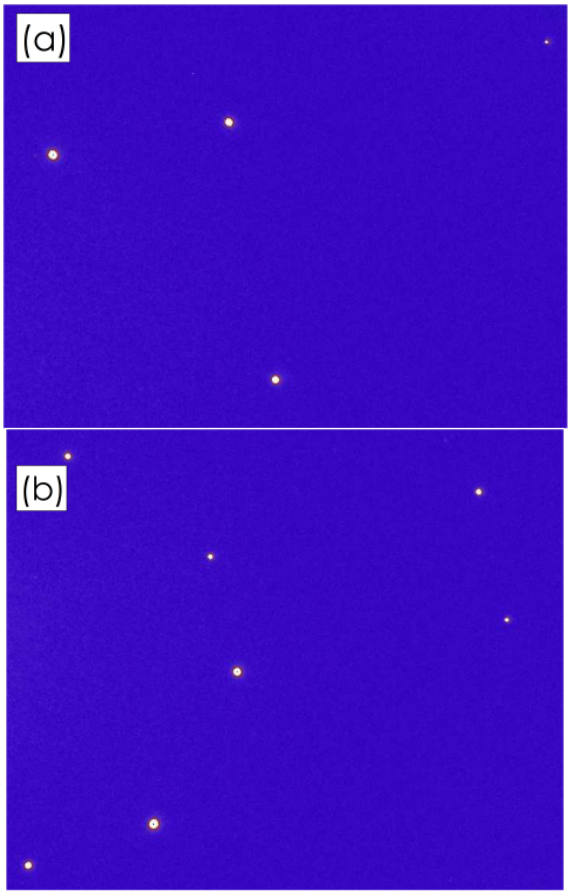

FIG.2.3 *Selected diffraction frames collected at room temperature using synchrotron radiation diffraction on $GdBaCo_2O_{5.0}$ single crystal at BM01A (ESRF).*

with a Si(111) analyzer crystal which span over 16° in the diffraction angle 2ϑ. Two different data collection strategies were employed: (*i*) the powdered sample was measured in the $0< 2\vartheta < 50°$ range for a total counting time of 1 hour, first at 300 K and at 400 K; (*ii*) XRPD patterns in the $0< 2\vartheta < 20°$ range were collected every 3K while raising temperature from 300 K to 400 K. The sample was warmed using a N_2 gas blower (Oxford Cryosystems) mounted coaxially.

The XRPD patterns were analyzed with the Rietveld method as implemented in the GSAS software suite of programs[30] which feature the graphical interface EXPGUI.[31] The background was fitted by Chebyshev polynomials. Absorption correction was performed through the Lobanov empirical formula[32] implemented for the Debye-

Scherrer geometry. Line profiles were fitted using a modified pseudo-Voigt function[33] accounting for asymmetry correction.[34] In the last cycles of the refinement, scale factor(s), cell parameters, positional coordinates and isotropic thermal parameters were allowed to vary as well as background and line profile parameters.

2.4 Single crystal diffraction experiment

Diffraction data were collected using a four-circle Siemens P4 diffractometer equipped with a conventional Mo source (λ = 0.71073 Å) and a point scintillation counter at nominal 50 kV x 30 mA X-rays power. Room-temperature unit cell dimensions of $GdBaCo_2O_{5.0}$ were determined from a set of 28 reflections (11 equivalents) accurately centred in the $10.8 \leq 2\vartheta \leq 26.4$ ° interval. An entire sphere of 2998 reflections was then collected within $\sin\vartheta/\lambda = 0.90$ Å with scan rate of 2 °/min, providing a 100 % complete dataset. The intensities of three reference reflections were monitored during the entire data acquisition, and a small linear correction for intensity decay (up to 1.01 % upon a total of ~94 h) was applied to the diffraction data. Possible off-lattice reflections were also looked for by accurate scanning of the reciprocal lattice at fractional indices positions, but no superlattice spots or alternative symmetries were detected anyway. Systematic extinction rules were also carefully screened (see Table A.1 in Appendix A), revealing that no translational symmetry elements are to be expected within the unit cell.

For $GdBaCo_2O_{5.0}$, the absorption correction is probably the most crucial step of the data reduction process, as the linear absorption coefficient of this material, μ, which amounts to 29.6 mm^{-1} for $\lambda_{Mo,K\alpha}$ = 0.71073 Å, is exceptionally large with respect to lighter-element containing compounds. Nevertheless, in this case the problem is further

complicated by the shape of the specimen, which is necessarily irregular as it was obtained after breaking into pieces the original rod used to produce single crystals from the melt. Some unsuccessful attempts were done to ground to a sphere other samples of the title compound: due to the considerable hardness of the material, the best shape we obtained (when the crystal did not break) was a sort of elongated ellipsoid - not significantly different from the specimen used in the current study. Moreover, the efforts spent in adopting a more accurate analytical absorption model, which would imply to correctly index the macroscopic crystal faces, led up till now to unsatisfactory results. As a matter of fact, the specimen is very small, black (making quite difficult to recognize the various faces), and its surface is characterized by both well-formed planes and irregular zones (Fig. 2.4 (*a*)). Therefore, we eventually chose to adopt an empirical absorption correction.[35] To this end, 1926 individual azimuthal Ψ-scan measures (i.e. around the diffraction vector in the reciprocal space) were performed on 28 suitable reflections covering, when possible, the entire Ψ range with a scan rate of 2 °/min. The empirical correction improved the merging *R* factor within the set of azimuthal measures from 0.0907 to 0.0257 (*mmm* point symmetry) and from 0.0920 to 0.0267 (4/*mmm* point symmetry). Figure 2.4(*b*) shows the effect of this correction on a couple of azimuthal scans: it can be seen that the periodic oscillations of the reflection intensities as function of Ψ are considerably smoothed down, within 3 esd's, to a constant, average value. This is due to the fact that, as it can be seen in Fig. 2.4(*a*), the elongated shape of the crystal is not too far from being an ellipsoid, making acceptable, all things considered, this absorption correction strategy, at least for the accurate determination of the crystal structure.

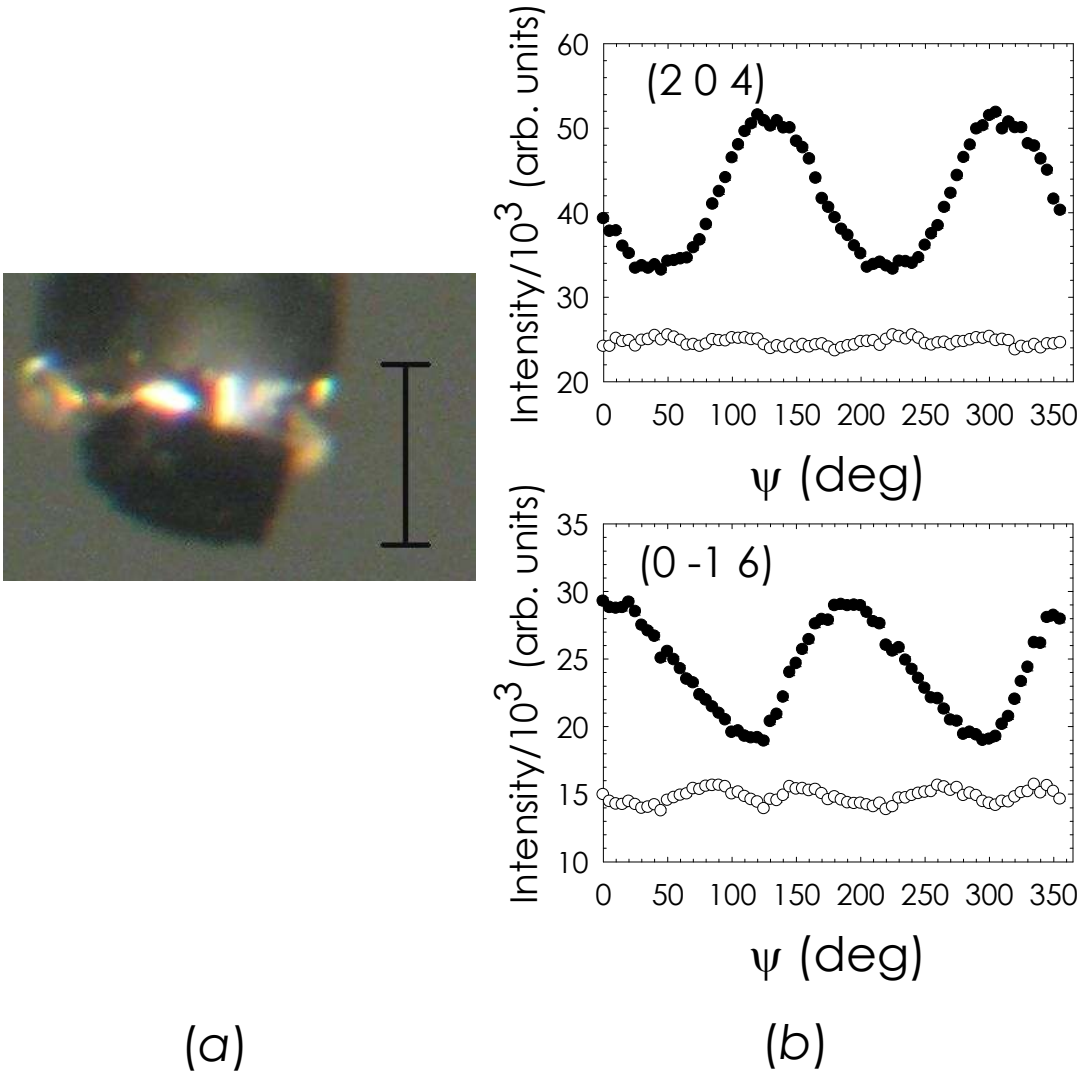

FIG. 2.4 *(a) Single crystal of $GdBaCo_2O_{5.0}$ employed in the present work, mounted on a glass capillary with two-component epoxy glue, as viewed with a Zeiss (STEMI DRC) microscope (40x magnification). The vertical bar in the photograph corresponds roughly to 80 μm. (b) Measured and corrected (mmm symmetry) intensities vs. Ψ angle (deg) relative to the azimuthal scans of the (2 0 -4) and (0 -1 6) reflections. The diameter of each dot corresponds to ≈ 1 esd. Full dots: measured intensities. Empty dots: corrected intensities after applying the empirical absorption model.*

It should be noted that the above described empirical absorption model provided the best results in terms of smoothing intensity oscillations of the azimuthal scans,

equivalent reflection intensities, final agreement factors and electron density residuals. Nevertheless, some small fluctuations in the corrected azimuthal scan intensities are still recognizable (Fig. 2.4(*b*)), indicating that a more accurate treatment is in order if sensible information besides the crystal structure, e.g. on the experimental electron density, is sought. If unbiased (or at least less-biased) estimates of structure factor amplitudes in heavy-atom based compounds are looked for, it should be stressed that it is mandatory to proceed with great caution while performing the absorption correction of SCD diffraction data. In turn, this is crucial not only for providing an accurate structural model, but also in the perspective of assessing the correct crystal symmetry through equivalence relationships in the reciprocal space (see below).

The SCD structural model (see Table 2.1) was obtained within the spherical atom approximation.[36] The direct-space Patterson function was employed to locate the metal atoms. Oxygen atoms were subsequently found by Fourier difference synthesis. No evidence of atom site disorder was detected. The compound stoichiometry was confirmed by SCD results, as no residual Fourier peaks attributable to guest atoms in the unit cell were found.

2.5 SCD results

The proper assessment of the symmetry and cell parameters of the title compound is far from being trivial, as the orthorhombic distortion, if any, is certainly small. It is well recognized that joint powder and single-crystal diffraction techniques, constitute a very powerful tool to achieve a high level of accuracy in crystal structure determinations.[37,38,39,40,41,42] It is therefore desirable to apply such approach when the expected changes in the crystallographic structure are hardly detectable.

Table 2.1. *Crystallographic and refinement details at room temperature for the stoichiometric cobaltite $GdBaCo_2O_{5.0}$ (PM = 492.45 uma, Z = 1).*

Data collections				
Technique	SCD		XRPD	
Source	Conventional X-rays		Synchrotron radiation	
Data collection temperature (K)	298 (2)		300 (2)	
Radiation wavelength (Å)	0.71073 (Mo K_α)		0.39620(5)	
Absorption coefficient (mm^{-1})	29.585		5.573	
Monochromator	Graphite single-crystal		Double-crystal Si(111)	
Diffractometer	Siemens P4		ID31 (ESRF)	
$2\vartheta_{max}$ (°)	79.8		50.0	
No. of collected reflections	2998		727	
Lattice				
Space group	*Pmmm* (47)	*P*4/*mmm* (123)	*Pmmm* (47)	
a (Å)	3.920 (1)	3.920(1)	3.91830(2)	
b (Å)	3.919 (1)	3.920(1)	3.92389(2)	
c (Å)	7.510 (1)	7.510(1)	7.51824(3)	
V ($Å^3$)	115.37 (4)	115.40(4)	115.593(1)	
No. of unique reflections	457	259	-	
R_{merge}	0.0437	0.0472	-	
Spherical atom refinements [1]			*Relevant Rietveld agreement factors*	
$R(F)$	0.0293 / 0.0203	0.0271 / 0.0185	$R(F)$	0.0277
$wR(F^2)$	0.0547 / 0.0422	0.0526 / 0.0383	$R(F^2)$	0.0447
Gof	0.942 / 0.916	0.932 / 0.954	*R*p	0.1089
Extinction parameter	0.038(3) / 0.059(4)	0.044(4) / 0.068(5)		
Data-to-parameter ratio	19.9 / 7.8	17.3 / 7.1		
$\Delta\rho$ max, min ($e \cdot Å^{-3}$)	2.01, -2.05 / 0.97, -0.94	1.84, -2.42 / 0.66, -0.88		

Within the SCD technique, examining the intensity distribution statistic usually faces the problem of recognizing the correct crystal point symmetry, but this strategy is of

[1] All independent data / data within $\sin\vartheta/\lambda \leq 0.65$ $Å^{-1}$.

difficult applicability to XRPD data due to overlapping of Bragg peaks.[43] When the space group cannot be assigned on the basis of systematic extinctions, it is possible to complement the information provided by diffraction data with spectroscopic (IR, Raman) or second-harmonic generation techniques. In this way, the correct point symmetries can be in principle determined on the basis of the allowed vibration or electronic accessible states.[44,45] It should be noted that such a method can unequivocally assess the presence of a centre of inversion, but it may not be straightforward (e.g. it may require the theoretical simulation of the IR and Raman active modes for different crystal symmetries[44]) when the ambiguity is more subtle, as in the case here discussed. In $GdBaCo_2O_{5.0}$, actually, the uncertainty arises from alternative choices between the C_4 or C_2 axes in the symmorphic, extinction-free and centrosymmetric *P*4/*mmm* (D_{4h}) or *Pmmm* (D_{2h}) groups: to the best of our knowledge, the present study is the first aimed at discriminating the correct point symmetry in heavy-metal containing compounds when different proper rotation axes are involved, by using diffraction methods only. As the equivalence relationships in the reciprocal lattice are different between orthorhombic and tetragonal symmetry, careful inspection of equivalent intensities is mandatory when ambiguities among different space groups occur, provided that the measured data were properly corrected for systematic errors (and particularly, in this case, for absorption: see the discussion above). Within the tetragonal system, *hkl* reflections are necessarily equivalent to the *khl* ones. On the contrary, this is no longer true in an orthorhombic space group. To assess if there is some evidence from the analysis of the equivalent statistics that the orthorhombic symmetry is in fact to be preferred with respect to the tetragonal one, we carried out two parallel SCD data reductions both in *Pmmm* and *P*4/*mmm* space groups. In the following, we will refer to such two distinct datasets as "orthorhombic" and

"tetragonal", respectively. In particular, we compared individual measures of possible equivalent *hkl* and *khl* reflections within the "orthorhombic" dataset i.e. that corrected for absorption without forcing the empirical transmission surface to make the azimuthal-scanned *hkl* and *khl* intensities to be equivalent to each other. If the merging *R*(int) factor, defined as

$$R(\text{int}) = \sum \left| F_{obs}^2 - \overline{F}^2 \right| / \sum F_{obs}^2 \qquad (2.1)$$

is calculated for this dataset under the various Laue classes (see Table A2 in the Appendix A), it comes out to be essentially identical for the *mmm* and 4/*mmm* symmetries (0.042 *vs* 0.044). This implies that, even *without* explicitly imposing the 4/*mmm* symmetry, almost all the individual measures are equal, within 1 or 2 esd's, to the corresponding weighted averages in *P*4/*mmm*. Closer inspection of the individual diffraction measures shows that, even if the "orthorhombic" dataset is considered, the deviations with respect to the corresponding weighted means in *P*4/*mmm* are, in general, immaterial. Taking into account, as an example, the 16 individual measures with intensity *I* of the reflection (1 4 6) and all its 4/*mmm* equivalents ($\pm$ 1 $\pm$ 4 $\pm$ 6 and $\pm$ 4 $\pm$ 1 $\pm$ 6) within the "orthorhombic" dataset, the quantity $\langle [I-\langle I \rangle]/\sigma(I) \rangle$ comes out as large as 0.9, $\langle I \rangle$ being the weighted average intensity and $\sigma(I)$ the corresponding individual esd for the measure with intensity *I*. Out of the total of 2998 measured diffraction data, only 13 (0.4 %) deviate by more than 3.0 esd's from the corresponding averages, 9 of them being nevertheless equal to their weighted average value within 4.0 esd's. Such poorly significant differences can be explained, however, in terms of counting statistics or small imperfections of the empirical model for absorption. In

general, the final "orthorhombic" and "tetragonal" datasets have individual intensities very similar to each other (Fig. A1 in the Appendix A), showing that neglecting the C_4 proper symmetry axis in the unit cell during the data reduction process has but an immaterial effect on the measured structure factor amplitudes. In other words, the absorption correction produces exactly the same effects on the observed intensities, irrespective of the Laue group (4/*mmm* or *mmm*) adopted to generate the empirical transmission surface.

As regards the final least-square agreement factors, they are slightly lower in *P*4/*mmm* symmetry (see Table 2.1), but such differences are again barely significant, as it is possible to easily account for them considering the different data-to-parameter ratio (≈20 in *Pmmm*, vs. ≈17 in *P*4/*mmm*). Therefore, in agreement with earlier SCD reports on the same compound,[12] there are not unquestionable evidences to reject the higher *P*4/*mmm* symmetry in favor of the lower *Pmmm* orthorhombic one. Rather, from the analysis of both the lattice metric and the reflection statistics, the tetragonal symmetry is to be preferred on the basis of our room-temperature SCD data.

2.6 XRPD results across the PM-AF transition

Figure 2.5 (*a*) shows the Rietveld refinement against XRPD data at T = 300 K in the *Pmmm* space group, using as a starting point the structural model provided by SCD at 298 K. The corresponding structural and agreement parameters are reported in Table 2.2. Positional and thermal parameter estimates for the same title compound at T = 400 K (>> T_N, *P*4/*mmm* symmetry) can be found in Table A.3 of the Appendix A while diffractogram at the same temperature is shown Fig. 2.5 (*b*).

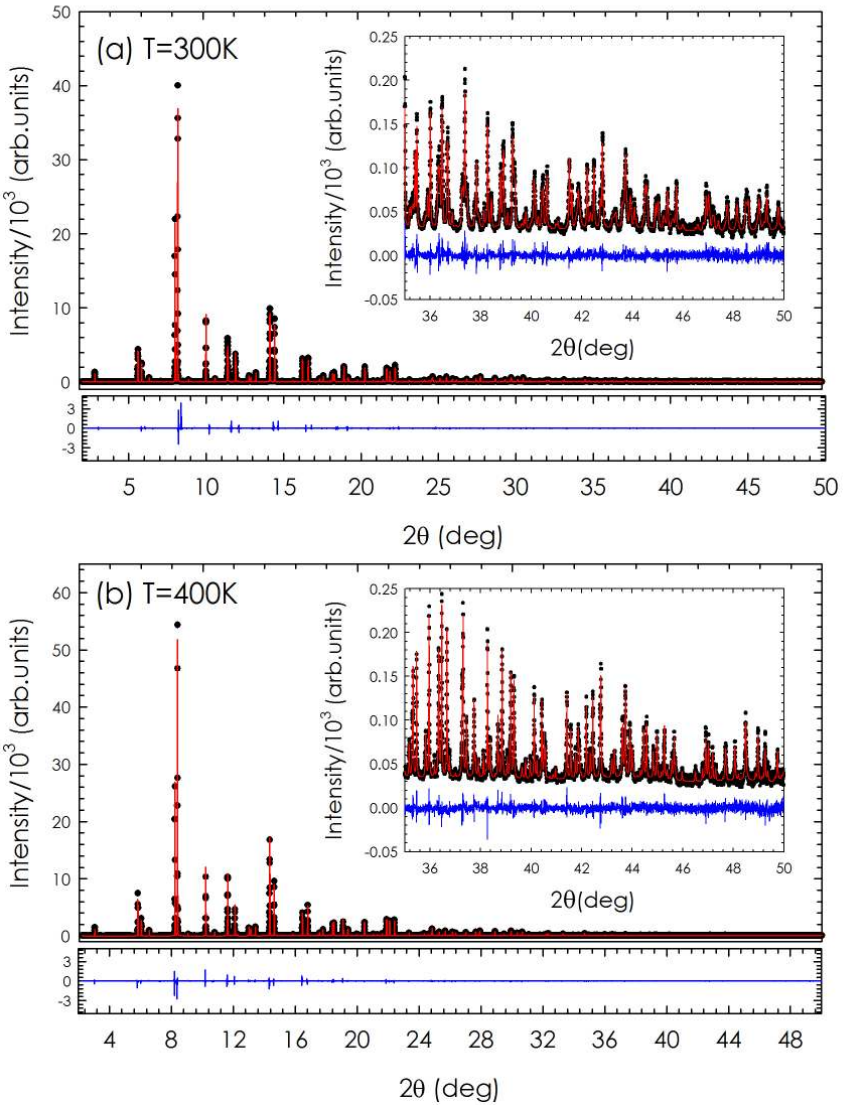

FIG 2.5 *(a) ,(b) Observed (dots) and calculated (lines) XRPD for $GdBaCo_2O_{5.0}$ at 300 K and 400K. Inset: high-angle diffraction peaks. The difference between the observed and fitted patterns is displayed at the bottom.*

In the final model, the isotropic thermal parameters of oxygen atoms were constrained to be the same. Good $R(F^2)$ values were obtained, testifying the suitability of the structural model.[46] Conversely, the *R*p values are quite high owing to the considerable narrowness of the instrumental resolution of the ID31 beamline. At T = 400 K,

$GdBaCo_2O_{5.0}$ has tetragonal structure with space group P4/*mmm* and cell metric $a_p \times a_p \times 2a_p$, a_p being the cubic perovksite lattice parameter.

Table 2.2 *Fractional atomic coordinates (dimensionless) and allowed thermal U_{ij} tensor parameters ($Å^2$) as obtained from least-square refinements on the SCD (first line: Pmmm, second line: P4/mmm) and XRPD (third line, Pmmm) diffraction data at room temperature. Esd's in parentheses*[2].

Atom	*x*	*y*	*z*	U_{eq}[3]	U_{11}	U_{22}	U_{33}
Gd	0.5000	0.5000	0.5000	0.0115(1) 0.0117(2) 0.0054(2)	0.0119(2) 0.0120(2) -	0.0116(2) 0.0120(2) -	0.0110(2) 0.0112(2) -
Co	0.0000	0.0000	0.2569(2) 0.2570(2) 0.2571(2)	0.0125(1) 0.0126(2) 0.0054(2)	0.0118(3) 0.0116(2) -	0.0112(3) 0.0116(2) -	0.0144(3) 0.0145(4) -
Ba	0.5000	0.5000	0.0000	0.0144(1) 0.0146(2) 0.0074(2)	0.0140(2) 0.0140(2) -	0.0137(2) 0.0140(2) -	0.0155(2) 0.0156(3) -
O1	0.0000	0.0000	0.0000	0.016(1) 0.017(2) 0.0113(8)	0.019(3) 0.020(3) -	0.020(3) 0.020(3) -	0.010(2) 0.010(3) -
O2	0.5000	0.0000	0.3093(6) 0.3095(5) 0.3098(12)	0.0153(8) 0.0156(7) 0.0113(8)	0.016(2) 0.016(2) -	0.017(2) 0.017(2) -	0.014(2) 0.014(1) -
O3[4]	0.0000	0.5000	0.3095(6) - 0.3063(12)	0.0150(8) - 0.0113(8)	0.016(2) - -	0.015(2) - -	0.014(2) - -

[2] Symmetry-constrained fractional coordinates are only once reported. Lacking entries (' - ') indicate that the corresponding parameters are not refined in the least-square model.

[3] When the atomic thermal motion is described as anisotropic, U_{eq} is defined as the 1/3 of the trace of the corresponding thermal tensor.

[4] In *P*4/*mmm* symmetry, O3 is symmetry-related with O2.

In Fig. 2.6 (*a*) the most relevant part of the diffraction patterns collected at 300 $\leq T \leq$ 400 K is shown, with the appropriate crystallographic indexes highlighted.

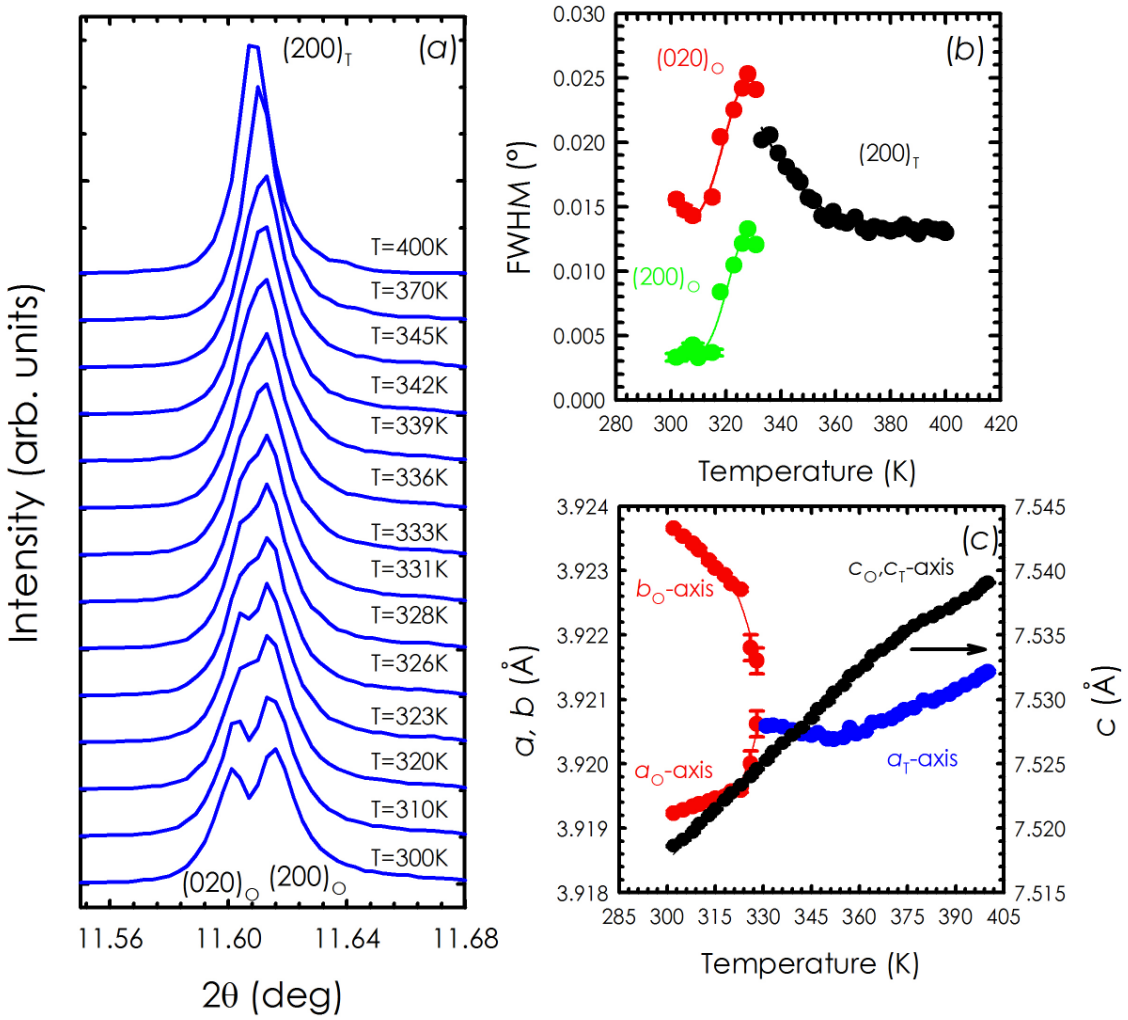

FIG 2.6 *(a) (200) and (020) diffraction peaks as a function of temperature. Subscripts 'T' and 'O' stand for 'tetragonal' and 'orthorhombic', respectively. (b) Evolution of the FWHM parameter of the (200) and (020) peaks for the orthorhombic and tetragonal phases. (c) Lattice parameters a, b (full grey dots: tetragonal phase; empty dots: orthorhombic phase) and c (black dots) of* $GdBaCo_2O_{5.0}$ *as a function of temperature. Continuous lines are guides for the eye.*

The $(200)_O$ and $(020)_O$ peaks, clearly resolved at lower T, belong to the orthorhombic *Pmmm* space group, and merge together at higher temperatures. Above T = 331 K they are no more distinguishable, as their difference in the d-space falls below the instrument resolution ($\Delta d/d \sim 10^{-4}$). Above the estimated Néel temperature (350 K), on the other hand, only the $(200)_T$ reflection indexed within a tetragonal unit cell is recognizable. It should be noted, however, that the full width at half maximum (FWHM) of the $(200)_T$ profile in tetragonal symmetry monotonically increases upon cooling from 360 to 330 K (Fig. 2.6(*b*)). In other words, some kind of structural distortions, clearly visible in the high-resolution powder diffraction pattern, are taking place around the Néel temperature. In any case, attempts to describe the $(200)_O$ peak in the 331 K < T < 350 K range using a multiple peak fitting were somewhat unsuccessful, as the individual profile shapes were at least questionable and sometimes clearly unphysical. These evidences seem to point out that the tetragonal-to-orthorhombic symmetry lowering is indeed coupled with the magnetic transition around the Néel temperature. [12] This conclusion is supported by inspecting the temperature evolution of the cell parameters (Fig. 2.6(*c*)). Interestingly, between 350 and 330 K the a axis follows a non-monotonous behavior featuring a very slight lengthening below 350 K, until the tetragonal symmetry is clearly broken below T = 330 K. Such an evidence, together with the above commented behavior of the $(200)_T$ linewidth, suggests that the reported magnetic transition is in fact coupled with structural changes, that in turn require some tens of kelvin to be fully exploited.

However, it should be noted that the structural phase transition is only *incipient* in close proximity of the reported T_N,[12,20] i.e. some kind of small bulk lattice distortions occur and affect the profile shape parameters in high-resolution powder diffractograms, without yet being able to cause a clearly measurable structural symmetry breaking until

$T \approx 331$ K. Interestingly, the $(200)_T$ FWHM starts to smoothly increase when $T < 364$ K, i.e. even above T_N (Fig. 2.6 (*b*)), while the slope of the crystallographic a_T axis vs. T clearly change sign just at $T \approx T_N$ (Fig. 2.6 (*c*)). In other words, the behavior of the a_T lattice parameter seems to be more closely coupled with the magnetic transition. Overall, it appears reasonable that the above mentioned distortions are somewhat related to small oxygen displacements in the unit cell, but their full rationalization is not straightforward. On the other hand, it is known that in $GdBaCo_2O_{5+\delta}$ with $\delta \approx 0.5$, the observed structural phase transitions in the $300 < T < 400$ K range are somewhat associated to electronic effects, and in particular, to orbital ordering.[18,47] A tentative explanation to account for the ~20 K discrepancy in the $\delta = 0$ compound between T_N and the temperature where symmetry definitely breaks down could reside in the mismatch between the local and long-range magnetic order in the $330 < T < 350$ K range. This hypothesis implies that between 350 and 364 K the spins of the paramagnetic phase are organized in small antiferromagnetic clusters which are suppressed at $T > 364$ K. From a structural point of view, local magnetic clustering can be associated to a sort of local symmetry breaking, where oxygen atoms undergo small displacements that locally lower the lattice symmetry from *P*4/*mmm* to *Pmmm*. Within this scenario, a further decrease of T below ~350 K allow this small magnetic clusters to grow in size, resulting in a transition from local to long-range magnetic ordering. As a consequence, the strength of the antiferromagnetic interactions gradually increases until a critical value (probably near 330 K) is reached; then, an overall structural lattice transition takes place. In other words, the lattice distortions observed in this temperature range could be associated with gradual localization of the spins due to the strengthening of the long range antiferromagnetic ordering upon cooling, that in turn implies a gradual splitting of the Bragg peaks. It should be also noted, however, that

other data should be collected, for example by means of dielectric spectroscopy and magnetic susceptivity measurements, to provide insights on the above sketched picture. Actually, it should be remarked that the structural distortions in the 330-350 K range detected by powder X-ray diffraction analysis are below the instrumental resolution. Therefore, it cannot be excluded that the long-range symmetry breaking occur at temperatures even higher than 330 K. We deserve to investigate this topic more in detail in subsequent works, as the full magnetic and electronic characterization of the *P*4/*mmm* to *Pmmm* phase transition in the title compound goes beyond the purposes of the present discussion.

2.7 Crystal structure of $GdBaCo_2O_{5.0}$

If the atomic positional and thermal parameters as obtained from both the SCD refinements ('orthorhombic' and 'tetragonal') at RT are compared (Table 2.2), no significant differences emerge, as within 2 esd's all the geometric and thermal parameters are perfectly identical. This was not truly surprising, if the results above described on the intensity equivalences of reflections in the reciprocal space are taken into account. On the other hand, conclusions drawn in the reciprocal lattice also hold true when the real lattice is considered. In particular, granted that the C_4 axis is removed, making the cell orthorhombic, the very closeness in lengths of *a* and *b* cell edges (*pseudo*-tetragonal lattice *metric*), together with essentially identical positions of the symmetry-independent O2 and O3 oxygen atoms in *Pmmm*, result in fact in a *pseudo*-C_4 lattice *symmetry*, which cannot be discriminated from a *true* C_4 one on the basis of the current precision provided by our SCD experiment.

In general, the XRPD results on atomic positions (Table 2.2) and next-neighbors distances (Table 2.3) also agree *quantitatively* with the SCD ones. The only significant

difference affects the Gd–O3 distance (Table 2.3), being 0.014 Å (~ 0.6 %) longer from the XRPD refinement. Such a deviation is due to the slightly different O3 *z* coordinate obtained from the XRPD and SCD data (Table 2.2). Nevertheless, the SCD outcome for *z*(O3) lies within a confidence interval of ± 3 esd's with respect to the XRPD estimate. Greater differences affect the isotropic equivalent displacement parameters of the metal atoms, U_{eq}, that are systematically lower (roughly halved) in the XRPD results. Anyhow, significant discrepancies among thermal motion parameters among the XRPD and SCD techniques are not uncommon,[48] as they depend critically on least-square strategy, data treatment and experimental settings.

Table 2.3 *Bond distances among symmetry-independent next-neighbor atoms in* $GdBaCo_2O_5$ *at RT as obtained from XRPD and SCD X-ray diffraction experiments. Esd's in parentheses.*

Atoms	*d* / Å (XRPD)	*d* / Å (SCD)	|Δ| %
Ba–O1	2.773(<1)	2.772(<1)	0.04
Gd–O2	2.428(5)	2.427(3)	0.04
Gd–O3	2.441(5)	2.427(3)	0.58
Co–O1	1.933(2)	1.930(1)	0.16
Co–O2	1.999(2)	1.999(1)	0.00
Co–O3	1.997(2)	1.999(1)	0.10

2.8 Conclusion

In conclusion, we have shown the usefulness of the joint approach by SCD and XRPD techniques to gain insight into the average *cell metric* and *crystal symmetry* of the title compound to a high level of accuracy and precision. Because of the very small

distortions coupled with the PM-AF transition in $GdBaCo_2O_{5.0}$ around T_N, that imply only minor displacements of the O3 oxygen atoms, SCD data alone do not provide enough evidence for justifying the choice of the less symmetric orthorhombic Bravais lattice, as the higher tetragonal symmetry fits equally well the observed diffraction pattern. Therefore, according to commonly accepted conventions for selecting the proper crystallographic system, SCD data would definitely describe the structure as *tetragonal* at RT in terms of both lattice metrics and equivalent reflection intensity statistics. HRXPRD outcomes, on the contrary, provide compelling evidence that the metric is in fact *orthorhombic* below T_N, with deviations of *a* and *b* axis lengths not exceeding 0.14 %. Nevertheless, it is worth noting that the SCD technique has some interesting advantages with respect to XRPD. First, it allows solving *ab initio* the crystal structure of $GdBaCo_2O_{5.0}$, whereas at least a guess model is necessary to start a Rietvield-based refinement against powder data. Obviously, in the present case this is not a particularly serious problem, as one can safely use the known structure of other rare-earth cobaltites as a starting point, but this fact can undoubtedly turn out to be useful when totally or partially unknown structures are examined. Second, the estimated standard deviations affecting bond distances (Table 2.3) are significantly lower (on average, ≈ 1/2) when estimated by SCD than by XRPD. Eventually, SCD provides reliable estimates of anisotropic atomic thermal motion (and, hence, coordination geometries that are likely to be a bit more accurate). Finally it is important to stress that the occurring of a tetragonal-to-orthorhombic transition around T_N even in the stoichiometric oxygen-deficient $GdBaCo_2O_{5.0}$ system implies that the symmetry lowering can be brought about not only by oxygen insertion within the Gd layer, as it could be inferred from the discussion at page 6 of the work by Taskin *et al*.,[12] but it can

be also the consequence of an intrinsic structural distortions somewhat coupled with magnetic and electronic or orbital transitions.

References

[1] M. Meinert, J.-M. Schmalhorst and G. Reiss, Appl. Phys. Lett. **97**, 012501 (2010).

[2] J.–E. Jørgensen and L. Keller, Eur. Phys. J. B **66**, 445 (2008).

[3] M. Reehuis, C. Ulrich, P. Pattison, M. Miyasaka, Y. Tokura and B. Keimer, Eur. Phys. J. B **64**, 27 (2008).

[4] F. Fauth, E. Suard, V. Caignaert, B. Domengès, I. Mirabeau and L. Keller, Eur. Phys. J. B **21**, 163 (2001).

[5]C. Martin, A. Maignan, D. Pelloquin, N. Nguyen and B. Raveau, Appl. Phys. Lett. **71**, 1421 (1997).

[6] A. A. Taskin, A. N. Lavrov and Y. Ando, Phys. Rev. Lett. **90**, 227201 (2003).

[7] D. Liao, M. R. Lees, G. Balakrishnan and D. McK. Paul, J. Phys. Conf. Ser. **200**, 012104 (2010).

[8] B. Raveau, MD Motin Seikh, V. Pralong and V. Caignaert, Bull. Mater. Sci. **32**, 305 (2009).

[9] C. Frontera, J. L. Garcia-Muñoz, A. Llobet, M. A. G. Aranda, J. Rodriguez-Carvajal, M. Respaud, J. M. Broto, B. Raquet, H. Rakoto and M. Goiran, Journal of Alloys and Compounds **323-324**, 468 (2001).

[10] W. Wang, T. S. Peh, S. H. Chan and T. S. Zhang, ECS Transactions **25**, 2277 (2009).

[11] E. Chavez., M. Mueller, L. Mogni and A. Caneiro, J. Phys. Conf. Ser. **167**, 012043 (2009).

[12] A. A. Taskin, A. N. Lavrov and Y. Ando, Phys. Rev. B **71**, 134414 (2005).

[13] P. S. Anderson, C. A. Kirk, J. Knudsen, I. M. Reaney and A. R. West, Solid State Science **7**, 1149 (2005).

[14] Y. Moritomo, M.Takeo, X. J. Liu, T. Akimoto and A. Nakamura, Phys. Rev. B **58**, R13334 (1998).

[15] I. O. Troyanchuk, D. D. Khalyavin, T. K. Solovykh, H. Szymczak, Q. Huang and J. W. Lynn, J. Phys: Condens. Matter **12**, 2485 (2000).

[16] I. O. Troyanchuk, N. V. Kasper, D. D. Khalyavin, A. N. Chobot, G. M. Chobot and H. Szymczak, J. Phys.: Condes. Matter **10**, 6381 (1998).

[17] S. Roy, M. Khan, Y. Q. Guo, J. Craig and N. Ali, Phys. Rev. B **65**, 064437 (2002),

[18] T. Vogt, P. M. Woodward, P. Karen, B. A. Hunter, P. Henning and A. R. Moodenbaugh, Phys. Rev. Lett., **84**, 2969 (2000).

[19] F. Mitchell, J. Burley and S. Short, J. Appl. Phys. **93**, 7364 (2003)

[20] X. S. Wu, H. L. Zhang, J. R. Su, C. S. Chen and W. Liu, Phys. Rev. B **76**, 094106 (2007)

[21] S. Bhagavantam and D. Suryanarayana, Acta Cryst. **2**, 21 (1949).

[22] Z. W. Ouyang, F. W. Wang, Q. Huang, W. F. Liu, Y. G. Xiao, J. W. Lynn, J. K. Liang and G. H. Rao, Phys. Rev. B **71**, 064405 (2005).

[23] M. Garcia-Fernández, V. Scagnoli, U. Staub, A. M. Mulders, M. Janousch, Y. Bodenthin, D. Meister, B. D. Patterson, A. Mirone, Y. Tanaka, T. Nakamura, S. Grenier, Y. Huang and K. Conder, Phys. Rev. B **78**, 054424 (2008).

[24] D. D. Khalyavin, S. N. Barilo, S. V. Shiryaev, G. L. Bychkov, I. O. Troyanchuk, A. Furrer, P. Allenspach, H. Szymczak and R. Szymczak, Phys. Rev. B **67**, 214421 (2003).

[25] Y. Moritomo, T. Akimoto, M. Takeo, A. Machida, E. Nishibori, M. Takata, M. Sakata, K. Ohoyama and A. Nakamura, Phys. Rev. B **61**, R13325 (2000).

[26] *Encyclopædia Britannica. Encyclopædia Britannica Online*. Encyclopædia Britannica. Retrieved from http://www.britannica.com/EBchecked/topic/545924/single-crystal (2011).

[27] L. Lo Presti, D. Invernizzi, R. Soave and R. Destro, Chem. Phys. Lett. **416**, 28 (2005).

[28] D. M. Wang, J. B. He, T.-L. Xia and G. F. Chen, Phys. Rev. B **83**, 132502 (2011).

[29] Z. T. Zhang, Z. R. Yang, L. Li, C. J. Zhang, L. Pi, S. Tan and Y. H. Zhang, J. Appl. Phys. **109**, 07E113 (2011)

[30] A. C. Larson and R. B. Von Dreele, General Structural Analysis System (GSAS). Los Alamos National Laboratory Report LAUR 86 (2004).

[31] B. H. Toby, J. Appl. Cryst. **34**, 210 (2001).

[32] N. N. Lobanov and L. Alte da Veiga, 6th European Powder Diffraction Conference P12-16 (1998).

[33] P. Thompson, D. E. Cox and J. B. Hastings, J. Appl. Crist. **20**, 79 (1987).

[34] L. W. Finger, D. E. Cox and A. P. Jephcoat, J. Appl. Crist. **27**, 892 (1994).

[35] XEMP - EMPIRICAL ABSORPTION CORRECTIONS - v4.2 Siemens Analytical Xray Inst. Inc. (1990).

[36] G. M. Sheldrick, Acta Cryst. A **64**, 112 (2008).

[37] V. Hansen, B. Hauback, M. Sundberg, Chr. Rømming and J. Gjønnes, Acta Cryst. B54, 351 (1998)

[38] J. B. Parise, C. C. Torardi, M. A. Subramanian, J. Gopalakrishnan, A. W. Sleight, E. Prince, Physica C 159 (1989) 239.

[39] M. T. Weller, P. F. Henry, M. E. Light, Acta Cryst. **B63**, 426 (2007).

[40] J. A. Armstrong, H. Friis, A. Lieb, A. A. Finch, M. T. Weller, American Mineralogist **95**, 519 (2010).

[41] N. A. Tumanov, E. V. Boldyreva and H. Ahsbahs, Powder Diffraction, **23**, 307 (2008).

[42] P. N. Gates, H. C. Knachel, A. Finch, A. V. Fratini, A. N. Fitch, O. Nardone, J. C. Otto and D. A. Snider, J. Chem. Soc. Dalton Trans. 2719 (1995).

[43] W. I. F. David and K. Shankland, Acta Cryst. A **64**, 52 (2008).

[44] G. M. Loiacono, G. Kostecky and J. S. Jr. White, American Mineralogist **67**, 846 (1982).

[45]T. N. Moroz and N. A. Palchik, Crystallography Reports **54**, 734 (2009).

[46] B. H. Toby, Powder Diffraction **21**, 67 (2006).

[47] Yu. P. Chernenkov, V. P. Plakhty, V. I. Fedorov, S. N. Barilo, S. V. Shiryaev and G. L. Bychkov, Phys. Rev. **B 71**, 184105 (2005).

[48] T. Bataille and D. Louër, Acta Cryst. B **56**, 998 (2000).

3. Spin-lattice interaction in $GdBaCo_2O_{5+\delta}$

As reported in Chapter 2, the possibility of tuning with great accuracy the effective oxygen content (δ) in the $GdBaCo_2O_{5+\delta}$ structure provides the opportunity to control several macroscopic key features such as the resistivity. This is the case of the temperature induced insulator-to-metal transition (IMT) found when $\delta \sim 0.5$.

Chapter 3 presents our work on the IMT of $GdBaCo_2O_{5+\delta}$ samples in the δ range $0.54(1) \leq \delta \leq 0.63(1)$ performed by using a combined approach by electron paramagnetic resonance (EPR) and powder diffraction techniques. The EPR linewidth markedly changes across IMT and its temperature evolution can be explained considering spin state transition involving Co ions. The temperature dependences of the EPR linewidth and of the *a* lattice parameter fairly overlap to each other suggesting spin-lattice interaction along the same crystallographic direction of the reported *Ising*-Like spin anisotropy [A. A. Taskin et al., Phys. Rev. Lett. **90**, 227201 (2003)]. A possible mechanism describing the interplay between this strong spin-lattice interaction and IMT is proposed. These results will be published in reference: M. Allieta, C. Oliva, M. Scavini, S. Cappelli, E. Pomjakushina, and V. Scagnoli, Phys. Rev. B, accepted, (2011).

3.1 Introduction

Ln$BaCo_2O_{5+\delta}$ layered cobalt oxides (*Ln* is a rare earth element) exhibit very rich electronic and magnetic phase diagrams that involve many fascinating phenomena like magnetoresistance (MR) effect.[1-3] The crystal structure of *Ln*$BaCo_2O_{5+\delta}$ can be viewed as a sequence of square-lattice layers [CoO_2][BaO][CoO_2][*Ln*O_δ] stacking along *c* axis

with alternation of two types of coordination environments for cobalt ions, *i.e.* CoO_5 pyramid (Co_{pyr}) and CoO_6 octahedra (Co_{oct}). The Co_{pyr} / Co_{oct} ratio as well as their ordering along crystallographic directions can be modified by tuning the oxygen concentration δ in LnO_δ planes.[2] More importantly, δ affects the mean valence state of cobalt ions as Co^{3+} can exist in low-, intermediate-, or high-spin state (LS, IS or HS) whilst Co^{2+} and Co^{4+} are stable in HS and LS configurations, respectively.[2] Then, the physics of these systems is driven by a complex interplay between charge, spin, orbital and lattice degrees of freedom triggered, *e.g.*, by temperature.

Such behavior is clearly demonstrated by the temperature induced insulator-to-metal transition (IMT) found at T_{IM}≈365 K with $GdBaCo_2O_{5+\delta}$ when δ≈0.5.[1-5] However, despite a number of experimental and theoretical studies in layered cobaltites, great controversy has arisen regarding the Co spin state and the microscopic origin of IMT. In the year 2000, Moritomo *et al.*[6] suggested that the IMT is induced by a spin state transition (SST) from an orbital ordered (OO) IS state to the HS state in both Co_{pyr} and Co_{oct} sites, basing their consideration on neutron powder diffraction of $TbBaCo_2O_{5.5}$. Later, a synchrotron radiation X-ray powder diffraction (XRPD) study of $GdBaCo_2O_{5.5}$ ruled out any OO, suggesting that the IMT should be related to spin-state switch from LS to HS states at Co_{oct}. Conversely, the Co_{pyr} should remain in IS state at both sides of the IMT.[4] This is consistent with *ab initio* calculations that verified the stability of pyramidal IS states in $LnBaCo_2O_{5.5}$ systems.[7] Maignan *et al.*[8] explained the interplay between IMT and SST using a model based on conversion of HS to LS state in Co_{oct} at $T<T_{IM}$ which would immobilize the electron charge carriers through a "spin blockade" mechanism between $HSCo^{2+}$ and $LSCo^{3+}$. In strong contrast with SST, muon-spin relaxation study on $LnBaCo_2O_{5+\delta}$ δ≈0.5 suggested that the HS state of Co^{3+} is retained at T<300 K.[9] Recently thermal expansion measurements on $GdBaCo_2O_{5.5}$ confirmed

the SST as the driving force for IMT excluding the occurrence of stepwise SST at lower temperatures.[5] Another model based on density functional theory calculations[10] and supported by photoemission[11] and isotope-effect neutron diffraction data[12] suggested that the IMT is due to hole delocalization in the Co^{3+} HS state rather than to SST.[10,12]

In the following the first EPR study on $GdBaCo_2O_{5+\delta}$ combined with synchrotron XRPD as a function of δ and of the temperature across the IM transition is presented. EPR spectroscopy allows a direct access to the spin-environment interactions through the investigation of the spin relaxation behavior.[13]

3.2 Sample preparation

$GdBaCo_2O_{5+\delta}$ was synthesized by conventional solid state reaction technique[14] and the desired oxygen content was adjusted on three aliquots according to annealing conditions and thermal treatments reported by Taskin *et al.*[2] The oxygen content was determined by using the thermogravimetric (TG) reduction procedure as outlined in Ref.15. In particular, in the TG reduction the sample is heated up to 950°C with a rate of 2°C/min in a reducing atmosphere (He with 5% H_2) and from the weight loss the oxygen content in the starting sample can be calculated. The δ=0.54(1), δ=0.57(1) and δ=0.63(1) values were found for the three prepared samples.

3.3 Diffraction experiment and results

Diffraction patterns were collected at the ID31 beamline of the European Synchrotron Radiation Facility (ESRF) in Grenoble. For each sample, 40 diffraction patterns were collected in the $0 < 2\vartheta < 20°$ range from 300 K to 400 K selecting a wavelength of

λ=0.39620(5) Å. Moreover, some high quality diffraction patterns were collected at λ=0.35422(1) Å for a total counting time of 1 hour at selected *T* between 300 K and 400 K depending on sample composition. Data were analyzed using Rietveld method as implemented in GSAS software suite.[16] All the data sets have been refined against the *Pmmm* model derived from the cubic perovskite by doubling along the *b* and *c* axes ($a_c \times 2a_c \times 2a_c$ unit cell, where a_c stands for the cell parameter of the cubic perovskite lattice).[4] To account for the actual δ values in structural models, we located the extra oxygen ions (with respect to δ=0.5) at the 1*c* (0,0,1/2) position considering the 1*g* (0,1/2,1/2) fully occupied. This is equivalent to consider an ordered alternation of Co_{pyr} and Co_{oct} along the [010] direction for δ=0.5.[1,4,6,17] The Rietveld refinements in selected portions of the diffraction patterns collected at various temperatures for δ=0.54(1) and δ=0.57(1) samples are shown in Fig. 3.1. Figure 3.2 shows the refined lattice for all the samples.

The presence of splitting in the diffraction profile of (040), (020) and (002) peaks is evident for δ=0.54(1) and δ=0.57(1) in a narrow *T* range (~7-8 K) below T_{IM}~365 K[1-5] as shown in Fig.3.1. This phase transition in the proximity of IMT is well known to occur in $LnBaCo_2O_{5.5}$[4,6,12,18] and the presence of peak splitting in the XRPD patterns are related to coexistence of the low- and high-*T* structural phases. The latter finding provides evidence for the first order of the transition.[18] As shown in Fig.3.2, with increasing *T* toward IMT, both *b* and *c* lattice parameters exhibit a step-like increase while *a* sudden shrinks for both δ=0.54(1) and δ=0.57(1) samples. No phases coexistence was evidenced by the XRPD patterns of δ=0.63(1) sample, since *b* and *c* linearly increase in $300 \leq T \leq 400$ K range and *a* decreases up to *T*~325 K.

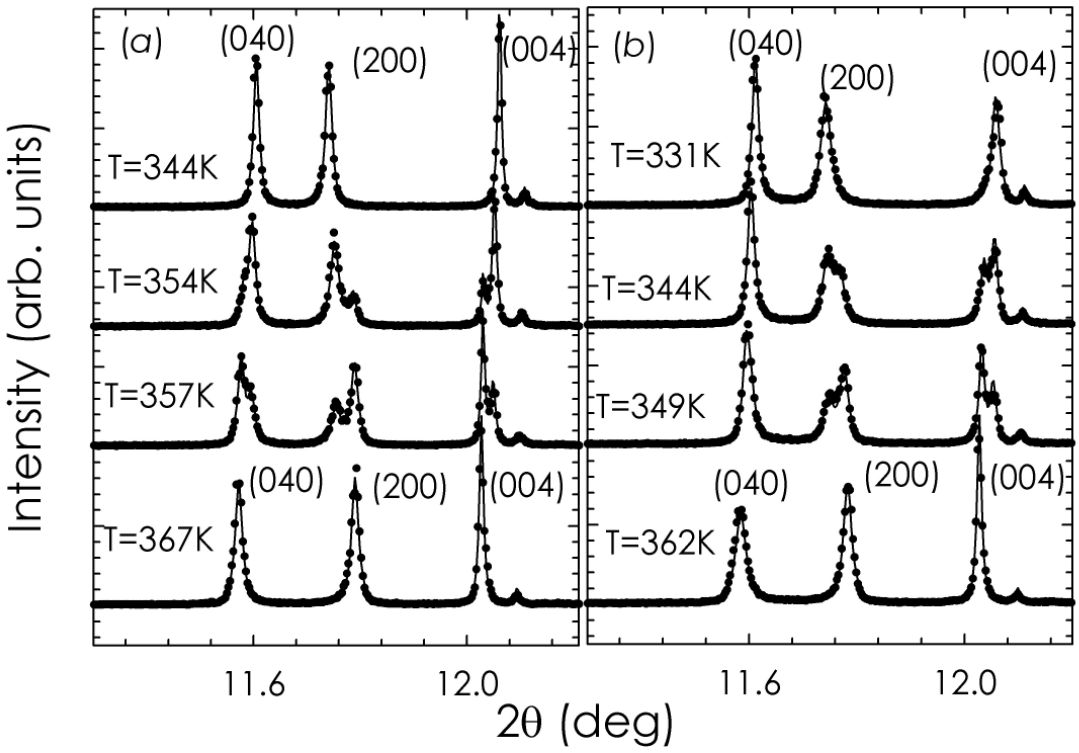

FIG. 3.1 *(a), (b) are selected region of XRPD patterns as collected at different temperatures for the δ=0.54(1) and δ=0.57(1) samples. The black dots are the experimental data while the continuous lines are the results from Rietveld refinements. The Miller indexes of the diffraction peaks are also reported. Typical agreement factor* $R(F^2)$ *between observed and calculated XRPD patterns are ranged from 0.06 to 0.08.*

The anisotropic thermal expansion of the unit cell parameters results in a variation of the unit cell volume. By comparing unit cell volume values as a function of T and δ reported in the insets of Fig.3.2, we note that the discontinuity which holds for first order transition is clearly apparent only for δ=0.54(1). This provides an indication that the order of the structural phase transition may change from the first to second order upon increasing δ.

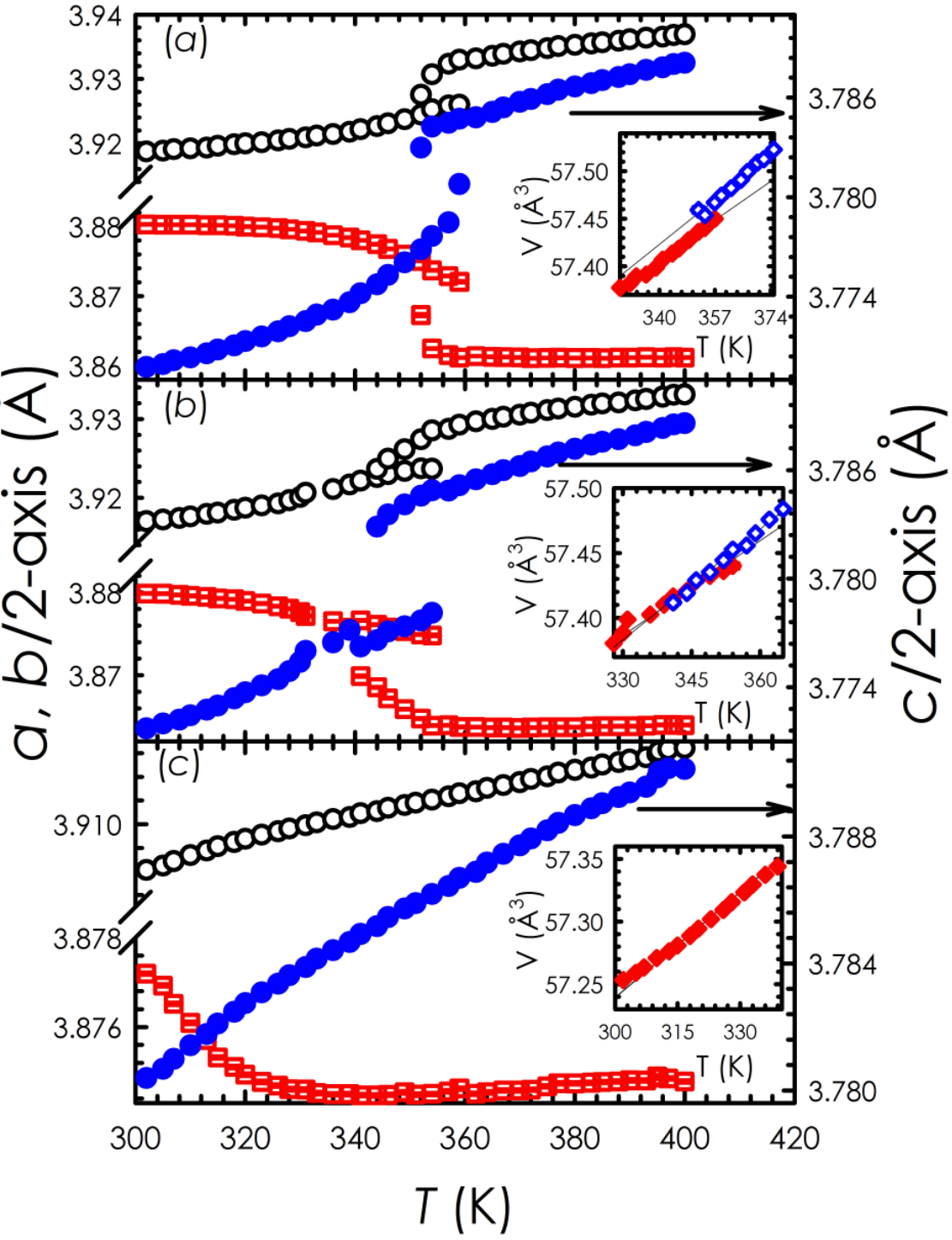

FIG. 3.2 *(a), (b), (c) Lattice parameters a (empty squares), b/2 (empty circles) and c/2 (black circles) as a function of temperature are displayed for the δ=0.54(1), 0.57(1) and 0.63(1), respectively. In the insets the temperature dependence of the unit cell volume are reported in selected temperature range.*

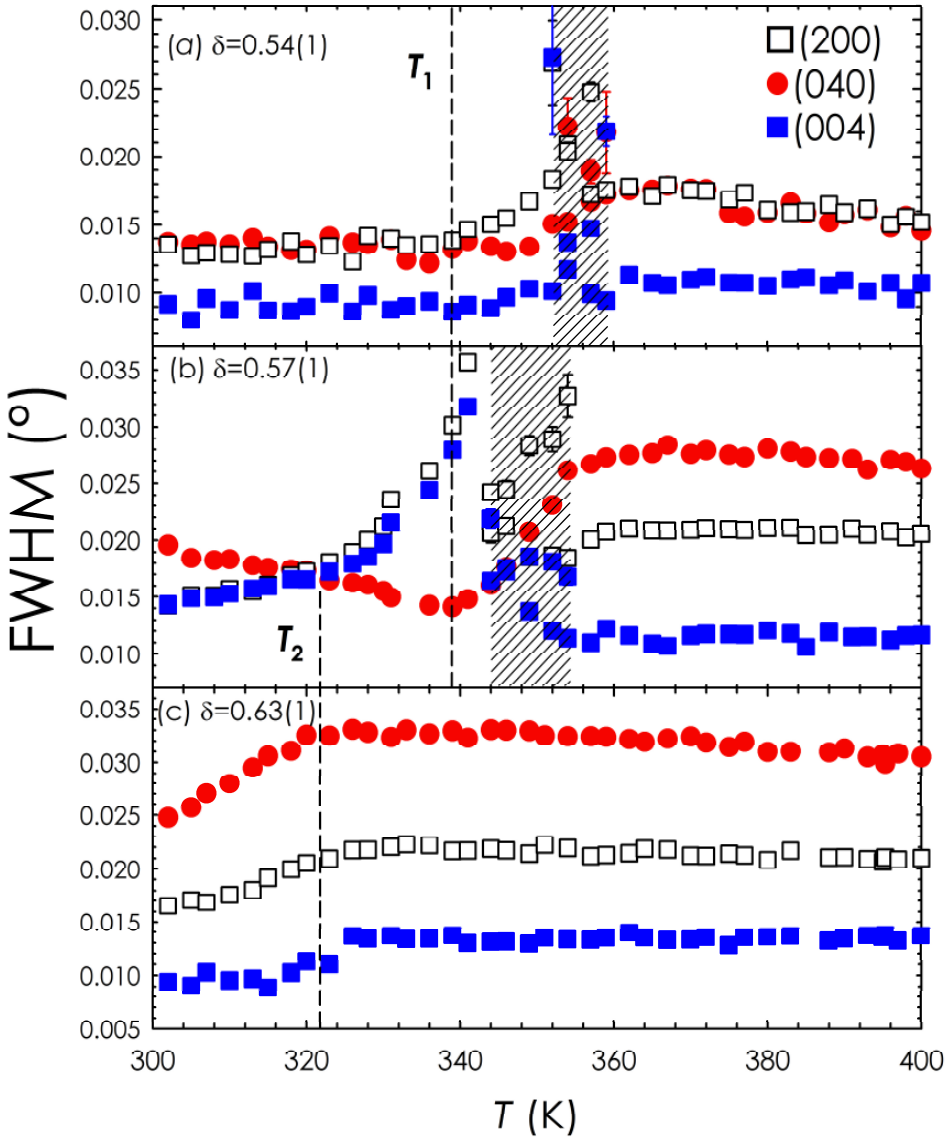

FIG. 3.3 *(a), (b), (c) Temperature evolution of the FWHM parameter of the (040) (full circles), (200) (empty squares) and (004) (full squares) peaks referring to the δ=0.54(1), 0.57(1) and 0.63(1) sample composition. Dashed boxes in panels indicate the temperature range where a biphasic structural model was employed whereas the dashed lines in right panels refer to FWHM anomalies at T_1 and T_2, respectively.*

We decided to analyze the thermal dependences of FWHM of (040), (200), (004) for all the samples. However, these results shown in Fig.3.3 were not included in the discussion session.

As shown in Fig.3.3, the thermal dependence of FWHM is very rich and complex depending on δ composition. For δ=0.54(1) we note that at T~300 K the FWHM related to (040) and (200) display the same value higher than the FWHM of (004). With increasing temperature FWHMs of (040) and (004) remain roughly constant up to the onset of the phase transition T~354K and change abruptly in the biphasic region. The FWHM of (200) shows a different behavior increasing steeply at T_1~340K. At T>357K all the FWHM values show weak T dependence.

At T=300K the FWHM of (200) and (004) peaks of δ=0.57(1) sample are very similar in value and increasing T one can clearly appreciated that for T<344K the T evolution of FWHM of (200) and (004) is almost the same. A linear broadening up to T_2=325K for FWHM of (200) and (004) is observed and for $T>T_2$ the FWHM abruptly increases reaching the lower limit of the biphasic region. The FWHM of (040) shows a completely different behavior. It linearly decreases up to T_1 and increases steeply at the biphasic region. For δ=0.63(1) the thermal evolution of FWHM is less complex than the other samples. At T=300K the FWHM related to (200), (040) and (004) peaks display different values and with increasing T the FWHMs of (020) and (004) peaks seem to increase up to T_2. On the other hand, FWHM of (004) is roughly constant showing an upturn at T_2.

3.4 EPR experiment and results

EPR measurements were performed at a Bruker ELEXSYS spectrometer equipped with an ER4102ST standard rectangular cavity at X band (9.4 GHz) frequency in the temperature range 305-450 K every 5 K. Powdered samples were placed into quartz tubes and the derivative dP/dH of power P absorbed was recorded as a function of the static magnetic field H.

In Fig. 3.4 we show EPR spectra as a function of temperature for δ=0.54(1) sample, as an example.

The signal consists of a single broad resonance line. It is well known that the Co^{3+} EPR signal cannot be observed because of a too short relaxation time[19] so that the EPR signals in $GdBaCo_2O_{5+\delta}$ can be originated from the shift and/or broadening of the Gd^{3+} resonance caused by exchange interaction $J_{fs}\boldsymbol{S}\cdot\boldsymbol{s}$ between localized 4f electron spin ($\boldsymbol{S}$) and the spins ($\boldsymbol{s}$) of the transition metal.[13]

At each temperature, the spectra were well fitted by a single Dysonian lineshape[20] shown as a solid line in the inset of Fig.3.4. However, meaningless negative dispersion-to-absorption α contributions were evaluated in these EPR features. By comparing our spectra with Dysonian line reported in the literature for another perovskitic system[21], we found that the EPR features measured by us correspond only to a part of the literature reported line.[21]

In particular, the left lobe of EPR spectrum shown in the inset of Fig. 3.4 is too broad to be fully observable. This leads to unreliable numerical values of the x_0 (peak position), α or w (linewidth) parameters. Another possible reason could be the presence of multiple signals as reported for other Co-based oxides.[22] However, attempts by linear combinations of Lorentzian and Gaussian functions gave no improvement to the lineshape description. We decided to extract the peak-to-peak linewidth (ΔH_{pp}) by direct observation of the experimental patterns as indicated in the inset of Fig.3.4. The trend of ΔH_{pp} with temperature is shown in Fig. 3.5 (*a*)-(*c*) for all the samples. It should be noted that in our spectra the baseline is not well defined and, hence, we cannot determine directly the peak position.

ΔH_{pp} shows three different temperature-dependent regions for δ=0.54(1) and δ=0.57(1):

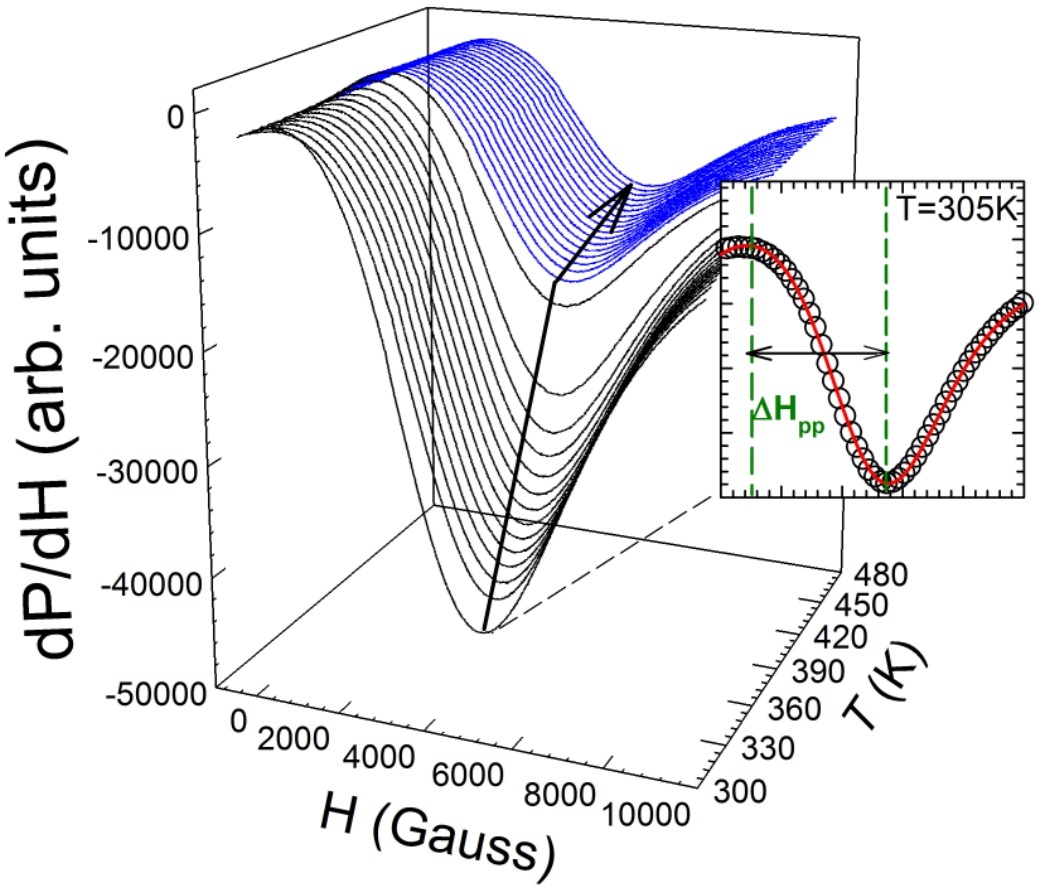

FIG. 3.4 *EPR spectra of the δ=0.54(1) sample as a function of temperature. The arrow outlines their trend with increasing temperature and in particular at the critical temperature T_c~365 K. In the inset an example of fit using a Dysonian line shape is shown (empty dots: observed data; solid line: fit).*

(*i*) it is roughly constant or decreases smoothly between 300 K and 330 K; (*ii*) it decreases steeply for ~330<T<~360 K toward the critical temperature T_c; (*iii*) it exhibits a distinct kink at T_c=360±5 K, then approaching constant values up to T=450 K. The behavior of ΔH_{pp} is rather different for the δ=0.63(1) sample, showing a smaller ΔH_{pp} value at T=300 K with just a weak decrease at T_c~325 K. All the samples display

a similar ΔH_{pp} value at $T > T_c$. In Fig. 3.5 (*d*) we compare the T_c with the T_{IM} values determined by Taskin *et al.* for δ=0.50 and δ=0.65 from resistivity measurements.[2] The good agreement between the two critical temperatures as a function of δ indicates that the EPR line-width change at T_c is consistent with the IM transition. $T_c = T_{IM}$ will be considered hereinafter.

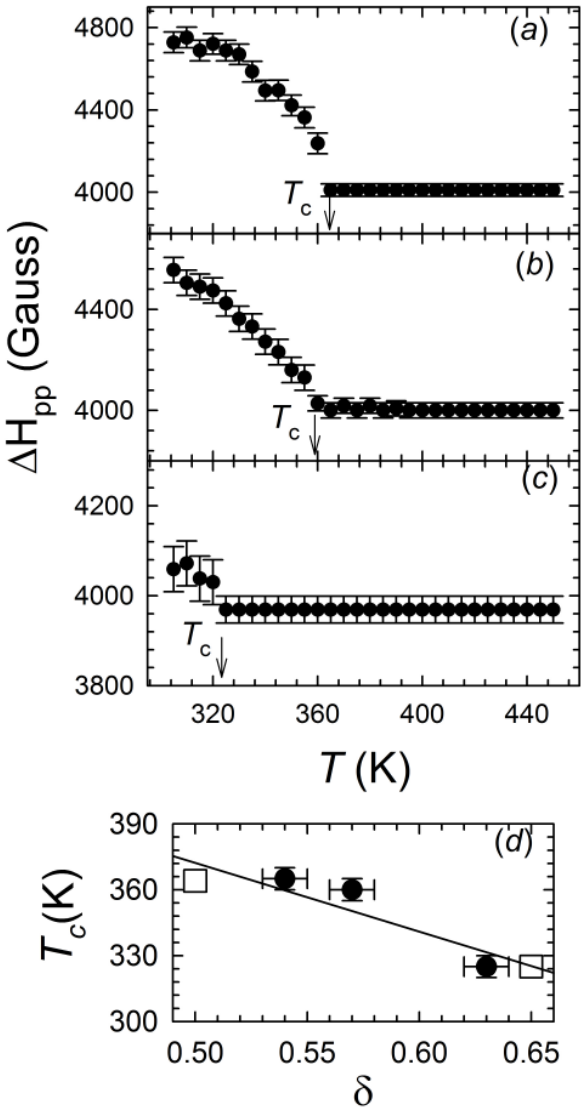

FIG.3.5 *(a), (b), (c) report ΔH_{pp} against temperature for δ=0.54(1), δ=0.57(1) and δ=0.63(1), respectively. (d) The T_c (full circles) highlighted in panels (a), (b), (c) are compared with T_{IM} reported by Taskin et al.[2] (empty squares).*

3.5 Discussion

According to magnetization measurements performed by Respaud *et al.*[17] on $GdBaCo_2O_{5.54(3)}$ sample, a drastic change in the Weiss-Curie temperature Θ_{WC} and effective cobalt magnetic moment was observed above T_{IM}.

In order to estimate the strength of the magnetic interactions involved, we calculated the value of the isotropic exchange constants (J) using the molecular field theory for 3D systems using the following molecular field equation[23]:

$$J = \frac{3k_B\Theta_{WC}}{2ZS(S+1)} \tag{3.1}$$

where k_B is the Boltzmann constant, Z is the number of nearest neighbors and S is the spin quantum number.

We assumed the model proposed by Taskin et *al.*[1,2] in which the magnetic interactions are generated by IS-Co^{3+} and we used the modulus of the values of Θ_{WC} reported below and above the IMT, i.e. $|\Theta_{WC}|$~ 275 K and $|\Theta_{WC}|$~ 600 K.[17] By considering S=1 for IS-Co^{3+} and Z=3, i.e. by counting only for nearest neighbors, we estimated $|J_{ins}|/k_B$~69 K and $|J_{met}|/k_B$~150 K in the insulating and metallic phases, respectively. This corresponds to a ratio of $|J_{met}|/|J_{ins}|$~2 indicating that the isotropic exchange interactions between cobalt ions increase above T_{IM}.

In the case of strong isotropic exchange interactions the Gaussian EPR linewidth is narrowed into a Lorenztian line with ΔH_{pp} given by[23,24,25]:

$$\Delta H_{pp} = \frac{\hbar M_2}{g\mu_B\omega_{ex}} \tag{3.2}$$

where $\omega_{ex} \sim J/\hbar$ is the frequency of the isotropic exchange interactions caused by the Heisenberg hamiltonian $H_{ex}^{ij}(=Js_i s_j)$ between neighboring spins s_i and s_j. It should be noted that, in the case of an asymptotic regime, as observed at $T \rightarrow 300$ K and at $T > T_{IM}$ for $\delta=0.54(1)$ and $\delta=0.57(1)$ samples, both the second moment M_2 and the exchange frequency ω_{ex} are temperature independent. Basically, the equation (3.2) can be employed to explain that the ΔH_{pp} asymptotic value at $T > T_{IM}$ in the metallic phase is smaller than that reached at $T \rightarrow 300$ K in the insulating phase. According to the equation, above T_{IM} the decreasing of ΔH_{pp} can be justified by an increase of the frequency of the isotropic exchange interactions ω_{ex} and/or by a decrease in the second moment M_2. As a matter of fact, M_2 parameter depends on anisotropic exchange interactions and can be determined by measuring the angular dependence of EPR line width or *g*-factor as a function of several orientations of a single crystal sample in the external magnetic field.[26] As we deal with powdered samples, we cannot resolve the anisotropy of the EPR spectra and, hence, we cannot say anything about the influence of such parameter to explain the strong narrowing. On the other hand, from $\omega_{ex} \sim J/\hbar$ we can scale the J ratio accordingly and deduce that $\omega_{ex}^{met} > \omega_{ex}^{ins}$. Thus, the observed temperature decreasing of the ΔH_{pp} above T_{IM} is compatible with an enhancement of the isotropic exchange frequency term in the metallic phase.

According to the model proposed by Maignan *et al.*,[8] the increase of spin-spin exchange frequency observed at $T > T_{IM}$ in $\delta=0.54(1)$ and $\delta=0.57(1)$ samples can be easily understood as an increasing of hopping probability of 3d electrons between nearest-neighbor Co ions. The metallic state is interpreted as the motion of an extra electron from an excited $HSCo^{2+}$ ion to a HS or to an IS Co^{3+} ion.[8] However this model does not explain how Co^{2+} are created and does not consider that a motion of one e_g

electron from $HSCo^{3+}$ to $ISCo^{3+}$ would generate an unstable non-$LSCo^{4+}$. To avoid the production of such cobalt species, we suppose that the Co^{3+}_{oct} sites in the metallic phase of an ideal δ=0.5 sample display IS state together with a *T* independent $ISCo^{3+}_{pyr.}$[4] It should be noted that e_g electron hopping from an $ISCo^{3+}_{oct}$ to the next $ISCo^{3+}_{oct}$ along the *a* and *c* axes and/or to the next $ISCo^{3+}_{pyr}$ along the *b* axis generates in any case a couple of $LSCo^{4+}$ and $HSCo^{2+}$ stable species. For example the electron transfer along the *b*-axis from Co_{pyr} to Co_{oct} and *viceversa* can be sketched as: $t_{2g}^5 e_g^1$-$ISCo^{3+}_{pyr} + t_{2g}^5 e_g^1$-$ISCo^{3+}_{oct} \rightarrow t_{2g}^5 e_g^0$-$LSCo^{4+}_{pyr} + t_{2g}^5 e_g^2$-$HSCo^{2+}_{oct}$ (Fig.4.6).

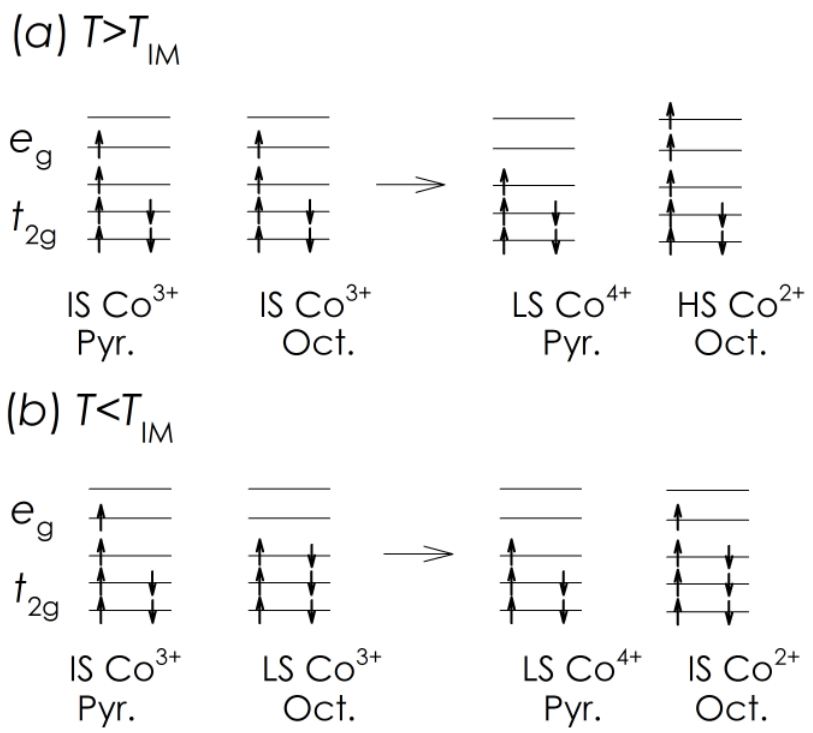

FIG.4.6 *Schematic electronic level diagram of Co in* $GdBaCo_2O_{5.5}$ *showing the processes of* e_g *electron hopping. In the left side of (a), (b) the* e_g *electron transfers from pyramidal to octahedra Co sites are displayed in the metallic and insulating phases, respectively. In the right side of the same panels the diagram related to cobalt species generated after the hopping processes are shown.*

This process justifies high ω_{ex} above T_{IM} since the presence of $LSCo^{4+}_{pyr}$ and $HSCo^{2+}_{oct}$ implies double exchange (DE) interaction between $LSCo^{4+}_{pyr}$ and $HSCo^{2+}_{oct}$ and $ISCo^{3+}_{oct/pyr}$ ions occurring along the *b*-axis. At the same time, the formation of e_g conduction band of IS character gives rise to the observed metallic ground state since DE paths formed by the 3D network of $ISCo^{3+}_{oct/pyr}$ account for electronic delocalization in all directions. Upon cooling below T_{IM}, a SST from IS to LS state can occur solely at Co^{3+}_{oct} while the Co^{3+} in pyramid remains in IS state.[4] Within this spin configuration, t_{2g} electron hopping from $LSCo^{3+}_{oct}$ to $ISCo^{3+}_{pyr}$ produces a couple of $LSCo^{4+}_{oct}$ and $HSCo^{2+}_{pyr}$. Conversely e_g electron hopping from $ISCo^{3+}_{pyr}$ to $LSCo^{3+}_{oct}$ ions generates stable $LSCo^{4+}_{pyr}$ but unstable $ISCo^{2+}_{oct}$ (Fig.4.6). This latter process accounts for the decreased ω_{ex} value since the above sketched model to produce Co^{4+}-Co^{2+} pairs would be no more valid. Hence, we can say that the proposed mechanism identifies the SST from $LSCo^{3+}_{oct}$ to $ISCo^{3+}_{oct}$ as a possible origin for the IMT. The temperature induced SST is corroborated by the sudden unit cell volume expansion observed for δ=0.54(1) sample. Indeed the transition to a higher spin-state in Co^{3+} implies bigger ionic radius with respect to $LSCo^{3+}$.[4,5]

Dealing with δ>0.5 samples, the role of the increased amount of $LSCo^{4+}$ induced by increasing δ must be taken into account in the above mechanism. As suggested by Taskin *et al.*,[2,3] the presence of $LSCo^{4+}$ can imply double exchange (DE) interaction between $LSCo^{4+}$, $ISCo^{3+}$ and $LSCo^{3+}$. These exchange channels are active even at room temperature and can be considered to enlighten the gradual improvement in the conductivity that blurs the IMT with increasing δ.[2,3] We argue that the δ dependence of EPR results reported here can be understood considering the interplay between SST and DE. Looking at the ΔH_{pp} temperature dependences, distinct transitions were found

for δ=0.54(1) and δ=0.57(1) samples and we can suggest that the DE contribution is negligible for δ≤0.57 (i.e. Co^{4+}/Co^{3+}≤7.5%). Conversely, the weak effect observed in the temperature dependence of ΔH_{pp} for δ=0.63(1) (i.e. Co^{4+}/Co^{3+}~20%) can be explained considering a strong contribution of DE that accounts for high ω_{ex} value even at room temperature. Moreover we observe a gradual decrease of ΔH_{pp} value increasing δ above 0.54(1) at 305 K. This is a further confirmation that the narrowing of the EPR line with increasing Co^{4+} concentration can be fully explained by DE channel between $LSCo^{4+}$ and $LS/ISCo^{3+}$ active at $T<T_{IM}$.

In order to compare the XRPD and EPR results, in Fig.4.7 (*a*) we plot the normalized change of ΔH_{pp}, $\delta\Delta H_{pp}/\Delta H_{pp}=[\Delta H_{pp}(305)-\Delta H_{pp}(T)]/\Delta H_{pp}(305)$, together with the normalized changes of the lattice constants for δ=0.54(1) sample, $\Delta L/L=[L(305)-L(T)]/L(305)$ where $L=a, b, c$. In the biphasic region we considered an average lattice parameter value calculated as $F_1L_1+F_2L_2$ where L is the lattice parameter and F is relative phase fraction. Indices 1 and 2 stand for low-T and high-T phases, respectively. As shown in Fig. 4.7 (*a*), it is clear that the temperature dependences of $\delta\Delta H_{pp}/\Delta H_{pp}$ and $\Delta a/a$ fairly overlap to each other and the change of ΔH_{pp} is much larger than that of the latter parameter: e.g. at T=400 K $\delta\Delta H_{pp}/\Delta H_{pp}$~15% and $\Delta a/a$~0.5%. In particular, $\Delta a/a$ is the only normalized lattice parameter that increases as a function of T and saturates above T_{IM} in a manner remarkably similar to $\delta\Delta H_{pp}/\Delta H_{pp}$.

This could give evidence that the Co-O-Co interatomic distances along the [100] direction contract with increasing T giving rise to the enhancement of the spin-spin exchange frequency along this direction and the decreasing of ΔH_{pp}. These results suggest spin-lattice interaction along the *a*-axis.

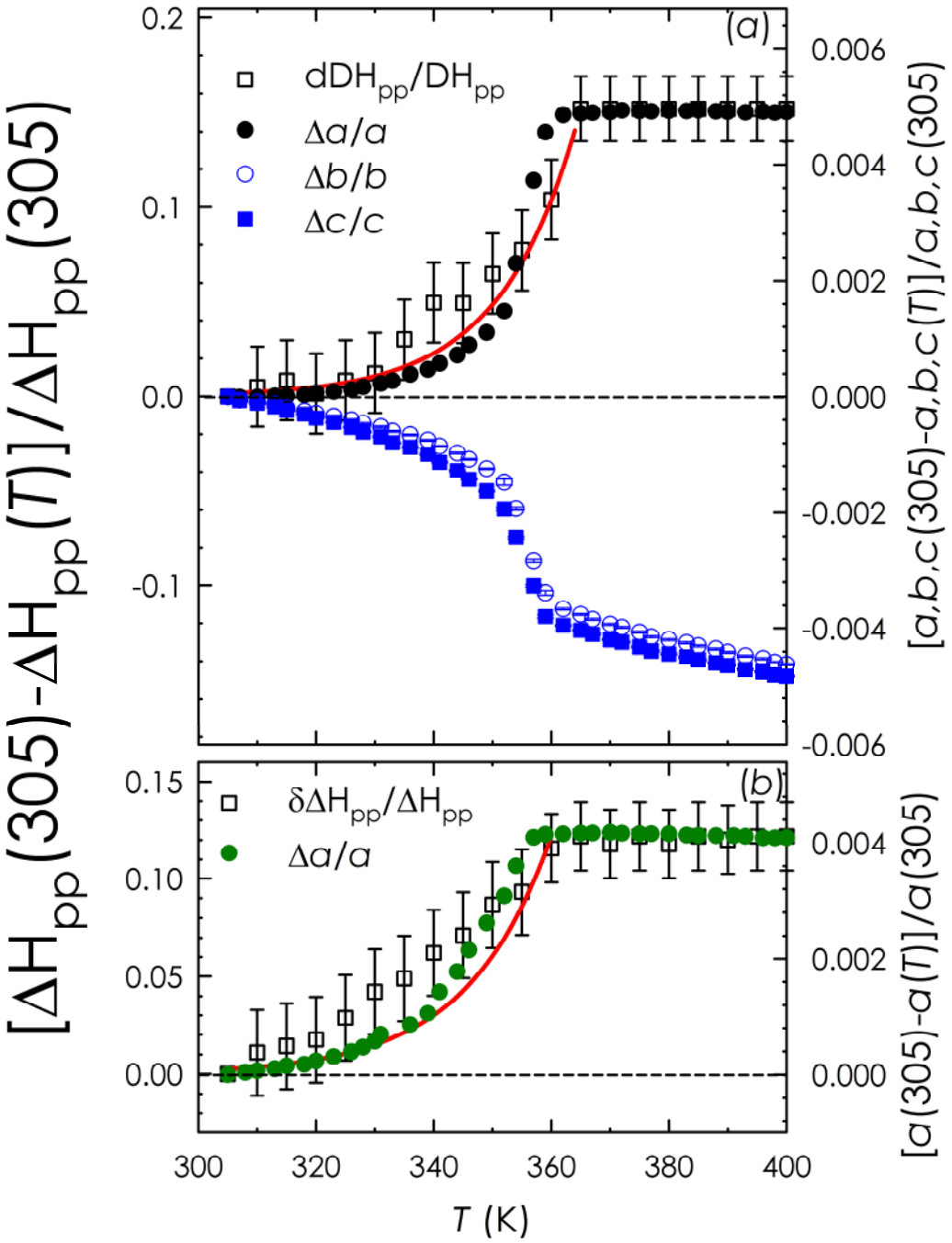

FIG. 4.7 *(a) The normalized ΔH_{pp} (empty squares) values are reported together with the normalized a (full circles), b/2 (empty circles) and c/2 (full squares) axes for δ=0.54(1) sample. (b) The normalized data (a-axis and ΔH_{pp}) are reported for δ=0.57(1). The activation model proposed (full line) is superimposed in panels (a), (b) to experimental data.*

Anisotropic interactions involving Co^{3+} spin and crystal structure are not new in the $GdBaCo_2O_{5+\delta}$ system. In particular, Taskin *et al.*[1] found *Ising*-like behavior of spins along the *a*-axis in the ferromagnetic (FM) phase of $GdBaCo_2O_{5.5}$ single crystal below the Curie temperature T_{Curie} ~275 K.[1,2] According to the proposed model,[1] the insulating FM ground state is generated from the interaction of $ISCo^{3+}$ ions forming 2-leg ladders extended along the *a*-axis.[1,2] These ladders are separated from each other, along the *b* axis, by *ac* CoO_2 layers composed by nonmagnetic $LSCo^{3+}$.[1,2] Above T_{Curie} a clear FM to paramagnetic (PM) transition is observed in the magnetization curve of $\delta \approx 0.5$ sample composition.[1] Basically, two contrasting explanations can be given for such transition: (1) Cobalt spins keep their spin easy axis in the direction of the *a*-axis but the interaction between FM ladders becomes weaker than the PM contribution of Gd^{3+}; (2) The orientation FM order of Co^{3+} *Ising*-like spins is completely destroyed above T_{Curie}.

Ising-Like behavior of spins and the observed $\delta\Delta H_{pp}/\Delta H_{pp}$ and $\Delta a/a$ scaling behavior shows that the *a* axis is the preferred crystallographic direction for distinct phenomena related to the FM and the PM phases. According to Taskin et al.[1,2] in the FM phase the *a*-axis is the preferred direction for magnetization which precludes the formation of magnetic moments along the *b* and *c* axes. Above T_{Curie}, in the PM phase, the *a*-axis is the preferred direction for the spin-lattice interaction which is connected mainly to spin-spin exchange channels. In order to make a link between the two distinct phenomena occurring along the same crystallographic direction, we might suggest that something related to the nature of spins of the FM phase is retained along the *a*-axis even when the phase is PM. This could support the explanation (1) given above and, more importantly, the bridge between FM and PM could be useful to figure out the interplay between the spin-lattice interaction and SST. Indeed, with increasing *T* and by approaching the IMT from the FM phase, the SST from LS to $ISCo^{3+}$ occurs in the

octahedral *ac* layers stacked along the *b*-axis. On the other side, we suggest that the generation of $ISCo^{3+}$ state, holding to lattice deformation, can be significantly influenced by the nature of spins of the FM phase along the *a*-axis. Hence, strong coupling between spin-spin exchange interactions and *a* lattice parameter can be made explaining the observed $\Delta a/a$ and $\delta\Delta H_{pp}/\Delta H_{pp}$ scaling.

In our model the SST is linked with an increasing of spin-spin exchange frequency which is the driving force of IMT. The formation of the metallic phase could be then explained by thermal-activated hopping of spins between neighboring Co sites where the SST from $t_{2g}^5 e_g^0$-LS state to a cobalt high-spin state enhances the number of electrons in the e_g conduction band.[4]

In order to account for such behavior we consider that the change of ΔH_{pp} can be described by the following relation:

$$\frac{\delta\Delta H_{PP}}{\Delta H_{PP}} \approx K \exp\left[-\frac{E(T)}{k_B T}\right] \tag{3.3}$$

where *K* is a constant and *E*(*T*) is a temperature-dependent energy gap.

The energy *E*(*T*) is given by the parameterized power function used to model the temperature dependence of energy splitting between ground and excited spin states of Co in $GdCoO_3$ system.[27] The function is the following:

$$E(T) = E_0\left[1-\left(\frac{T}{T_{IM}}\right)^{3.39}\right] \tag{3.4}$$

Using the optical band gap width E_g=0.26 eV given in Ref.28, we calculated the solid lines shown in Fig.4.7 (*a*), (*b*). The good agreement between model and observed data proves the role of excited Co spin states and, thus, SST in the IMT dynamics of δ=0.54(1) sample. These considerations are still valid for the δ=0.57(1) sample, as shown in Fig.4.7 (*b*). Conversely, just a weak correlation between the $\Delta a/a$ and $\delta\Delta H_{pp}/\Delta H_{pp}$ trends was found for δ=0.63(1) up to ~325 K.

Co^{3+} in IS state is a Jahn-Teller (JT) active ion, so that we expect an increased JT distortion across T_{IM}. Aiming to account for Q_2-type JT distortion, we calculated the differences between *ab*-planar long and short Co-O bond lengths[10] (D_{ab}) obtained by Rietveld refinements against the high quality XRPD data collected at λ=0.35422(1) Å. Figure 4.8 shows the data for δ=0.54(1) as an example whereas the tables containing the refined structural parameters obtained from the Rietveld refinements are reported in Appendix B.

In Fig. 4.9 the D_{ab} values related to octahedra and pyramids are plotted as a function of *T* for all the samples.

In the former case, D_{ab} increases linearly with increasing temperature for δ=0.54(1), indicating that the Q_2-type distortion of the basal plane increases when heating above T_{IM}. Interesting features come out with increasing δ. At *T*~300 K, the D_{ab} values are very similar for δ=0.54(1), δ=0.57(1) and δ=0.63(1). This indicates that rising δ well above 0.5 does not significantly affect the Co-O distances in the octahedra. D_{ab} seems to increase linearly with increasing *T* for δ=0.57(1), approaching a constant value above T_{IM}. Conversely, D_{ab} remains practically unchanged for δ=0.63(1). In the pyramid, the D_{ab} parameters were weakly δ dependent and they did not change

significantly with temperature. This is in agreement with the assumption of *T*-independent $ISCo^{3+}_{pyr}$ states.

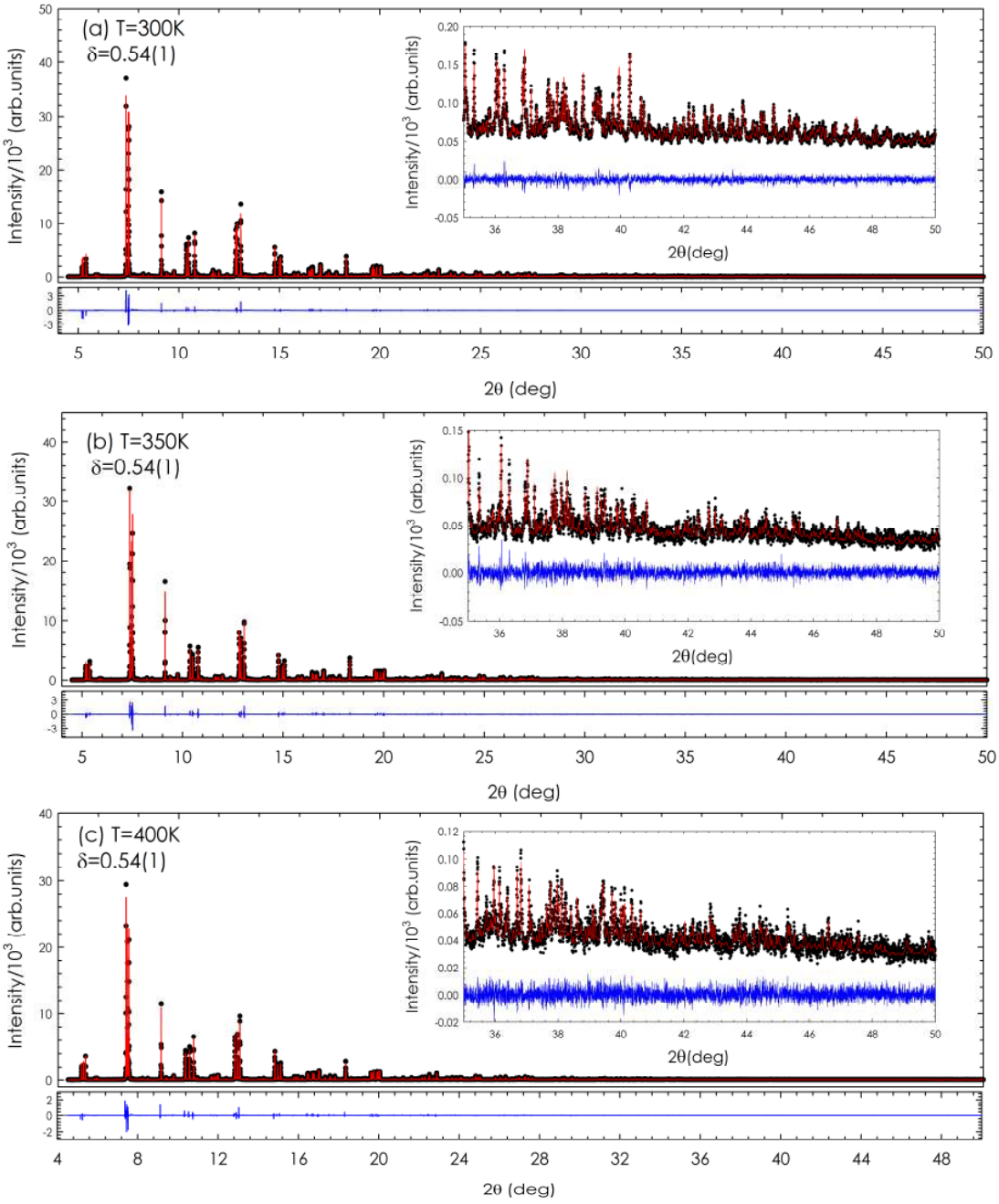

FIG.4.8 *(a),(b),(c) Observed (dots) and calculated (lines) XRPD for* $GdBaCo_2O_{5+\delta}$ *with* δ*=0.54(1) at T=300K, 350K, 400K, respectively. The insets highlight the high angle diffraction peaks. The difference between the observed and fitted patterns is displayed at the bottom of the figure.*

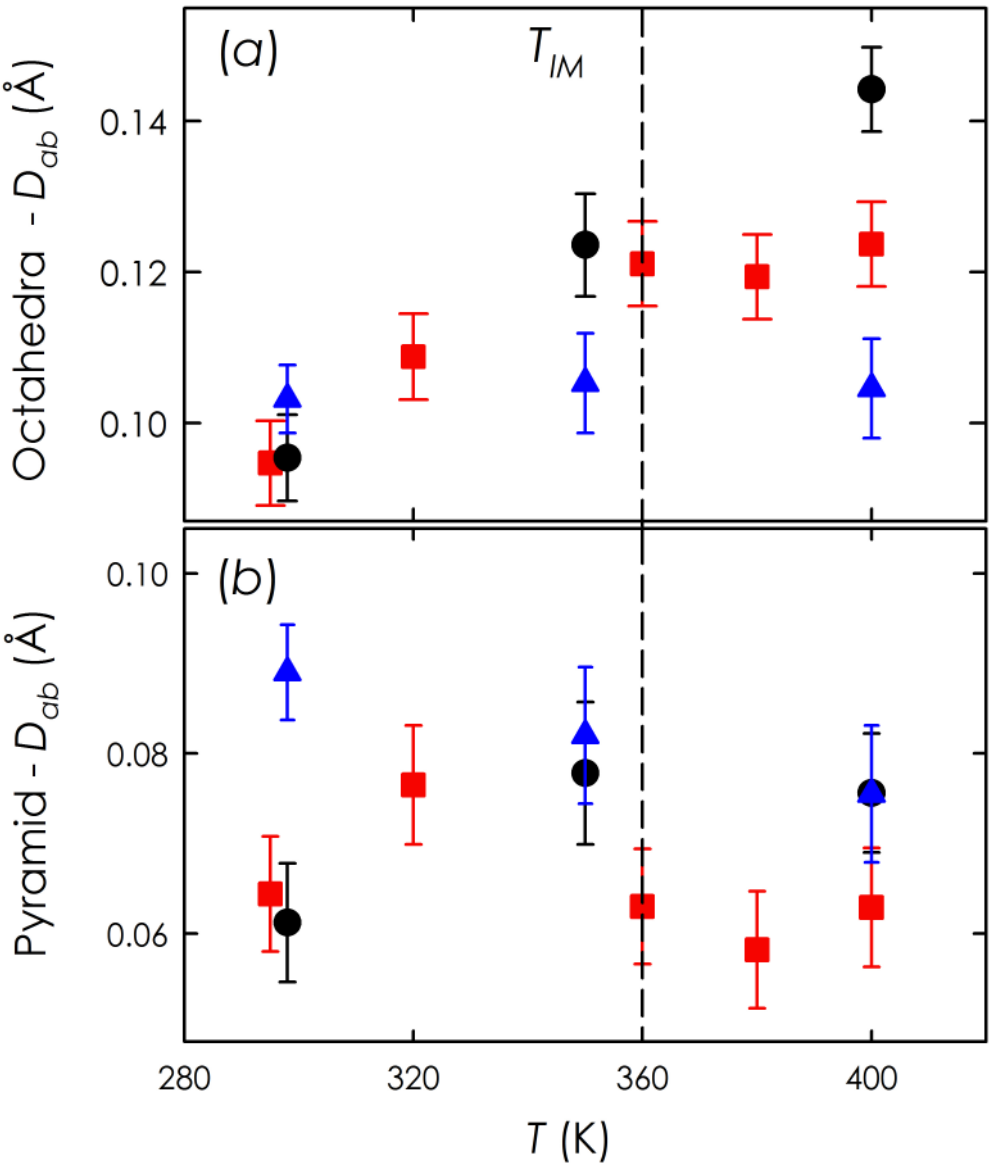

FIG.4.9. *(Color online) (a), (b) The ab planar bond length difference (D_{ab}) values as a function of T for δ =0.54(1) (circles), to δ=0.57(1) (squares) and δ=0.63(1) (triangles) is reported in the octahedral and pyramidal environment, respectively.*

The increasing of D_{ab} distortion observed by the XRPD analysis of the δ=0.54(1) sample corroborates the occurrence of the proposed SST through the gradual population of the JT active IS state. On the other hand we have suggested that the DE

interactions between $LSCo^{4+}$ and $LSCo^{3+}_{oct}$ and $ISCo^{3+}_{pyr}$ [1] strengthens with δ increasing above δ≥0.54(1) giving rise to a blurred IMT.[2] We then expect that the strong DE contribution can also restrain the temperature induced SST by making the $LSCo^{3+}_{oct}$ species less available for the transition. This leaves the high temperature $ISCo^{3+}$ states less populated and destroys the JT effect at Co^{3+}_{oct} sites. Such effects are supported by the absence of a sudden unit cell volume expansion across IMT and the saturation of D_{ab} above T_{IM} for δ=0.57(1) sample as shown in Fig.4.9. In addition, the lack of phase coexistence and the temperature independent behavior of the D_{ab} parameter for δ=0.63(1) further confirms the removal of the JT with increasing δ. These structural effects give evidence to the occurrence of a transition from low-spin to JT active intermediate-spin state and should support the mechanism proposed to explain IMT.

3.6 Conclusion

The increasing of electron hopping probability between Co in different spin states can be indentified as the main driving force for IMT in $GdBaCo_2O_{5+\delta}$ system. EPR data are consistent with this model and the increasing of ω_{ex} with increasing T can be explained by taking into account the SST from $LSCo^{3+}_{oct}$ to $ISCo^{3+}_{oct}$. XRPD and EPR results give evidence about a strong coupling between the SST and the crystal structure. To figure out the nature of this coupling and its connection with IMT two ingredients are needed: (*i*) spin-lattice interaction along the *a*-axis; (*ii*) JT distortion induced by $ISCo^{3+}_{oct}$ which is removed with increasing δ giving rise to a blurred IMT.

Moreover, by comparing our findings with the results reported by Taskin *et al.*,[1] we found that the *a* axis is the preferred crystallographic direction for different phenomena related to the ferromagnetic and to the paramagnetic phases. Indeed, in the

ferromagnetic phase the *a*-axis is the preferred direction for magnetization which precludes magnetic moments formation along the *b* and *c* axes. On the other hand, in the paramagnetic phase the *a*-axis is the preferred direction for the spin-lattice interaction which is linked mainly to spin-spin exchange channels.

References

[1]A. A. Taskin, A. N. Lavrov, and Yoichi Ando, Phys. Rev. Lett. **90**, 227201 (2003).

[2]A. A. Taskin, A. N. Lavrov, and Yoichi Ando, Phys. Rev. B **71**, 134414 (2005).

[3]A. A. Taskin, and Y. Ando, Phys. Rev. Lett. **95**, 176603 (2005).

[4]C. Frontera, J. L. García-Muñoz, A. Llobet, and M. A. G. Aranda, Phys. Rev. B **65**, 180405(R) (2002).

[5]K. R. Zhdanov, M. Yu Kameneva, L. P. Kozeeva, and A.N. Lavrov, Phys. Solid State **52,** 1688 (2010).

[6]Y. Moritomo, T. Akimoto, M. Takeo, A. Machida, E. Nishibori, M. Takata, M. Sakata, K. Ohoyama, and A. Nakamura, Phys. Rev. B **61**, 13325(R) (2000).

[7]V. Pardo, and D. Baldomir, Phys. Rev. B **73**, 165117 (2006).

[8]A. Maignan, V. Caignaert, B. Raveau, D. Khomskii, and G. Sawatzky, Phys. Rev. Lett. **93**, 026401 (2004).

[9]H. Luetkens, M. Stingaciu, Yu. G. Pashkevich, K. Conder, E. Pomjakushina, A. A. Gusev, K. V. Lamonova, P. Lemmens, and H.-H. Klauss, Phys. Rev. Lett. **101**, 017601 (2008).

[10]H. Wu, J. Phys.: Condens. Matter **15**, 503 (2003).

[11]W. R. Flavell, A. G. Thomas, D. Tsoutsou, A. K. Mallick, M. North, E. A. Seddon, C. Cacho, A. E. R. Malins, S. Patel, R. L. Stockbauer, R. L. Kurtz, P. T. Sprunger, S. N. Barilo, S. V. Shiryaev, and G. L. Bychkov, Phys. Rev. B 70, 224427 (2004).

[12]K. Conder, E. Pomjakushina, V. Pomjakushin, M. Stingaciu, S. Struele, and A. Podlesnyak, J. Phys.: Condens. Matter 17, 5813 (2005).

[13]C. Rettori, S. B. Oseroff, D. Rao, P. G. Pagliuso, G. E. Barberis, J. Sarrao, Z. Fisk, and M. Hundley, Phys. Rev. B 55, 1016 (1997).

[14]L. Lo Presti, M. Allieta, M. Scavini, P. Ghigna, L. Loconte, V.Scagnoli, and M. Brunelli, Phys. Rev. B (to be published).

[15] K. Conder, E. Pomjakushina, A. Soldatov, and E. Mitberg, Mater. Res. Bull. **40**, 257 (2005).

[16]A.C. Larson and R.B. Von Dreele, "General Structure Analysis System (GSAS)", Los Alamos National Laboratory Report LAUR 86-748 (2000).

[17]M. Respaud, C. Frontera, J. L.García-Muñoz, M. Á. G. Aranda, B. Raquet, J. M. Broto, H. Rakoto, M. Goiran, A. Llobet, and J. Rodríguez-Carvajal, Phys. Rev. B **64**, 214401 (2001).

[18]E. Pomjakushina, K. Conder, and V. Pomjakushin, Phys. Rev. B **73**, 113105 (2006).

[19]J. Arai, K. Ozawa, and T. Ishiguro, J. Magn. Magn. Mat. **226-230**, 871 (2001).

[20]F. J. Dyson, Phys. Rev. **98**, 349 (1955).

[21]J. P. Joshi and S.V. Bhat, J. Magn. Reson. **168**, 284 (2004).

[22]N. Tristan, V. Zestrea, G. Behr, R. Klingeler, B. Büchner, H. A. Krug von Nidda, A. Loidl, and V. Tsurkan, Phys. Rev. B **77**, 094412 (2008).

[23]P.W. Anderson and P. R. Weiss, Rev. Mod. Phys., **25** 269 (1953).

[24]R. Kubo, and K. Tomita, J. Phys. Soc. Jpn. **9**, 888 (1954).

[25]D. Zakharov et al., in *Quantum magnetism*, edited by B. Barbara, Y. Imry, G. Sawatzky, P. C. E. Stamp (Springer, 2008), p.212.

[26]M. Heinrich, H. –A. Krug von Nidda, R. M. Eremina, A. Loidl, Ch. Helbig, G. Obermeier, and S. Horn, Phys. Rev. Lett. 93, 116402 (2004).

[27]K. Knízek, Z. Jirák, J. Hejtmánek, M. Veverka, M. Marysko, G. Maris, and T.T.M. Palstra, Eur. Phys. J. B. **47**, 213 (2005).

[28]A. A. Makhnev, L. V. Nomerovannaya, S. V. Strel'tsov, V. I. Anisimov, S.N. Barilo, and S. V. Shiryaev, Phys. Solid State **51**, 525 (2009).

4. Structural phase transition in $EuTiO_3$

In this Chapter, we present our synchrotron powder diffraction study on $EuTiO_3$ as a function of temperature.

Up to now the crystallographic structure of the magnetoelectric perovskite $EuTiO_3$ was considered to remain cubic down to low temperature. Here we provide evidence of a structural phase transition, from cubic *Pm*-3*m* to tetragonal *I*4/*mcm*, involving TiO_6 octahedra tilting, in analogy to the case of $SrTiO_3$. The temperature evolution of the tilting angle indicates a second-order phase transition with an estimated T_c=235K. This critical temperature is well below the recent anomaly reported by specific heat measurement at T_A~282K. By performing atomic pair distribution function analysis on diffraction data we provide evidence of a mismatch between the local (short-range) and the average crystallographic structures in this material. Below the estimated T_c, the average model symmetry is fully compatible with the local environment distortion but the former is characterized by a reduced value of the tilting angle compared to the latter. At T=240K data show the presence of local octahedra tilting identical to the low temperature one, while the average crystallographic structure remains cubic. On this basis, we propose intrinsic lattice disorder to be of fundamental importance in the understanding of $EuTiO_3$ properties. These results are available at http://arxiv.org/ as M. Allieta, M. Scavini, L. Spalek, V. Scagnoli, H. C. Walker, C. Panagopoulos, S. Saxena, T. Katsufuji, and C. Mazzoli, arXiv:1111.0541v2 [cond-mat.str-el].

.

4.1 Introduction

Multiferroic materials attract a great deal of interest due to the complex phenomena arising from multiple coupled order parameters existing in a single system.[1] In the case of simultaneous ordering interplay, as in the subset of materials called magnetoelectrics (MEs), the control of ferroelectric polarization via a magnetic field[2] and of magnetic phases by an electric field,[3] has been proved possible.

The interplay of spin and other electronic or lattice degrees of freedom can induce giant magnetoelectric effects,[4-5] dynamic behavior,[6] as well as novel types of excitations,[7] paving the way for future applications in sensors, data storage and spintronics.[8-9] In this paper we present the case of magnetoelectric $EuTiO_3$ (ETO) showing an unusual interplay between dielectric, magnetic and structural degrees of freedom. At room temperature (RT) its crystal structure has been reported to be *Pm-3m* and no phase changes have been observed to occur down to 108 K,[10] as deduced from lab source powder X-ray diffraction. From the dielectric point of view, ETO is described as a quantum paraelectric, as its low temperature dielectric constant increases on cooling and saturates below approximately 30 K.[11] No long range polarization is known to set in, despite high values of susceptibility, typical of a paraelectric state stabilized by quantum fluctuations.[12] The localized 4f moments on the Eu^{2+} sites order at T_N = 5.3 K in a antiferromagnetic arrangement.[13]Concomitant with the onset of antiferromagnetism the dielectric constant decreases abruptly (by $\varepsilon'_{5.5K}/\varepsilon'_{2K}$~3.5%) and shows a strong enhancement as a function of the applied magnetic field (~7% at B~1.5 T), providing evidence for the magnetoelectric coupling.[11] In bulk MEs the coupling between various degrees of freedom is realized at a microscopic level,[3] hence the crystallographic structure of ETO as a function of temperature is vital to any further investigation and modeling.

In this Chapter, we report on the structure of ETO at low temperature, as given by high resolution synchrotron X-ray powder diffraction analysis. Since the diffraction experiments were performed, we have been made aware of a recent publication, reporting about a specific heat anomaly detected in ETO powders at high temperature,[14] and in our discussion we address the differences arising from different experimental probes.

4.2 Sample preparation and powder diffraction experiments

High quality ETO samples have been grown by using the floating-zone method as outlined in Ref.15.

The growth procedure involves melting a pressed rod of mixed starting materials (Eu_2O_3, Ti and TiO_2) under an Ar atmosphere inside a floating-zone furnace. Polycrystalline samples coming from the same batches as the one used for X-ray measurements were checked by specific heat first, showing an anomaly identical to the one recently reported in literature.[14] ETO crystals extracted from the inner part of the grown crystalline rod were powdered, loaded in a 0.70 mm diameter capillary and spun during measurements to improve powder randomization. A wavelength of λ= 0.34986(1) Å was selected by using a double-crystal Si(111) monochromator. Several samples were checked and a few selected on the basis of RT X-ray powder diffraction (XRPD) measurements. The diffracted rays FWHM and symmetry criteria were applied to select a couple of best samples: in the following we report about measurements performed on those specimens. Different data collection strategies were employed: (*i*) in the $0 \leq 2\vartheta \leq 60°$ range data were collected for a total counting time of 2 hours at room temperature (RT), 240K, 230K, 215K, 200K, 175K, 160K, 140K, 120K, 100K, 80K; (*ii*) in the $3 \leq 2\vartheta \leq 15°$ range 30 XRPD patterns were collected while sweeping the

temperature from 300 K to 200 K; (*iii*) at 100 and 240 K data were collected by summing several scans for a total counting time of 7 hours (Q_{max}~27 Å^{-1}.) to achieve the necessary quality for pair distribution function analysis.

The temperature on the sample was varied using a N_2 gas blower (Oxford Cryosystems) mounted coaxially to the sample capillary, being orthogonal to the scattering plane.

Diffractograms were indexed by using the DICVOL91 software.[16] Le Bail-type and Rietveld refinements were performed using the GSAS program.[17] In particular in the Rietveld refinement the background was fitted by Chebyshev polynomials. The absorption correction was performed through the Lobanov empirical formula[18] implemented for the Debye-Scherrer geometry. In the last refinement cycles, scale factor, cell parameters, positional coordinates and isotropic thermal parameters were allowed to vary as well as background and line profile parameters.

4.3 Rietveld analysis of diffraction data

At room temperature ETO is isostructural to $SrTiO_3$ (STO, space group *Pm*-3*m*, *a* = 3.905 Å Ref.20), and the Rietveld refinement of XRPD patterns by the same cubic structural model[10,19] leads to a satisfactory description of our data. Our lattice parameters agree well with the literature (this work: *a* = 3.904782(5)Å; Ref.[19]: *a* = 3.904Å). In Fig. 4.1 (*a*), selected portions of the XRPD patterns collected at various temperatures are shown. The contrast between the unperturbed (111) reflection family and the (200) split one is evident. In particular for this last reflection family, the intensity ratio of the two split peaks is ~1/2, suggesting a cubic to tetragonal structural phase transition.

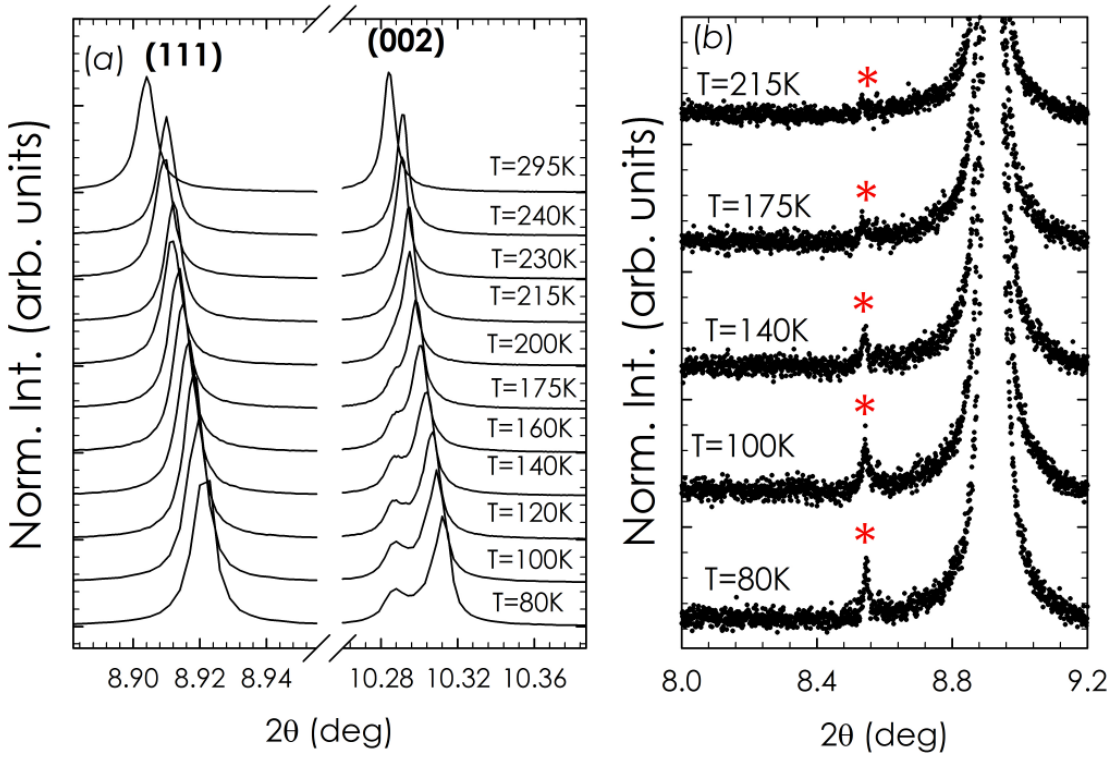

FIG. 4.1 *Selected 2θ regions of ETO X-ray diffraction patterns are shown as a function of temperature. (a) shows the temperature evolution of the Miller index (111) and (002) peaks related to the RT cubic phase. (b) shows the appearance of a weak superlattice reflection as a function of temperature.*

To solve the low temperature structure we have concentrated on data collected at 100K. First of all, 20 strong independent peaks were indexed, resulting in a tetragonal unit cell of lattice parameters *a*, *b* = 3.896 Å, *c* = 3.903Å. Then, by using a Le Bail-type profile-matching without structural model, based on the holohedral space group *P*4/*mmm*, we detected the presence of a few non indexed weak reflections as shown in Fig. 4.1 (*b*). A search for possible supercells gave a unit cell with lattice parameters of *a*, *b* = 5.509Å, c = 7.808Å and the analysis of systematic extinctions for this cell was compatible with a body centered lattice. The two previous tetragonal cells are related according to the

transformation matrix: (1,1,0), (-1,1,0), (0,0,2) or, alternatively, the low temperature tetragonal supercell can be classified as a pseudocubic cell with unit cell metric $\sqrt{2}a\times\sqrt{2}a\times 2a$, where a is the primitive cubic perovskite lattice parameter. By using the Le Bail-type refinement procedure we fitted the diffractograms acquired below room temperature with the new cell metric. In Fig. 4.2, we present the refined lattice parameters as a function of temperature for ETO together with X-ray diffraction data obtained for STO,[21] where a reduced tetragonal cell metric was used for comparison purposes between the cubic and tetragonal phases in the two systems.

Figure 4.2 clearly shows similarities between ETO and STO. The latter exhibits a second order displacive phase transition below T_c=106K,[22] so quite naturally we started from this hypothesis in the analysis of ETO structural phase transition. The possible mechanisms accounting for such modulation of the aristotype perovskite structure (*Pm*-3*m*) can be generated by Jahn-Teller distortion,[23] tilting of corner-linked BO_6 octahedral units,[24-25] polar distortions[25] or higher order mechanisms coupling several of these.[26] Given the electronic state of Ti in ETO ($3d^0$),[27] we concentrated on octahedral tilting and group-theoretical methods have been applied in order to classify compatible structures assuming a second order phase transition. The analysis yielded a list of 15 possible space groups[25] subgroups of the high temperature cubic one.

Restraining the analysis to tetragonal space groups,[25] the possible choices are (between parenthesis the related cell[28]): *I4/mmm* ($2a\times 2a\times 2a$), *P*4/*mbm* ($\sqrt{2}a\times\sqrt{2}a\times 2a$), *I*4/*mcm* ($\sqrt{2}a\times\sqrt{2}a\times 2a$) and $P4_2/nmc$ ($2a\times a\times 2a$). Space groups related to a $2a\times 2a\times 2a$ cell, i.e. *I*4/*mmm* and $P4_2/nmc$, are incompatible with the data on the basis of the metrics (i.e. indexation of the peaks due to the supercell structure). Moreover $P4_2/nmc$ has special extinction conditions, not fulfilled by the experimental pattern. The *P*4/*mbm* space group is completely ruled out by both the metrics and the lattice type. These arguments

leave *I*4/*mcm* as the only possibility. The tetragonal structure in the *I4/mcm* space group is consistent with an out-of-phase tilting of octahedra around the tetragonal axis. The associated irreducible representation (irrep) is R_4^+.[25] The direction of the distortion in the irrep space is indicated by the vector (*a*,0,0).

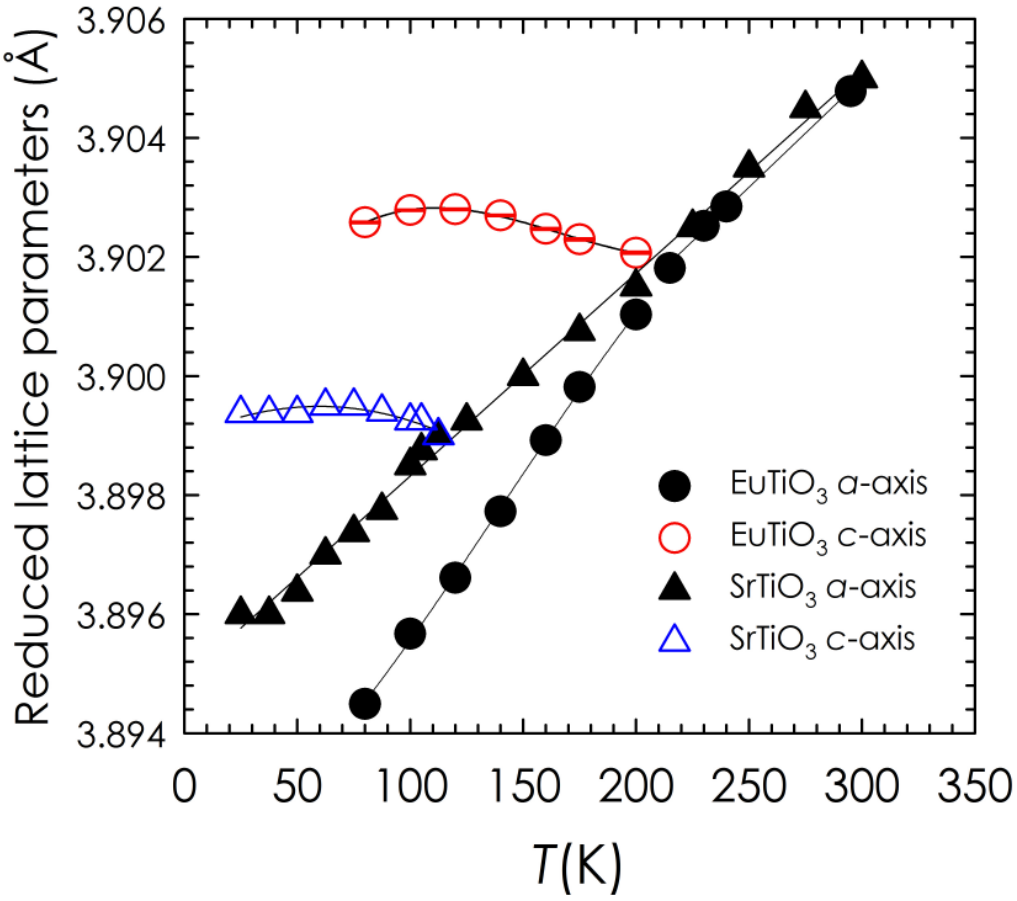

FIG. 4.2 *Reduced lattice parameters of ETO and STO as a function of temperature. The full and opened circles are the a and c-axis of ETO. Full and opened triangles indicate the a and c-axis values of STO derived from Ref. [21]. The continuous lines are guides to the eye.*

In order to obtain the starting atomic positions in *I*4/*mcm* the ISOTROPY [29] package was used, on the basis of the Wyckoff sites occupied in the undistorted cubic structure:

Ti on 1a (0, 0, 0), Eu on 1b (½, ½, ½) and O on 3d (½, 0, 0). The asymmetric unit of the *I*4/*mcm* subgroup consists then of Ti at 4c (0, 0, 0), Eu at 4b (0, ½, ¼), O1 at 4a (0, 0, ¼), O2 at 8h (x, x + ½, 0) with x~¼.

Figure 4.3 shows the Rietveld refinement of data collected at 100K, as obtained by using the above structural model in the *I*4/*mcm* space group.

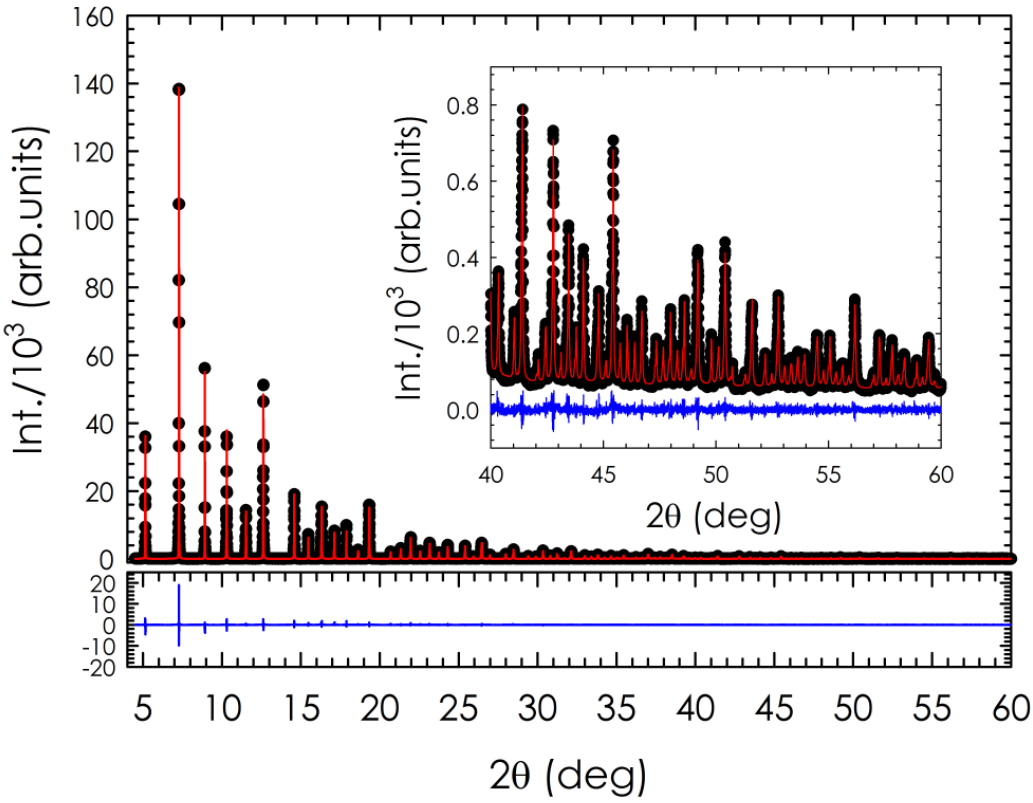

FIG. 4.3 *Measured (dots) and calculated (lines) powder diffraction patterns for ETO at 100K. The inset shows a magnified view of the high angle diffraction peaks. The difference between the observed and fitted patterns is displayed at the bottom of each figure.*

In Table 4.1, structural data and agreement factors obtained for patterns collected at different temperatures are listed. In the tetragonal phase we constrained both isotropic thermal parameters related to oxygen positions O1, O2 to be the same.

Table 4.1 *Refined structural data obtained from synchrotron powder diffraction.*

	RT	240K	230K	215K	200K	175K
a (Å)	3.904782(5)	3.902847(3)	3.902521(2)	3.901813(3)	5.516890(7)	5.515173(8)
c (Å)	----------	----------	----------	----------	7.804140(33)	7.804589(34)
U(Eu)(Å^2)	0.00748(3)	0.00655(2)	0.00623(2)	0.00593(2)	0.00507(2)	0.00471(2)
U(Ti)(Å^2)	0.00454(6)	0.00400(6)	0.00389(6)	0.00373(6)	0.00335(5)	0.00315(5)
U(O)(Å^2)	0.0106(2)	0.0105(2)	0.0101(2)	0.0107(2)	0.0092(2)	0.0090(2)
x[O(2)]	----------	----------	----------	----------	0.2439(7)	0.2410(6)
ϕ (°)	----------	----------	----------	----------	1.41(17)	2.06(14)
Rwp	0.1023	0.1073	0.1069	0.1100	0.0864	0.0945
$R(F^2)$	0.0452	0.0422	0.0400	0.0427	0.0251	0.0268
χ^2	4.494	5.886	5.722	5.117	4.011	3.622

	160K	140K	120K	100K	80K
a (Å)	5.513909(8)	5.512217(6)	5.510639(6)	5.509309(6)	5.507642(9)
c (Å)	7.804941(28)	7.805394(21)	7.805601(6)	7.805572(20)	7.805161(25)
U(Eu)(Å^2)	0.00445(2)	0.00407(2)	0.00366(2)	0.00325(1)	0.00252(2)
U(Ti)(Å^2)	0.00302(5)	0.00284(5)	0.00270(4)	0.00251(4)	0.00220(4)
U(O)(Å^2)	0.0086(2)	0.0084(2)	0.0079(2)	0.0074(2)	0.0073(2)
x[O(2)]	0.2399(5)	0.2384(4)	0.2373(4)	0.2363(4)	0.2353(4)
ϕ (°)	2.30(12)	2.66(10)	2.92(9)	3.14(8)	3.35(9)
Rwp	0.0944	0.0942	0.0934	0.0945	0.0941
$R(F^2)$	0.0273	0.0271	0.0274	0.0268	0.0258
χ^2	3.809	4.010	4.208	4.578	4.847

The thermal variation of the Ti-O and Eu-O bond lengths is given in Fig. 4.4 (*a*), (*b*). In the cubic phase the Ti-O1 distance decreases with decreasing temperature. Below 215K, according to the tilting of TiO6 octahedra, Ti-O distances visibly split as a result of oxygen basal plane O2 displacement. Moreover it should be noted that since in the tetragonal phase the Ti-O1 indicates the distance between Ti and the apical O1 position of octahedron, its thermal variation follows the *c*-axis length evolution on cooling (see Fig. 4.2). The Eu-O1 distance remains approximately constant within the temperature range studied. In the tetragonal phase short (Eu-O2) and long (Eu-O2') distances are generated by the displacement of the O2 position.

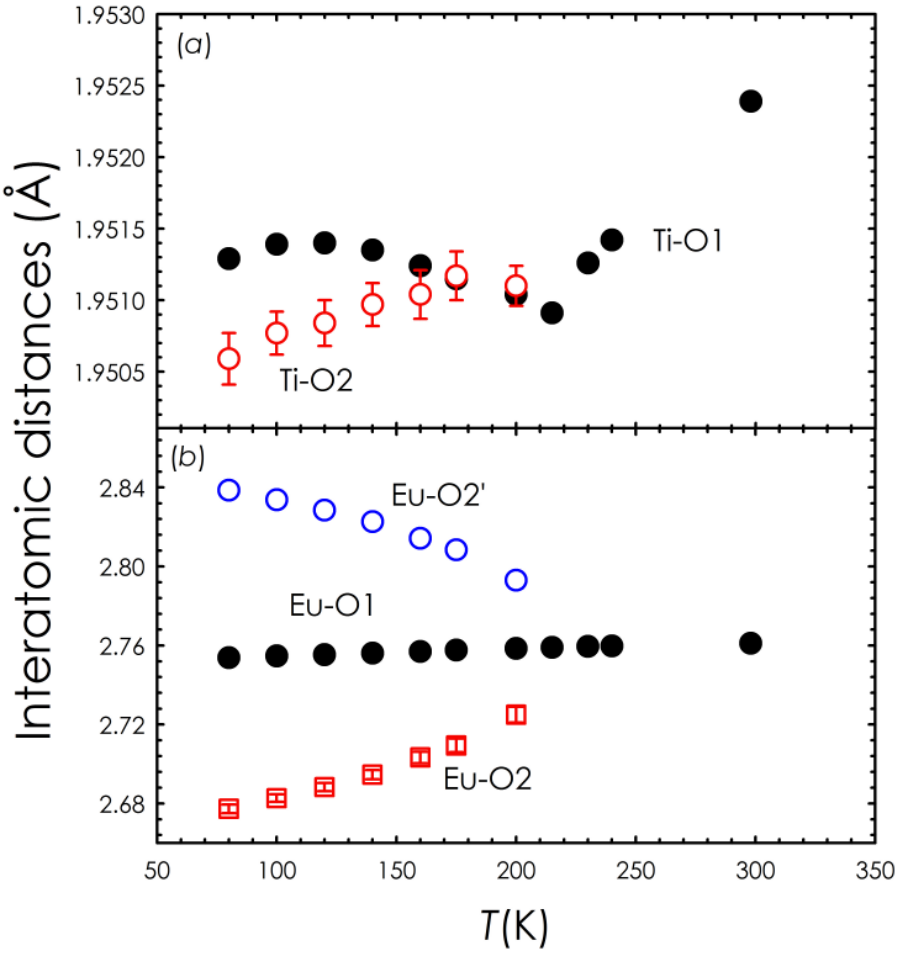

FIG. 4.4 *(a), (b) show the refined Ti-O and Eu-O interatomic distances as a function of temperature.*

In perovskites, the out-phase tilting angle of TiO_6 octahedra (ϕ_-), as calculated from the refined values of the x[O(2)] position, according to $\tan\phi_- = 1-4x$[O(2)],[30] has been proposed as the primary order parameter of the *Pm*-3*m* to *I*4/*mcm* displacive transition of the average structural model. Figure 4.5 shows the values obtained from our refinements as a function of temperature, as listed in Table 4.1. The temperature dependence of ϕ_- is expected to be described by a critical equation of the form: $\phi_-(T) = \phi_-(0)(1 - T/T_c)^{\beta}$, with a critical exponent of $\beta = 0.5$ for a second-order phase transition. The correct determination of T_c is fundamental for an effective estimation of the other model parameters. By setting T_c=215K on the basis of XRPD evidence, we obtained the fit shown in Fig. 4.5 by the solid line, with parameters $\phi_-(0) = 4.03(2)°$ and $\beta = 0.40(1)$. The β value thus obtained is different from the expected value. This finding is particularly important for internal consistency on the adopted procedure, based on our hypothesis of a second order phase transition.

Recently, an anomaly in the temperature dependence of specific heat measured on a powdered ETO sample has been reported, suggesting a structural instability at T_A=282(1) K.[14] Moreover, theoretical calculation performed by the same authors predicts a second-order antiferrodistortive phase transition which agrees perfectly with the *Pm*-3*m* to *I*4/*mcm* transition reported here. Despite this agreement, the discrepancy between the T_c estimated from data in Fig. 4.5 (*a*) and the reported T_A=282(1) K requires further investigation.

For this reason we performed an accurate profile analysis of the (200) reflection indexed within a cubic unit cell (Fig. 4.1 (*a*)) on the 30 XRPD patterns collected between 200 and 300K. In Fig. 4.5(*b*), we report the full width at half maximum (FWHM) of the (200) cubic reflection family as a function of temperature.

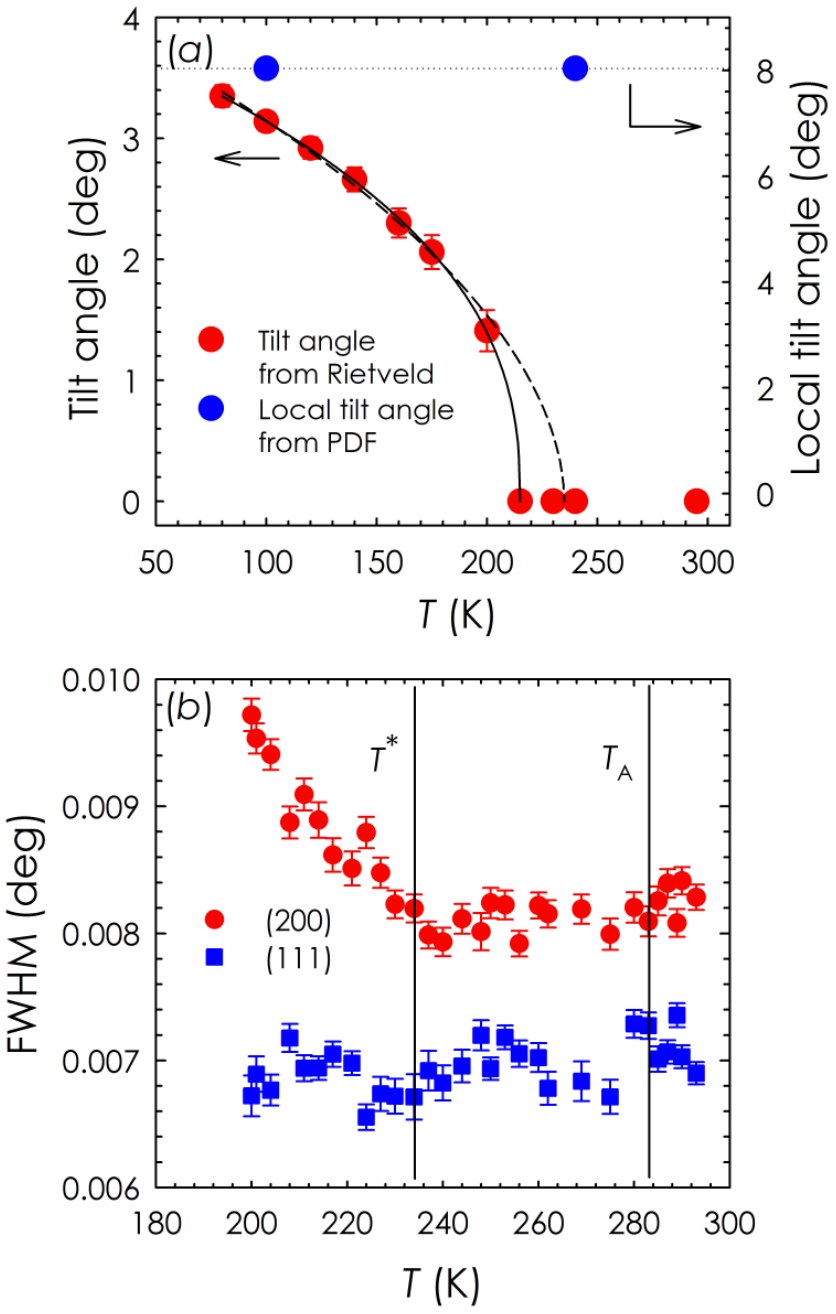

FIG. 4.5 *(a) ETO octahedral tilting angle values (empty circles) deduced from Reitveld analysis as a function of temperature (Table 4.1). The continuous line is the best fit by the critical equation* $\phi\_(T)=\phi\_(0)(1-T/T_c)^{\beta}$ *by setting* $T_c=215K$*. The dotted line is the same but with* $T_c=235K$*. The full circles are the tilting angle values obtained from PDF refinements (Table 4.2). (b) Temperature evolution of the (200) and (111) Bragg families FWHM for the cubic phase of ETO.*

In each pattern a single profile function was used because any attempt to describe the (200) peak by using a multiple peaks resulted in unphysical fluctuations of the fitting parameters. For sake of comparison, the temperature dependence of FWHM related to the (111) cubic reflection family is also shown.

The FWHM of (200) smoothly increases on cooling below T^*~235K (Fig. 4.5 (*b*)). This suggests that the structural distortion inducing the FWHM variation occurs at higher temperature than the temperature estimated by the previous method. However, we point out that from the point of view of XRPD at 235K the structural phase transition is just *incipient* without causing a detectable symmetry breaking until ~200K is reached. Indeed the splitting of cubic (200) peak is not visible in the 200K≤T≤235K range, the difference in the average (see below) *d*-space induced by the tetragonal distortion falling below the instrument resolution. It should be noted that a similar behavior has been already reported by some of the present authors concerning the tetragonal-to-orthorhombic transition of rare-earth cobaltite perovskite.[31] By setting T_c=235K, the fitting of the experimental $\phi_{-}(T)$ data by the same critical equation as before gives $\phi_{-}(0)$ = 4.22(11)° and β = 0.53(7) as parameters best estimate. The resulting curve is shown in Fig. 5 by the dotted line. The value of the critical exponent is now close to the expected value, suggesting that our procedure is reasonably consistent. However T*~235K is still too low to be consistent with the reported T_A from specific heat measurements.[14] Such a discrepancy can arise from an incomplete description of the structural phase transition mechanism or because of intrinsic limits characteristic of the investigation technique. Among functional materials, like ETO,[32] a general consensus is growing on the relation between physical properties of interest and disorder occurring at the local scale.[33] In the case of phase inhomogeneity, for example, the local and the average crystallographic structures are expected to differ, the correlation

length (CL) of the structural distortion being spatially limited. If so, conventional analysis of XRPD data, like Rietveld method, can be inadequate,[34] being able to detect just long enough structural correlations (average structure). On the contrary, total scattering methods, like the pair distribution function (PDF), have been successfully applied to similar problems in Ti-based perovskites.[35-36]

4.4 PDF analysis

We carried out a PDF analysis of the XRPD data collected at T=100K, 240K. The PDF function $G(r)$ is obtained through the total structure factor $S(Q)$ via the sine Fourier Transform (*FT*) using the procedure explained in Chapter 1.

In order to evaluate $I^{coh}(Q)$ consistently, the raw diffracted intensity $I(Q)$ collected at each temperature was corrected for background scattering, attenuation in the sample, multiple and Compton scattering. In particular, at high Q the Compton scattering was removed by calculating the Compton profile with an analytical formula. In the middle-low Q region the Compton scattering correction was applied by multiplying the calculated Compton profile with a monochromator cut-off function.[34] The corrected $I(Q)$ were then properly normalized to get $S(Q)$ and converted to $F(Q)$. The $F(Q)$'s obtained from XRPD data collected at 100K and 240K are shown in Fig.4.6. From the Fourier transform of these data sets we then obtained the PDFs.

The reduction operations have been done using the PDFGetX2 software.[37] Full structure profile refinements were carried out on PDF data using PDFgui program.[38]

Data collected were analyzed starting from r=2.3Å, i.e. excluding the shortest Ti-O distances. Indeed, the total $G(r)$ can be expressed as sum of partial $g_{i\text{-}j}(r)$ weighted for the atomic fractions and $f(Q)$ of the i and j components. Given the contrast between the X ray scattering factors of the element pairs involved, i.e. Eu-Eu, Eu-Ti, Eu-O, Ti-Ti,

Ti-O, the partial $g_{Ti\text{-}O}(r)$ has the lowest weighting. Then, at very low r, the $G(r)$ peak related to Ti-O pair corresponds to very weak feature with respect to the baseline ($-4\pi r\rho_0$), as shown by the arrow in the inset of Fig. 4.7. PDF analysis is sensitive to different crystallographic CL via the refined range of the interatomic distance r.

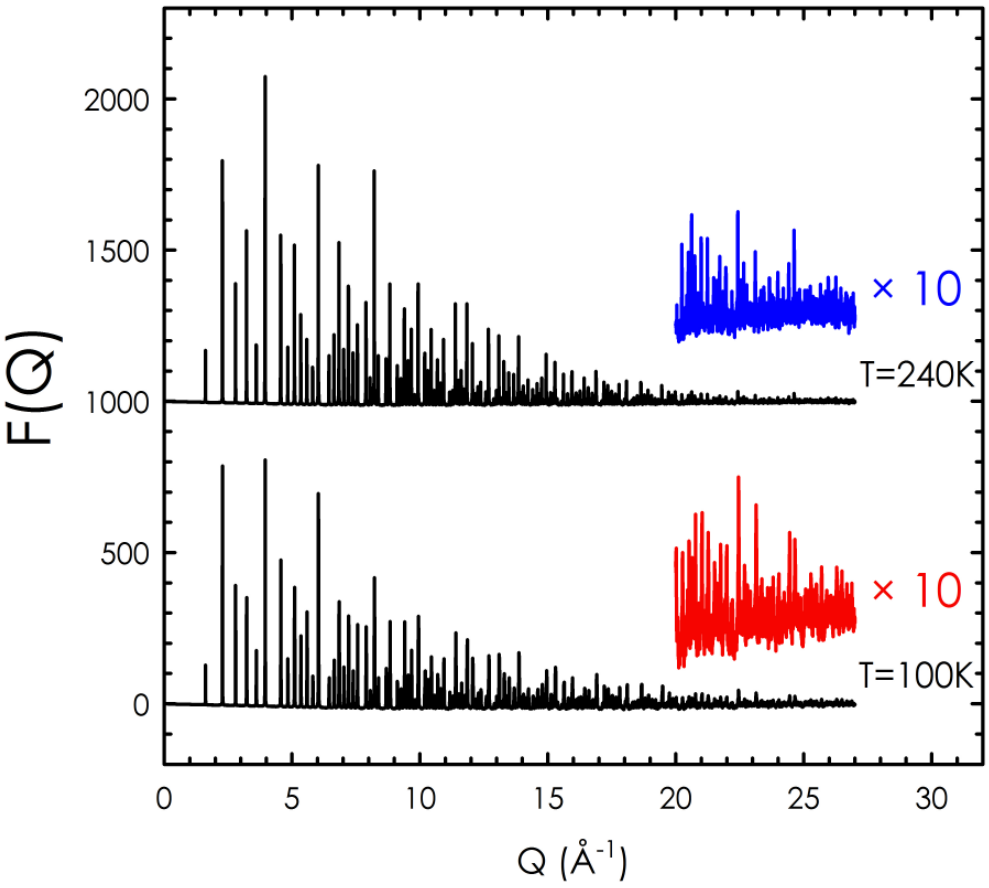

FIG.4.6. *Normalized F(Q) functions obtained from XRPD collected at 100K (bottom) and 240K (up).*

Figure 4.7 shows the full PDF profile structural refinement obtained at 100K by using the average *I*4/*mcm* model in 2.3Å≤r≤20Å range. The agreement factor obtained (Rw=0.073) confirms the good quality of the fit at low enough temperatures when describing local distortions by the average model.

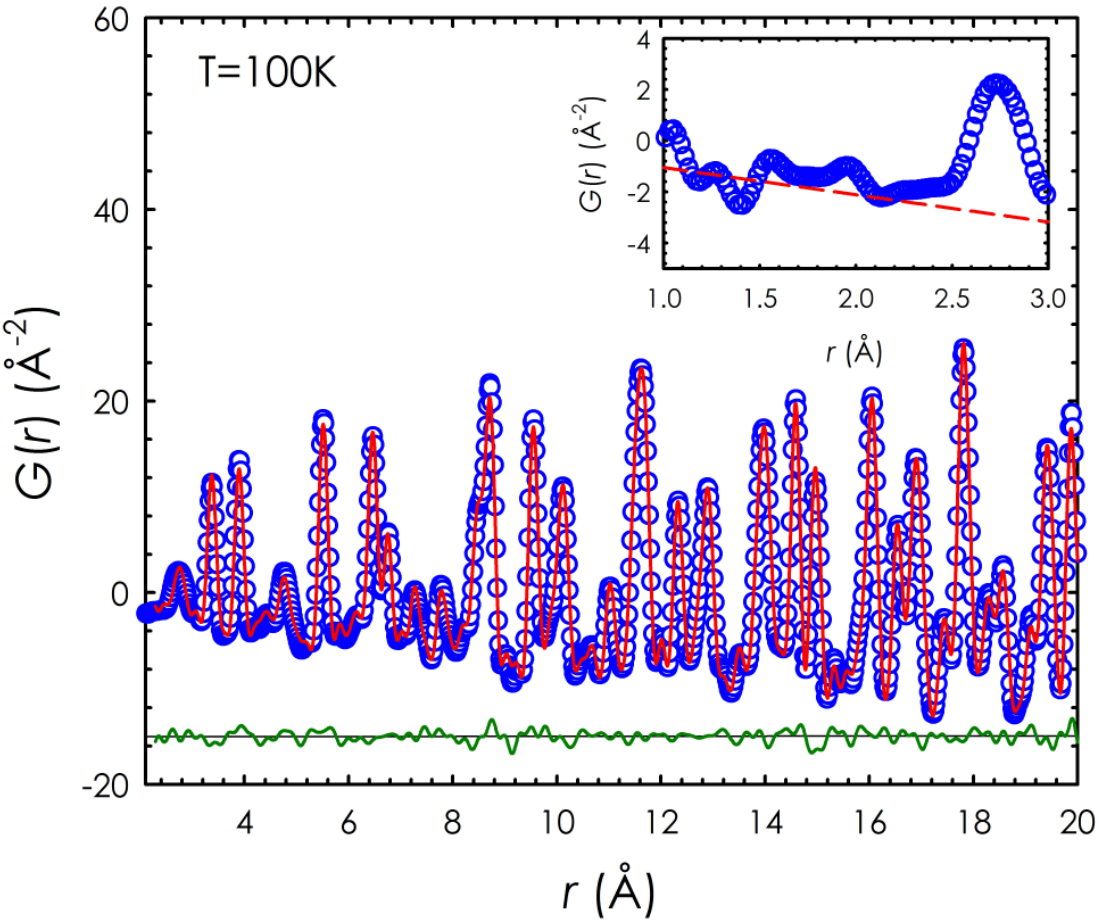

FIG. 4.7 *Observed (dots) and calculated (continuous line) PDF obtained for ETO at 100K. The residual plot is shown at the bottom of the figure. In the inset a region of short interatomic distances is displayed. The dashed line is the baseline and corresponds to* $-4\pi r\rho_0$ *(see Equ.1). The arrow indicates approximately the r position of Ti-O interatomic distances.*

Table 4.2 lists the structural parameter resulting from the PDF refinement at 100 K. By considering the *U*(O1), *U*(O2) unrelated we obtain a marked improvement of the fit quality, so that all the reported PDF refinements were performed without oxygen thermal motion constraints.

Table 4.2 Refined structural parameters of ETO obtained from PDF refinements at 100K and 240K.

Temperature	100K		240K		
Space Group	*I*4/*mcm*		*Pm*-3*m*		*I*4/*mcm*
Fitting *r* range	2.3Å≤*r*≤20Å	20Å≤*r*≤50Å	2.3Å≤*r*≤20Å	20Å≤*r*≤50Å	2.3Å≤*r*≤20Å
a/Å	5.5124(1)	5.5088(2)	3.9019(5)	3.9022(1)	5.5197(8)
c/Å	7.7931(8)	7.8030(5)	----------	----------	7.8002(2)
U(Eu)/Å^2	0.003225(6)	0.003905(2)	0.005463(2)	0.006785(2)	0.005794(2)
U(Ti)/Å^2	0.004317(6)	0.005831(4)	0.006056(5)	0.007231(3)	0.006228(5)
U(O1)/Å^2	0.00341(2)	0.006988(3)	0.02470(5)	0.02594(2)	0.00366(1)
U(O2)/Å^2	0.0429(4)	0.0514(4)	----------	----------	0.0449(2)
x[O(2)]	0.2147(2)	0.2356(6)	----------	----------	0.2147(1)
ϕ (°)	8.05(4)	3.3(1)	----------	----------	8.04(2)
*R*w	0.073	0.074	0.107	0.079	0.074

In the following the proposed structural order parameter ϕ, as obtained by both Rietveld and PDF refinement, is compared as a function of *r*. As reported in Table II, for 2.3Å≤*r*≤20Å (short-range) PDF analysis gives a structural order parameter of ϕ=8.05(4)°, while for 20Å≤*r*≤50Å (long-range) a value of ϕ=3.3(1)° is obtained, showing a strong dependence of the tilting angle as a function of the interatomic distance. In addition, the ϕ value found above 20 Å is in close agreement with value obtained from Rietveld analysis of the XRPD data (ϕ=3.14(8)°).

Figure 4.8 shows short-range portion of the PDF refinement at 240K.

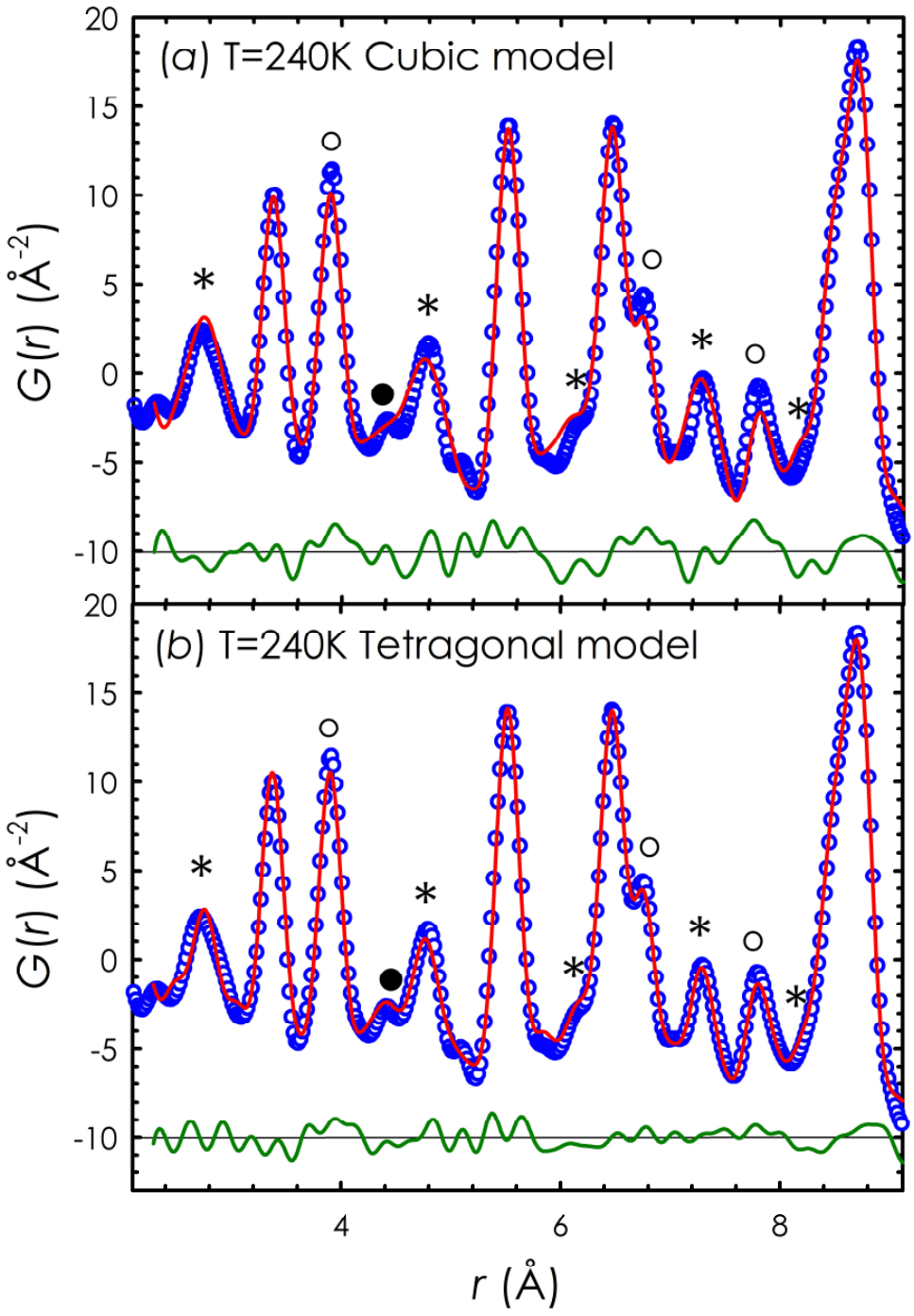

FIG. 4.8 *Short range observed (dots) and calculated (continuous lines) PDF for ETO at 240K. (a) and (b) are the fits obtained using the cubic average model and low temperature tetragonal model, respectively. The symbols in the panel label the PDF peaks belonging to Eu-O (stars), Eu-Eu (empty squares), Ti-O (full circles) interatomic distances.*

In panel *(a)* the average *Pm-3m* cubic model is shown. The calculated PDF systematically underestimates the intensity of most of the experimental peaks, proving the undistorted model to be inadequate. In panel (*b*), the fit performed by using the *I*4/*mcm* model in the same *r* range is shown. The *I*4/*mcm* has a better agreement with the data and the marked features in panel (*a*) are now well described. On the contrary, the *Pm-3m* structural model gives a reasonable fit over the long-range part (Table 4.2) indicating that ETO completely recovers its average structure already at interatomic distances of ~20Å. This provides a clear evidence of a mismatch between the short and the long-range structure at a temperature as high as *T*=240K. Futhermore, by comparing the ϕ_ values obtained from the short range PDF fits, we found that at *T*=100K and 240K the local tilting angles are the same. In order to confirm this finding, in Fig. 4.9(*a*) we compare the PDF collected at 100 K and 240 K up to 80 Å and in Fig.4.9(*b*) we substract one PDF to the other. We note that, according to our fitting models, the difference between G(r)'s changes at ~20 Å indicating that the same short range structure is retained both at low and high temperatures.

4.5 Discussion

PDF analysis of powder diffraction patterns suggests ETO to be an intrinsically disordered system as a clear mismatch between the short- and long-range crystallographic structures is evident at 240K. At 100 K the long-range tetragonal model describes the short-range PDF well qualitatively, but an increased value of the tilting angle is necessary to properly fit the data. From these results we propose a picture to reconcile the apparent discrepancy in the temperature anomalies *T** and T_A as detected by non-local and local techniques, respectively. According to specific heat

measurement interpretation,[14] a second order phase transition occurs in ETO at T_A~282K.

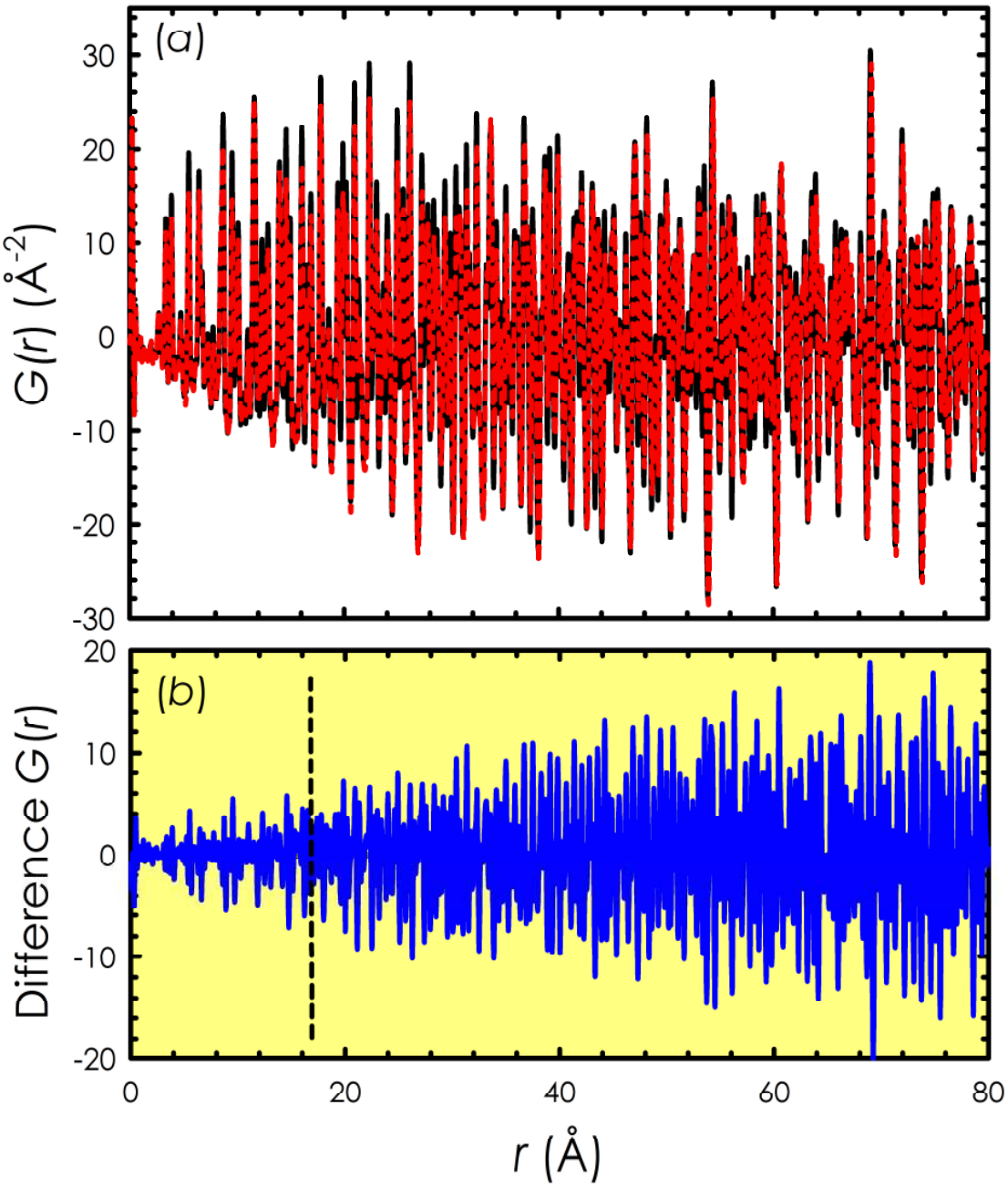

FIG. 4.9 *(a) Comparison of G(r) obtained at 100 K (solid line) and 240 K (dashed line). (b) The difference between the G(r)s is shown. The dashed line marks the variation in the difference plot.*

On the basis of the low temperature structural refinement shown above, we attribute this anomaly to a *Pm-3m* to *I4/mcm* displacive structural transition. The outcome of our PDF analysis shows how the CL of the tetragonal *I*4/*mcm* phase remains confined at the nanoscopic scale (~20Å) for ~235K≤*T*≤282 K. The tilting changes randomly from one nanoregion to the adjacent, quickly averaging out the metric variation on a longer scale, i.e. the crystallite size, and thus reducing the average structure to a cubic space group. For this reason the local distortion cannot be detected by conventional techniques as the Rietveld analysis of XRPD data. By decreasing *T*, a divergence of the tetragonal tilting CL takes place, resulting in a disorder-order transition at *T**~235K. Close to *T**, the magnitude of the tetragonal distortion (tilted) corresponding to the long-range ordered phase is still small, so that the transition shows up just as a weak feature in the temperature dependence of the cubic (200) FWHM. By further cooling the tetragonal deviation from the cubic metric increases, until the experimental resolution is finally sufficient to resolve it below 215 K. There, splitting of the Bragg peaks as well as the appearance of superlattice reflections are clearly observed in Rietveld refinements. It is worth noticing that even at *T*=100 K, i.e. well below *T**, the local tilting angle is greater than the one obtained from the long-range PDF refinement. At *T*=100K and 240K the local tilting angles (short-range refinement) are the same (~8°), see Fig. 4.5 and Table 4.2, whereas the tilting angle obtained at *T*=100 K from the long-range PDF refinement agrees well with the result of the Rietveld refinement for the average structure (~3°). On the other hand, *Cp* measurements do not show a sharp feature but a quite broad one over the temperature range shown in Ref.14, leaving the possibility of a further evolution of the structural distortion CL possible. In principle, the space group *I*4*cm* obtained from the coupling of R^+_4 and the Γ^+_4 polar irreducible representation[25] could be compatible with our experimental results on the

basis of metrics and extinction conditions. In particular, by considering [001] as the polar direction and the Eu position (i.e. the Γ^{+}_{4} polar irreducible representation) as a reference , we refined the data using the *I4cm* model. By comparing the results from *I4/mcm* and *I4cm* models we found no improvement in the refinement statistics at any temperature. However, it is worth noticing that the discrimination between 4/mmm and 4mm point symmetries requires a careful examination of the intensity distribution statistics, a very difficult task to be performed on powder diffraction data due to peak overlapping. Hence, the occurrence of inversion symmetry breaking cannot be unequivocally excluded by the current analysis of our high resolution XRPD data.

On the other hand, in the case of inversion symmetry breaking a strong dynamical behavior of the dielectric constant would be expected. In addition, given the mismatch between the local- and the long-range orders found in ETO, the system could act as relaxor ferroelectrics.[39] In these latter systems the disorder is typically introduced extrinsically, through chemical doping, while in ETO the structure itself seems to be willing to organize at a nanoscopic scale (forming domains of the order of ~20 Å).

4.6 Conclusion

In conclusion, in this paper we show that ETO undergoes a cubic to tetragonal structural phase transition below room temperature, on the basis of XRPD data analysis. The *I*4/*mcm* space group generated by an out-of-phase tilting of TiO_6 octahedra gives the best description of our powder diffraction data at low temperatures. Literature specific heat measurement shows an anomaly at T_A=282(1) K. Our PDF analysis of XRPD data shows that at T=240 K the structure of ETO is already distorted and consistent with the presence of local tilting regions embedded in a long-range cubic phase. From Rietveld analysis of XRPD data the temperature dependence of the

average tilting angle and of the (200) cubic peak FWHM suggests a second order transition taking place at T^*~235K. From the comparison between the Rietveld and the PDF analysis of XRPD data, we propose that the difference between T^* and T_A is due to the CL scale evolution of the structural phase transition. At T_A the cubic to tetragonal phase transition occurs at the nanoscale and it is then followed by a disorder-order transition at T^*, where the CL of the distorted regions starts to diverge, at least form the point of view of a non-local technique. Moreover, at T=100 K the average model is consistent with the outcome of the long-range PDF refinement, while the short-range one suggests that a bigger value of the tilting angle is locally realized. This provides evidence of disorder at the nanometric scale even below T^*, suggesting ETO to be an intrinsically disordered system in which the structural phase CL changes dramatically over a wide range of temperatures. In case of a possible further symmetry breaking of the *I4/mcm* space group by inversion symmetry loss, fact that cannot be excluded by the present investigation, this material would represent the first evidence of an intrinsic relaxor magnetoelectric: disorder modulated interactions are expected to deeply influence the low temperature electric properties. We believe that this fact has to be taken in suitable consideration when describing the peculiar properties of ETO as a quantum paraelectric material.

References

[1] W. Eerenstein, N. D. Mathur, and J. F. Scott, Nature **442**, 759 (2006).

[2] T. Kimura, T. Goto, H. Shintani, K. Ishizaka, T. Arima, and Y. Tokura, Nature **426**, 55 (2005).

[3] T. Lottermoser, T. Lonkai, U. Amann, D. Hohlwein, J. Ihringer, and M. Fiebig, Nature **430**,
541 (2004).
[4] J. Wang, H. Zheng, V. Nagarajan, and et al., Science **299**, 1719 (2003).
[5] A. Zvezdin and A. Pyatakov, Usp. Fiz. Nauk **174**, 465 (2004).
[6] J. Hemberger, P. Lunkenheimer, R. Fichtl, H.-A. K. von Nidda, V. Tsurkan, and A. Loidl, Nature **434**, 364 (2005).
[7] A. Pimenov, A. A. Mukhin, V. Y. Ivanov, V. D. Travkin, A. M. Balbashov, and A. Loid, Nature Physics **2**, 97 (2006).
[8] J. Scott, Nature **6**, 256 (2007).
[9] A. Zvezdin, A. Logginov, G. Meshkov, and A. Pyatakov, Bull. Rus. Acad. Sci. **71**, 1561 (2007).
[10] J. Brous, I. Fankuchen, and E. Banks, Acta Cryst. **6**, 67 (1953).
[11] T. Katsufuji and H. Takagi, Phys. Rev. B. **64**, 054415 (2001).
[12] K. A. Muller and C. T. Burkhard, Phys. Rev. B **19**, 3593 (1979).
[13] T. R. McGuire, M. W. Shafer, R. J. Joenk, H. A. Alperin, and S. J. Pickart, J. Appl. Phys. **37**, 981 (1966).
[14] A. Bussmann-Holder, J. Köhler, R. K. Kremer, and J. M. Law, Phys. Rev. B. **83**, 212102 (2011).
[15] T. Katsufuji and Y. Tokura, Phys. Rev. B **22**, R15021 (1999).
[16] A. Boultif and D. Louer, J. Appl. Cryst. **24**, 987 (1991).
[17] A. Larson and R. Von Dreele, General Structural Analysis System (GSAS)," Los Alamos National Laboratory Report LAUR, 2004, 86-748.
[18] Lobanov, N.N. Alte da Veiga, L. *6th European Powder Diffraction Conference Abstract* P12-16, 1998.
[19] D. L. Janes, R. E. Bodnar, and A. L. Taylor, J. Appl. Phys. **49**, 1452 (1978).
[20] F. W. Lytle, J. Appl. Phys. **35**, 2212 (1964).
[21] A. Okazaki and M. Kawaminami, Mater. Res. Bull. **8**, 545 (1973).
[22] H. Unoki and T. Sakudo, J. Phys. Soc. Jpn. **23**, 546 (1967).
[23] M. A. Carpenter and C. J. Howard, Acta Cryst B **65**, 134 (2009).
[24] C. J. Howard and H. T. Stokes, Acta Cryst B **54**, 782 (1998).
[25] C. J. Howard and H. T. Stokes, Acta Cryst A **61**, 93 (2005).

[26] H. T. Stokes, E. H. Kisi, D. M. Hatch, and C. J. Howard, Acta Cryst. B **58**, 934 (2002).

[27] C-L. Chien, S. De Benedetti, F. De S. Barros, Phys. Rev. B. **10**, 3913 (1974).

[28] The unit cell metrics are expressed as multiplied periodicity of the *Pm*-3*m* parent (*a*×*a*×*a*).

[29] H. T. Stokes, D. M. Hatch, and B. J. Campbell, ISOTROPY (2007), http://stokes.byu.edu/isotropy.html.

[30] K. Tsuda and M. Tanaka, Acta Cryst A **51**, 7 (1995).

[31] L. Lo Presti, M. Allieta, M. Scavini, P. Ghigna, L. Loconte, V. Scagnoli, M Brunelli, Phys. Rev. B **84**, 104107 (2011).

[32] J. H. Lee et al. Nature **466**, 954 (2010).

[33] E. Dagotto, Science **309**, 257 (2005).

[34] T. Egami, S. J. L. Billinge, *Underneath the Bragg peaks: Structural Analysis of Complex Materials* (Pergamon Materials Series, 2003), Vol. 7.

[35] K. Page, T. Kolodiazhnyi, T. Proffen, A. K. Cheetham, R. Seshadri, Phys. Rev. Lett. **101**, 205502 (2008).

[36] Jin-Cheng Zheng, A. I. Frenkel, L. Wu,1 J. Hanson, W. Ku, E. S. Božin, S. J. L. Billinge, Yimei Zhu, Phys. Rev. B **81**, 144203 (2010).

[37] X. Qiu, J. W. Thompson, S.J.L. Billinge, J. Appl. Cryst., **37**, 678 (2004).

[38] C. L. Farrow, P. Juhás, J.W. Liu, D. Bryndin, E.S. Božin, J. Bloch, Th. Proffen, S. J. L. Billinge, J. Phys. : Condensed Matter **19**, 335219 (2007).

[39] I.-K. Jeong, T.W. Darling, J. K. Lee, Th. Proffen, R. H. Heffner, J. S. Park, K. S. Hong, W. Dmowski, T. Egami, Phys. Rev. Lett. **94**, 147602 (2005).

5. Differential pair distribution function

As described in Chapter 1, the Pair Distribution Function technique based upon X-ray diffraction data is a powerful tool to unveil disorder on the nanometric scale. However, unlike Extended X-ray absorption fine structure (EXAFS) technique, PDF is element insensitive. In order to overcome this problem, the anomalous dispersion of X-rays near the absorption edge of a certain element can be exploited to obtain the so called Differential Pair Distribution Functions (DPDF).

In this Chapter, we derived the basic equations of DPDF method by applying the formalism of anomalous X-ray diffraction to total scattering. In order to test the validity of this approach to extract chemical specific information we applied this technique to the case of gadolinium doped ceria electrolytes.. Diffraction data have been collected at the Ce-*K* and Gd-*K* edge on the ID31 beamline of the European Synchrotron Radiation Facility (ESRF). The results related to $Ce_{0.75}Gd_{0.25}O_{1.875}$ sample measured near the Ce *K*-absorption edge have been published on reference: M. Allieta, M. Brunelli, M. Coduri, M. Scavini, C. Ferrero*, Z. Kristallogr. Proc.* **1**, 15 (2011).

5.1 Introduction

$Ce_{1-x}Gd_xO_{2-x/2}$ (CGO) compounds have been intensively studied in the last years as conducting electrolytes for electrochemical cells.[1] The ionic conductivity in CGO is due to oxygen diffusion via the vacancy mechanism. Actually, half oxygen vacancy is introduced into the structure when a Ce^{4+} ion is substituted by a Gd^{3+} one. At increasing Gd^{3+} concentration x, the conductivity $\sigma_i(x)$ reaches a maximum (at fixed T) and then decreases for higher x values.[2] This behavior has been attributed to the formation of defect clusters.

Accordingly, EXAFS measurements have detected the presence of Gd^{3+}-V_O-Gd^{3+} defect clusters in CGO materials.[3] However, the EXAFS technique can be successfully employed to explore *only* the local structure of Ce^{4+} and Gd^{3+} ions, and cannot provide further information in case of more extended defects (e.g. on the nanometric scale).

Conversely, the Pair Distribution Function (PDF) $G(r)$, i.e. the real space analysis of diffraction data, is a unique tool to determine the local and medium range deviations with respect to an ideally periodic structure within the same X-ray powder diffraction (XRPD) experiment. However, unlike EXAFS, this technique is not element sensitive, therefore it can be difficult to discriminate the contributions of Ce^{4+} and Gd^{3+} ions since their ionic radii are similar.

This problem can be overcome by applying the anomalous X-ray diffraction (AXD) technique[4] to a total scattering method in order to obtain the so-called Differential Pair Distribution Function (DPDF).[5]

5.2 Experimental

A micro-crystalline CGO sample with Gd concentration x =0.25 and 0.50 was prepared with the *Pechini* sol-gel method and fired at 900°C for 72 hours. XRPD patterns were collected at the ID31 beamline of the ESRF in the diffraction range $0<2\theta<80°$ covering a range of the wave-vector Q ($=4\pi \sin\theta/\lambda$) up to Q_{max}~30 $Å^{-1}$. We collected experimental data (plus empty capillary and air background) from $Ce_{0.75}Gd_{0.25}O_{1.875}$ and $Ce_{0.50}Gd_{0.50}O_{1.75}$ samples at four incident X-ray wavelengths named λ_1=0.30975(1) Å , λ_2=0.30760(1) Å, λ_3 = 0.24960(1) Å and λ_4 = 0.24748(1) Å near the Ce (λ_1, λ_2) and Gd (λ_3, λ_4) K-absorption edge, respectively. Additional data at λ_1 were collected also on CeO_2 (Aldrich ≥99.0%) and Gd_2O_3 (Aldrich 99.9%). In order to attain XRPD data quality for experimental $G(r)$, all patterns were obtained summing several scans (~7

hours total measuring time) performed at fixed temperature (T=90K). Data were corrected using the PDFGetX2 software.[6] In order to avoid an excessive noise-to-signal ratio at high Q range in the DPDF we have considered only data up to Q_{max}=24 Å^{-1} for all the samples. An X-ray fluorescence measurement was carried out on CeO_2 in the 39.93<E<40.62 keV and 49.56<E<50.44 keV energy range across the Ce and Gd K-edges.

5.3 Differential pair distribution function: the method

The total PDF, $G(r)$, is the atomic number density-density correlation function which describes atomic arrangements in powders or isotropically scattering amorphous materials.[5] The $G(r)$ function is obtained through the total structure factor S(Q) via the sine Fourier Transform (FT):[5]

$$G(r) = 4\pi r[\rho(r) - \rho_0] = \frac{2}{\pi}\int_{Q=0}^{Q_{max}} Q[S(Q) - 1]\sin(Qr)\mathrm{d}Q \qquad (5.1)$$

where, $\rho(r)$ and ρ_0 are the local and average atomic number densities and r is the interatomic distance. The upper integration limit Q_{max} is the reciprocal space cut-off.

For a single diffraction experiment on a sample composed of n chemical species, the total structure factor can be expressed as a weighted average of $n(n+1)/2$ partial structure factors,[5] i.e.:

$$S(Q) - 1 = \sum_{i,j}^{n} \frac{c_i c_j f_i(Q,\lambda) f_j(Q,\lambda)}{< f(Q,\lambda) >^2}[S_{ij}(Q) - 1] \qquad (5.2)$$

where c_i is the atomic fraction of the j component and $f_i(Q,\lambda)$ is the atomic scattering factor of the *i* component. The double sum runs over all atoms of the sample's stoichiometric unit and the brackets < > mean the average over the compound unit. $S_{ij}(Q)$ is the partial structure factor of the (i,j) atoms pair.

The total structure factor is calculated from the experimental coherent X-ray scattering intensity $I^{coh}(Q,\lambda)$ by:

$$S(Q) - 1 = \frac{I^{coh.}(Q,\lambda) - < f^2(Q,\lambda) >}{< f(Q,\lambda) >^2} \tag{5.3}$$

Combining equations (5.2) and (5.3) yields:

$$I^{coh.}(Q,\lambda) - < f^2(Q,\lambda) > = \sum_{i,j}^{n} c_i c_j f_i(Q,\lambda) f_j(Q,\lambda)[S_{ij}(Q) - 1] \tag{5.4}$$

From equation (5.4), it can be seen that all $S_{ij}(Q)$ can be determined from $n(n-1)/2$ independent intensity measurements according to which the atomic fractions in this equation are varied. A way to produce a significant change in the factors $f_i(Q,\lambda)$ is to exploit the anomalous dispersion effect of the X-rays near the absorption edge of an element.[7] Complete experimental and theoretical details of the anomalous X-ray scattering technique are reported elsewhere[4] and in the following we briefly present the application of this technique to obtain chemical specific $G(r)$ functions.

The atomic scattering factor of a specific atom is given by:

$$f(Q,E) = f_0(Q) + f'(E) + if''(E) \tag{5.5}$$

where the $f_0(Q)$ is the scattering factor and $f'(E)$ and $f''(E)$ are the real and imaginary part of the anomalous dispersion term, respectively.

The trends of $f'(E)$ and $f''(E)$ versus E in the close vicinity of an absorption edge (Ce *K*-edge) are shown in Fig. 5.1 (*a*), (*b*). The $f''(E)$ term is directly related to the photoelectric absorption and is almost flat below the edge and rises dramatically at the edge. $f'(E)$ exhibits a sharp negative peak with a full width at half maximum of ~100eV.

According to equation (5.4), if two diffraction intensity measurements are performed at slightly different wavelengths λ_1, λ_2 near the absorption edge of a particular element A, a large change of the real part of $f_A(Q,\lambda)$ and consequently of the coherent Intensity $I^{coh}(Q,\lambda)$ occurs. The differential structure factor ($DSF(Q)$) is defined as:[8]

$$DSF(Q) \equiv \frac{[I^{\text{coh.}}(Q,\lambda_1) - < f^2(Q,\lambda_1) >] - [I^{\text{coh.}}(Q,\lambda_2) - < f^2(Q,\lambda_2) >]}{c_A[f'(\lambda_1) - f'(\lambda_2)]\mathrm{W}(Q,\lambda_1,\lambda_2)} = \sum_j^n \frac{\mathrm{W_{Aj}}(Q,\lambda_1,\lambda_2)}{\mathrm{W}(Q,\lambda_1,\lambda_2)}[S(Q)_{\mathrm{Aj}} - 1] \tag{5.5}$$

where the total $\mathrm{W}(Q,\lambda_1,\lambda_2)$ and partial $\mathrm{W_{Aj}}(Q,\lambda_1,\lambda_2)$ weighting factors are defined as follows:

$$\mathrm{W}(Q,\lambda_1,\lambda_2) = \sum_k^n c_k \Re[f_k(Q,\lambda_1) + f_k(Q,\lambda_2)] \tag{5.6}$$

$$\mathrm{W_{Aj}}(Q,\lambda_1,\lambda_2) = c_j \Re[f_j(Q,\lambda_1) + f_j(Q,\lambda_2)] \tag{5.7}$$

where $\Re$ stands for real part. According to equation (5.1), the DPDF is calculated from the FT of the $DSF(Q)$ function. The DPDF will then contain only contributions of atomic pairs involving the anomalously scattering atom.

5.4 Application to $Ce_{1-x}Gd_xO_{2-x/2}$

The procedure shown above was applied to the case of a $Ce_{0.75}Gd_{0.25}O_{1.875}$ and $Ce_{0.5}Gd_{0.5}O_{1.75}$ sample at both the Ce and Gd *K*-edges.

In order to obtain experimental $f'(E)$ and $f''(E)$ values, the fluorescence spectrum of CeO_2 and Gd_2O_3 were measured and then converted to $f''(E)$ data and $f'(E)$ using the Kramers-Kronig (KK) relation[7] (Fig. 5.1).

Referring to pre-edge region ($E_1<E<E_2$ and $E_3<E<E_4$ in Fig. 5.1), the experimental values can be affected by instrumental aberration (e.g. large background) and the core hole lifetime broadening problem characterizing the *K*-edge of element with large atomic number Z. As these features cause the $f''(E)$ values to be unreliable near the Ce and Gd *K*-edges, in the present investigation the theoretical values for Ce and Gd were used.[9] However, it should be noted that for finely tuning the wavelengths involved in the present experiment, the determination of the fluorescence spectra is rather important to detect any monochromator offset.

In order to evaluate consistently $I^{coh.}(Q,\lambda)$ at each wavelength, the raw $I(Q,\lambda)$ were corrected for background scattering, attenuation in the sample, multiple and Compton scattering. In particular, at high Q the Compton scattering was removed by calculating the Compton profile with an analytical formula.[5] In the middle-low Q region the Compton scattering correction was applied by multiplying the calculated Compton

profile with a monochromator cut-off function.[5] Then the corrected $I(Q, \lambda)$ were normalized.[5]

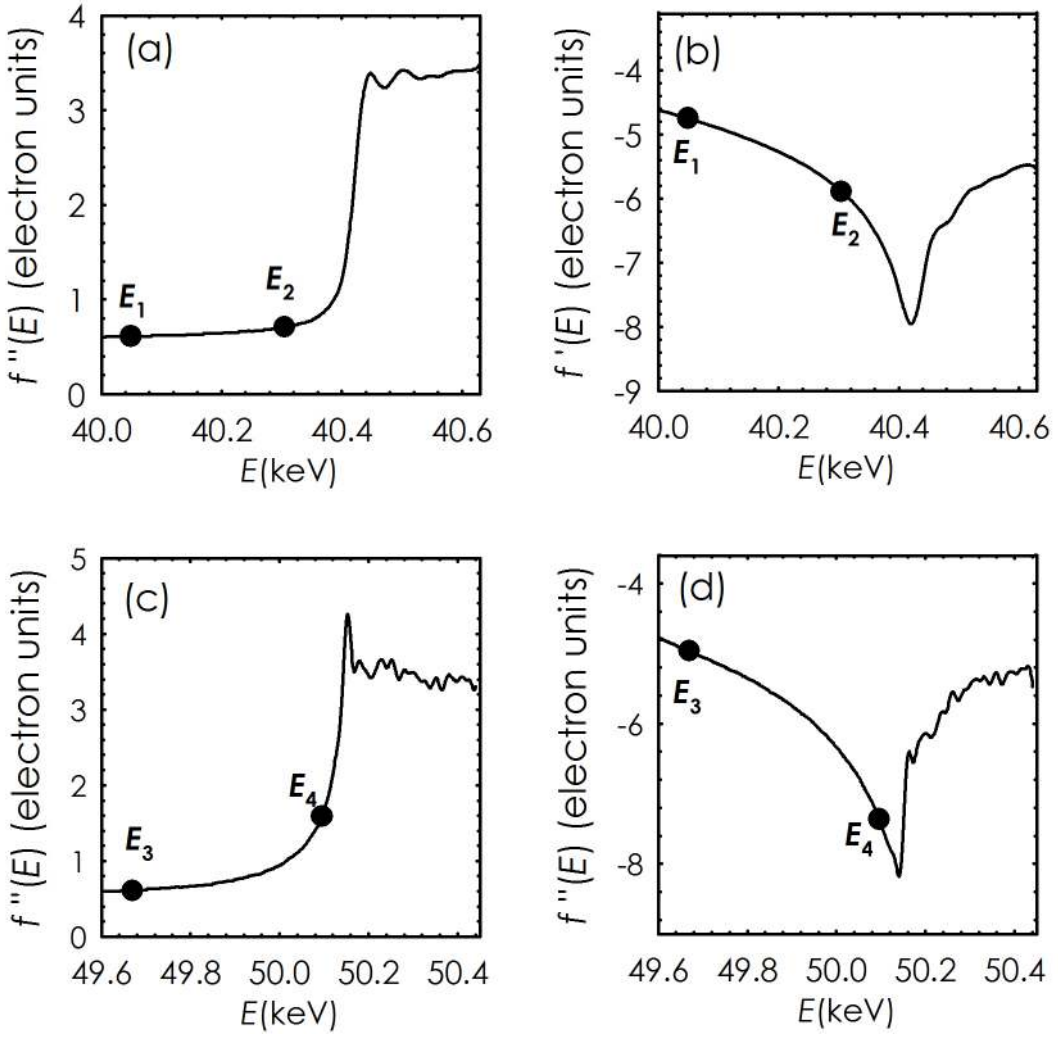

FIG.5.1 *Energy dependence of the real f'(E) and imaginary f''(E) part of the atomic X-ray scattering factor of CeO_2 near the Ce (a),(b) and Gd (c), (d) K-absorption edges. Solid lines are experimental data. The energies used in the anomalous scattering experiment are marked by dots.*

Figure 5.2 (*a*) shows the normalized coherent intensities after correction $I^{coh.}(Q,\lambda_1)$ and $I^{coh.}(Q,\lambda_2)$ for the a $Ce_{0.75}Gd_{0.25}O_{1.875}$ near the Ce *K*-edge taken as an example. In the related inset the *Q*-behaviours of the average mean-square scattering factors required to apply equation (5.5) are also displayed. The non dispersive part of $f(Q,\lambda)$ was calculated for each ion using the analytical formula suggested in Ref.10. By taking the difference between the two curves, as shown in Fig. 5.2 (*b*), the Ce related *DSF*(*Q*) was calculated according to equation (5.5) which can be Fourier transformed to obtained the DPDF Ce K-edge. The same procedure was applied to obtain the other DPDF.

In order to test the validity of this method for the CGO system, we performed PDF quality measurements as described in section 5.2.

In Fig.5.3 (*a*) the total PDFs obtained at λ_1 on pure CeO_2 and Gd_2O_3, respectively, are shown. The vertical dashed line centered on *r*~4.1Å indicates a *G*(*r*) peak related to Gd-Gd distances pertaining only to the C-type structure of pure Gd_2O_3.

Since this peak is absent in the CeO_2 fluoritic structure, it can be considered a clear fingerprint of the Gd contribution to the *G*(*r*) function. Figure 5.3 (*b*), (*c*) show the DPDF obtained at Ce and Gd K-edges for $Ce_{0.75}Gd_{0.25}O_{1.875}$, respectively together with the total PDF of the and CeO_2 and $Ce_{0.75}Gd_{0.25}O_{1.875}$ samples at λ_1. In both the panels, the peak at *r*~4.1 Å is present in the total PDF pertinent to the $Ce_{0.75}Gd_{0.25}O_{1.875}$ sample while it is completely absent in the DPDF Ce-K edge (Fig.5.3 (*b*)) and, in some way, it is seemed to be highlighted in the DPDF Gd-K edge (Fig.5.3 (*c*)).

In Fig. 5.4 (*a*) the total PDFs obtained on pure CeO_2 and Gd_2O_3 on a different *r* range are shown. The vertical dashed lines between $6<r<7$ Å again indicate *G*(*r*) peaks related only to interatomic distances belonging to C-type structure.

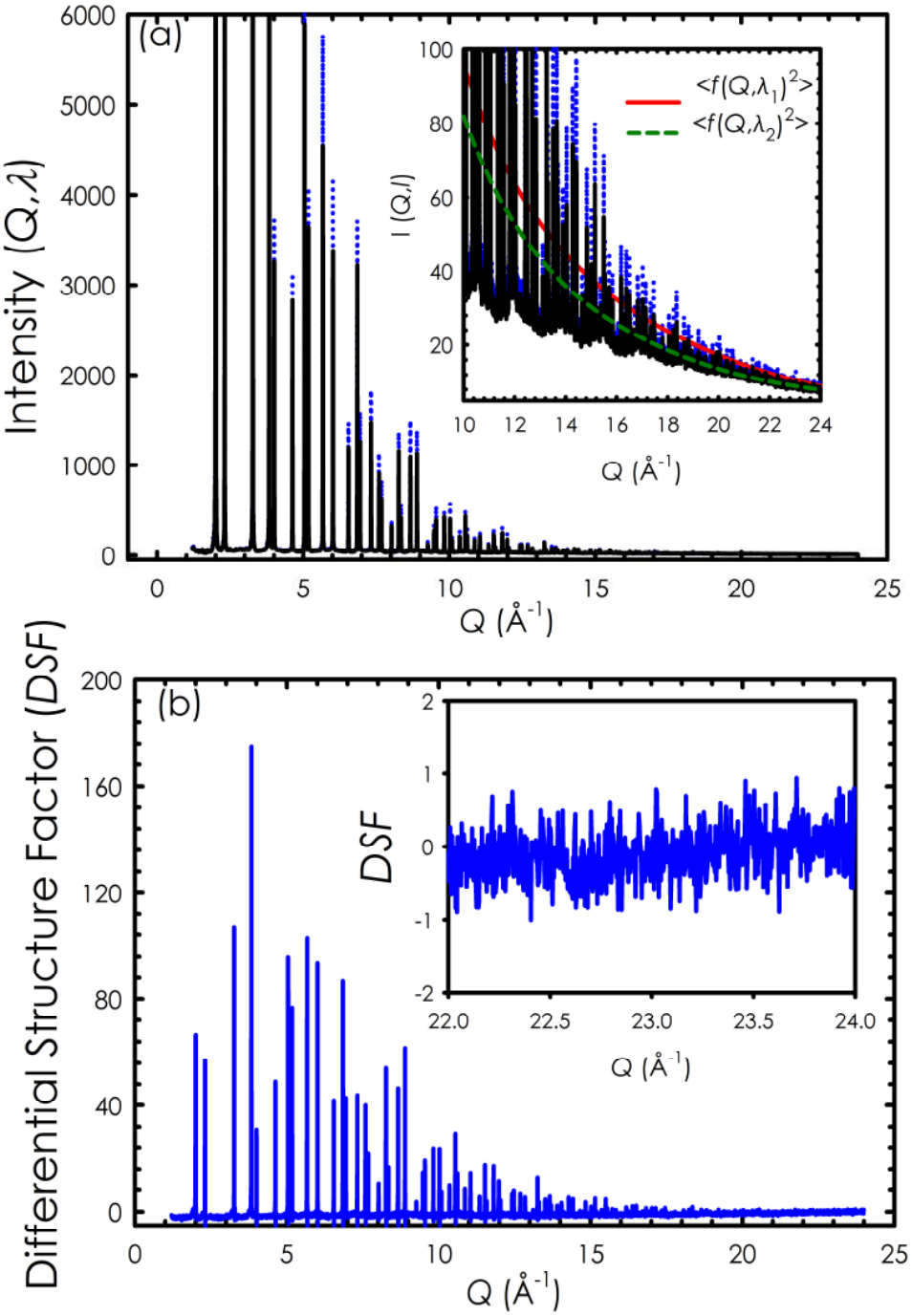

FIG.5.2 (*a*) *Comparison between normalized and corrected coherent I(Q,λ) data, as collected at* λ_1 *(dotted line) and* λ_2 *(solid line). In the inset: Q-dependence of the average mean square atomic scattering factors. (b) reduced Ce differential structure factor for* $Ce_{0.75}Gd_{0.25}O_{1.875}$. *The inset shows the high Q-region. The asymptotic behaviour of the DSF(Q) testifies the correctness of the normalization.*

Figure 5.4 (*b*), (*c*) show the DPDF obtained at Ce and Gd K-edges for $Ce_{0.5}Gd_{0.5}O_{1.75}$, respectively together with the total PDF of Gd_2O_3 and $Ce_{0.5}Gd_{0.5}O_{1.75}$ samples at λ_1.

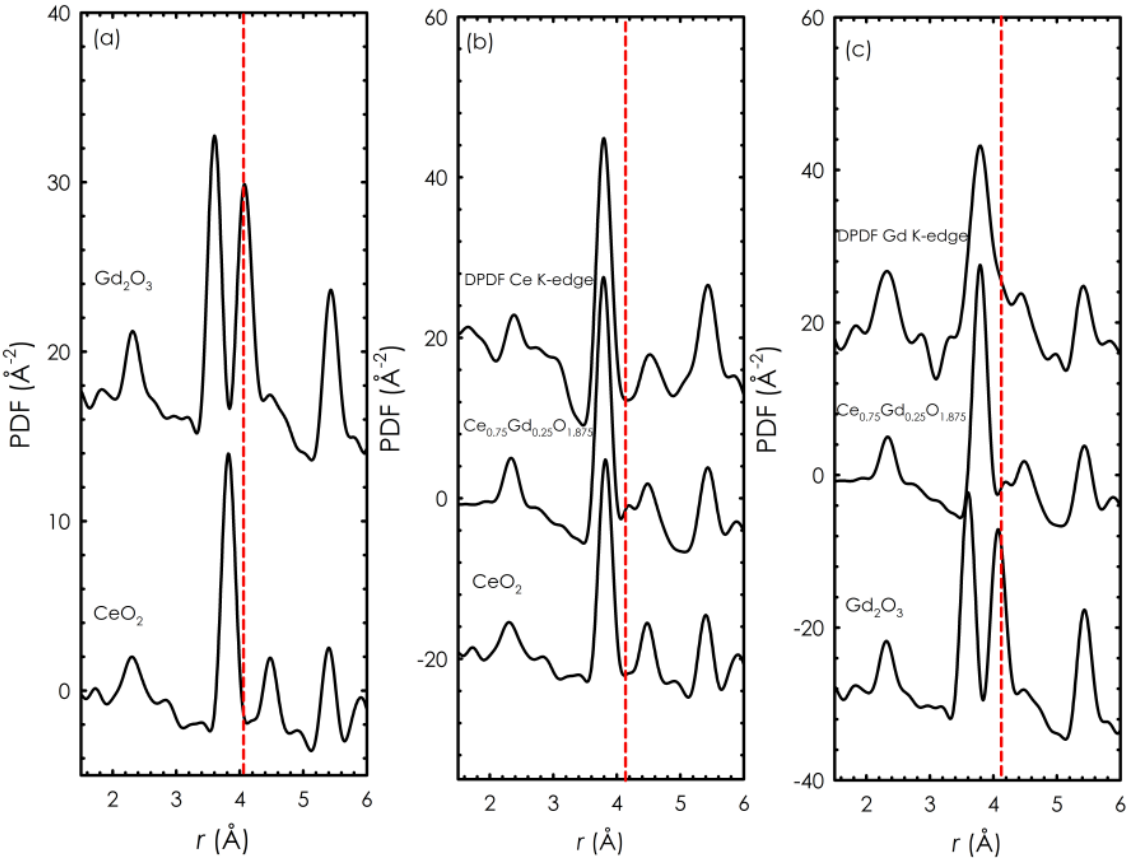

FIG.5.3 *(a) Total PDF for pure Gd_2O_3 (up) and CeO_2 (down). The vertical dashed line shows the C-type Gd-Gd distance. (b) Total (middle), DPDF Ce-K edge (up) for $Ce0_{.75}Gd_{0.25}O_{1.875}$. (c) Total (middle), DPDF Gd-K edge (up) for $Ce0_{.75}Gd_{0.25}O_{1.875}$. The total PDF for pure CeO_2 is also shown (bottom) in the panels together with the vertical line indicating again the same C-type Gd-Gd distance.*

In panel *(b)* the differential and the total PDF of the sample are very similar and, hence, we can say anything about the success of our signal extraction. On the other hand, the marked features belonging to the total PDF of Gd_2O_3 (bottom of Fig. 5.4 (*c*)) seem to

be completely emphasized in the DPDF Gd-K edge of $Ce_{0.5}Gd_{0.5}O_{1.75}$ (top of Fig. 5.4 (*c*)).

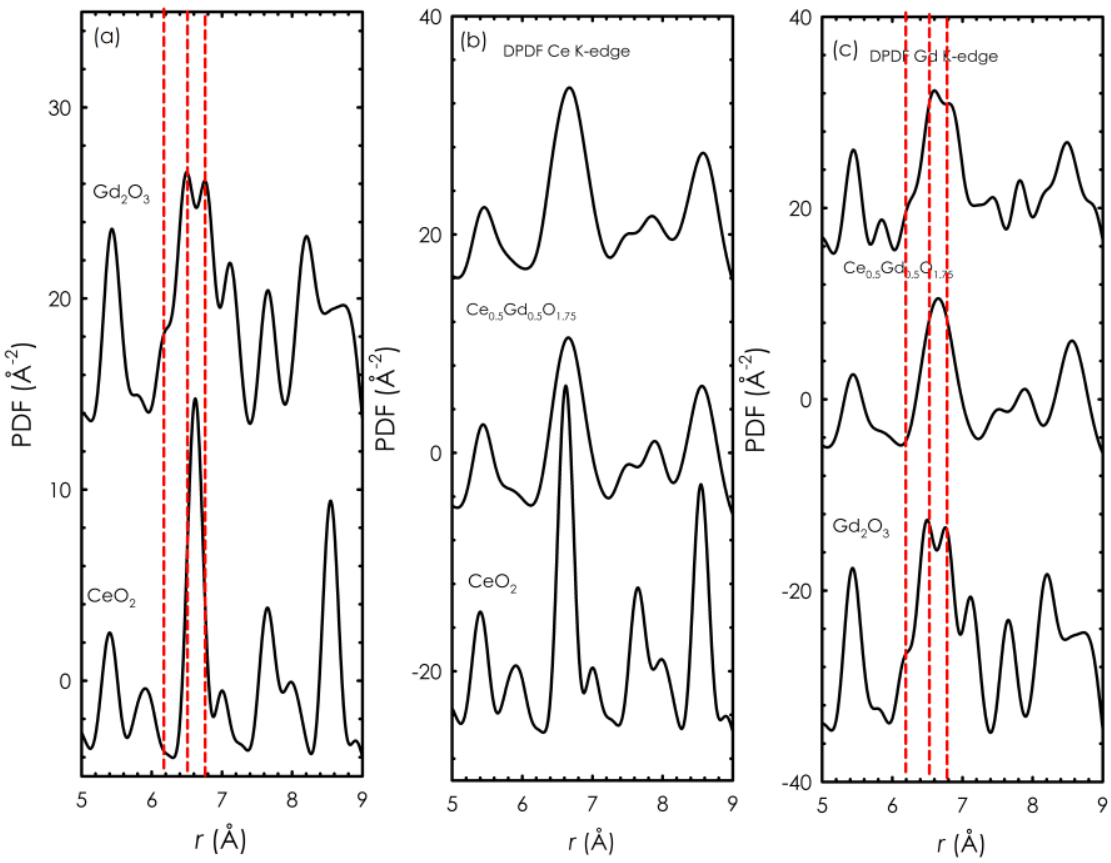

FIG.5.4 *(a) Total PDF for pure Gd_2O_3 (up) and CeO_2 (down). The vertical dashed lines show the C-type set distances. (b) Total (middle), DPDF Ce-K edge (up) for $Ce0.5Gd0.5O1.75$. (c) Total (middle), DPDF Gd-K edge (up) for $Ce0.5Gd0.5O1.75$. The total PDF for pure CeO_2 is also shown (bottom) in the panels together with the vertical lines indicating again the same C-type distances.*

According to equation (5.5), we can calculated partial structural factors related to Ce and Gd K-edges, $S_{Ce}(Q)$-1 and $S_{Gd}(Q)$-1, respectively:

$$S_{Ce}(Q)-1=W_{CeCe}\left[S_{CeCe}(Q)-1\right]+W_{CeGd}\left[S_{CeGd}(Q)-1\right]+W_{CeO}\left[S_{CeO}(Q)-1\right] \qquad (5.8)$$

$$S_{Gd}(Q)-1=W_{GdCe}\left[S_{GdCe}(Q)-1\right]+W_{GdGd}\left[S_{GdGd}(Q)-1\right]+W_{GdO}\left[S_{GdO}(Q)-1\right] \quad (5.9)$$

We noted that in equation (5.8), the partial structure factor [$S_{GdGd}(Q)$-1] is not involved in the $DSF(Q)$ Ce K-edge. Then, we expect than in the DPDF Ce K-edge the partial structure related to Gd-Gd does not contribute significantly to the $G(r)$ function. This is in agreement with our observation in Fig. 5.3 (*b*) confirming the reliability of the differential approach in providing element sensitive information. In addition, the [$S_{CeCe}(Q)$-1] is not present in the $DSF(Q)$ Gd K-edge (see equation (5.9)) so we expect a similar behavior in DPDF Gd K-edge of our samples. Actually, this is particularly true for the $DSF(Q)$ Gd K-edge of $Ce_{0.5}Gd_{0.5}O_{1.75}$. Indeed, since the Ce-Ce distance contributions are absent, the $G(r)$ features in some r range of DPDF Gd K-edge of $Ce_{0.5}Gd_{0.5}O_{1.75}$ (up Fig.5.4 (*c*)) are very similar to those present in total PDF of pure Gd_2O_3 (bottom Fig.5.4 (*c*))

As a final comment, by comparing the DPDF and the total PDF for pure CeO_2 and Gd_2O_3 a fairly good agreement is obtained in the r range shown in the Fig.5.2 and Fig.5.3. This provides evidence that Ce^{4+} and Gd^{3+} ions retain their local environment as in CeO_2 and Gd_2O_3 suggesting extended defect clusters (cationic compositional fluctuations) should occur in CGO materials.

5.5 Conclusion

We have discussed the applicability of the DPDF approach to the CGO system. PDF quality measurements have been performed at two different wavelengths close to the Ce *K*-edge and at two different wavelengths close to the Gs *K*-edge on $Ce_{0.75}Gd_{0.25}O_{1.875}$ and $Ce_{0.5}Gd_{0.5}O_{1.75}$ sample at 90 K. The comparison of the total with

the differential PDF of these sample reveals the disappearance and the appearance of peaks as predicted by element sensitive differential structure factors. The observations presented in this study support the idea that the differential approach can be successfully applied to this kind of samples.

References

[1] J. Goodenough, Ann. Rev. of Material Res. **33**, 91 (2003).

[2] T. S. Zhang, , J. Ma, L. B. Kong, S. H. Chan, J. A. Kilner, Solid State Ionics **170**, 209 (2004).

[3] H. Deguchi, H. Yoshida, T. Inagaki, M. Horiuchi, Solid State Ionics **176**, 1817 (2005).

[4] Y. Waseda, in *Novel Applications of Anomalous (Resonant) X-ray Scattering for Structural Characterization of Disordered Materials*, Springer, (1984).

[5] T. Egami, S. J. L. Billinge, in *Underneath the Bragg Peaks, Volume 16: Structural Analysis of Complex Materials*, Pergamon (2003).

[6] X. Qiu, J. W. Thompson, S. J. L. Billinge, J. Appl. Cryst. **37**, 678 (2004).

[7] H.E. Fischer, A. C. Barnes, Rep. Prog. Phys. **69**, 233 (2006).

[8] M. Saito, Y. Waseda, J. Synchrotron Radiation **7**, 152 (2000).

[9] M. Sánchez del Río, R. J. Dejus, 2004, *XOP 2.1: A new version of the X-ray optics software toolkit*, "Synchrotron Radiation Instrumentation: Eighth International Conference, edited by T. Warwick et al. (American Institute of Physics), pp 784-787.

[10] D. Waasmaier, A. Kirfel, Acta Cryst A **51**, 416 (1995).

Appendix A

Table A.1. *Exceptions to the systematic extinction conditions for the "orthorhombic" dataset (extracted from the output of the "Assign SpaceGroup" routine within the WinGX program package [L. J. Farrugia, J. Appl. Cryst. 32, 837 (1999)]). Cut1, Cut2, Cut3: number of data with I < 3, 6, 12 σ(I), respectively.*

Group	Cond.	Op.	All	Odd	Cut1	Cut2	Cut3	<I/σI>	Op. No.
h00	h=2n+1	21..	14	8	8	8	6	17.3	1
0k0	k=2n+1	.21.	14	8	8	8	6	17.8	2
00l	l=2n+1	..21	26	14	8	8	6	9.9	3
0kl	k=2n+1	b..	281	151	110	95	58	10.2	4
0kl	l=2n+1	c..		144	63	35	12	4.1	5
0kl	k+l=2n+1	n..		143	103	90	54	10.1	6
h0l	h=2n+1	.a.	281	151	114	95	61	9.9	7
h0l	l=2n+1	.c.		144	69	36	12	4.1	8
h0l	h+l=2n+1	.n.		143	105	89	57	9.9	9
hk0	h=2n+1	..a	158	82	82	82	53	15.8	10
hk0	k=2n+1	..b		82	82	82	54	15.9	11
hk0	h+k=2n+1	..n		80	80	80	45	14.1	12
hkl	k+l=2n+1	A..		1570	1142	976	607	10.2	13
hkl	h+l=2n+1	.B.		1571	1139	972	602	10.2	14
hkl	h+k=2n+1	..C		1421	987	812	421	8.5	15
hkl	h+k+l=2n+1	I		1387	915	768	420	8.3	16
hkl	not all odd/even	F		2281	1634	1380	815	9.7	17
h00	h=4n+1	41..		12	12	12	10	18.7	18
0k0	k=4n+1	.41.		12	12	12	10	19.2	19
00l	l=4n+1	..41		20	14	14	12	13.8	20
0kl	k+l=4n+1	d..		213	153	133	82	9.9	21
h0l	h+l=4n+1	.d.		213	157	131	84	9.8	22
hk0	h+k=4n+1	..d		117	117	117	76	15.4	23

Table A.2 *Values of the internal agreement factors under all Laue symmetries ("orthorhombic" dataset, extracted from the output of the "Assign SpaceGroup" routine within the WinGX program package [L. J. Farrugia, J. Appl. Cryst. 32, 837 (1999)]).*

R(int) values for merging under all Laue symmetries :
R(int) = Sum [|(F2(obs)- F2(mean)|] / Sum [F2(obs)]
Friedel pairs are always merged.
N(obs) & N(ind) only include those reflections with 2 or more observations
R1 includes redundancy factor n/(n-1) and may be up to 1.414 times greater than R(int)

Laue class	R(int)	N(obs)	N(ind)	R1	<n>
-1	0.021	2988	1404	0.028	2.128
2/m	0.028	2993	785	0.032	3.813
mmm	0.042	2994	456	0.044	6.566
4/m	0.043	2994	382	0.045	7.838
4/mmm	0.044	2990	258	0.045	11.589
-3(rhomb)	0.444	2993	817	0.486	3.663
-3m(rhomb)	0.445	2994	471	0.470	6.357
-3(hex)	0.276	2995	711	0.302	4.212
-3m1(hex)	0.278	2996	435	0.295	6.887
-31m(hex)	0.277	2996	411	0.292	7.290
6/m	0.278	2996	382	0.293	7.843
6/mmm	0.279	2996	258	0.289	11.612
m-3	0.468	2994	263	0.482	11.384
m-3m	0.468	2990	165	0.478	18.121
2/m 1 1	0.028	2993	785	0.032	3.813
1 1 2/m	0.038	2994	750	0.042	3.992

Highest diffraction symmetry with reasonable R(int) = 4/mmm
Highest diffraction symmetry compatible with cell metrics = 4/mmm

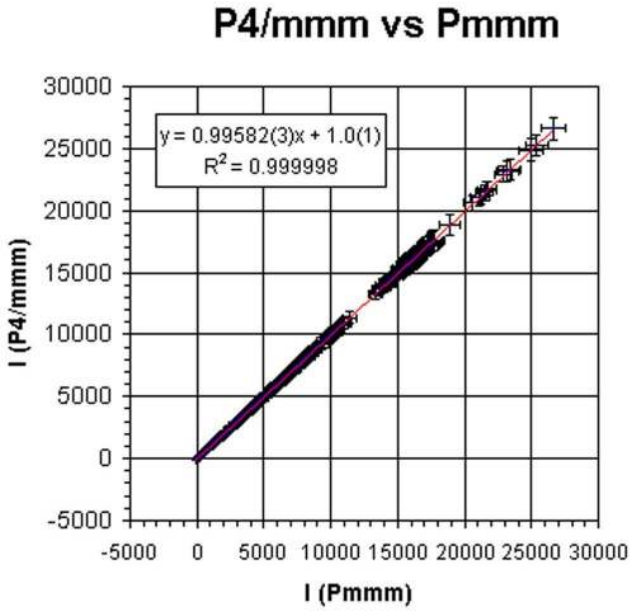

FIG. A.1 *Comparison between the net observed intensities (I) of "tetragonal" (P4/mmm) and "orthorhombic" (Pmmm) unmerged SCD datasets (2998 collected data). Corrections for crystal decay, absorption and Lorentz-polarization have been applied to both datasets. Inset: least-square parameters of the linear regression function. Error bars:* $\pm$ *1.0 estimated standard deviation.*

Table A.3 *Refined structural data of* $GdBaCo_2O_5$ *obtained at T=400K from synchrotron X ray powder diffraction. Space group is P4/mmm with refined lattice parameters a = 3.92144(1) Å and c = 7.53899(2) Å. The agreement factors are as large as* R_p*= 0.1006 and* $R(F^2)$*= 0.0489.*

Atom	*x*	*y*	z	U_{iso}
Gd	0.5000	0.5000	0.5000	0.00676(14)
Co	0.0000	0.0000	0.2568(1)	0.00686(16)
Ba	0.5000	0.5000	0.0000	0.00957(19)
O1	0.0000	0.0000	0.0000	0.0130(7)
O2	0.5000	0.0000	0.3083(4)	0.0130(7)

Appendix B

High quality XRPD patterns were collected at the ID31 beamline of the European Synchrotron Radiation Facility (ESRF) in Grenoble at λ=0.35422(1) Å.

Table B.1 *Refined structural parameters, Co-O bond distances and D_{ab} parameters for $GdBaCo_2O_{5+\delta}$ with δ=0.54(1) obtained at some selected temperatures. Space group Pmmm (#47). Atomic positions: Gd 2p (1/2 y 1/2), Ba 2o (1/2 y 0), $Co_{Oct.}$ 2r (0 1/2 z), $Co_{Pyr.}$ 2q (0 0 z), O1 1a (0 0 0), O2 1e (0 1/2 0), O3 1g (0 1/2 1/2), O4 1c (0,0,1/2) Occ.= 0.06, O5 2s (1/2 0 z), O6 2t (1/2 1/2 z), O7 4u(0 y z). The agreement factors R_p and $R(F^2)$ are also listed.*

	T=300K	*T*=350K	*T*=400K
a/Å	3.87892(2)	3.87439(2)	3.86070(2)
b/Å	7.83303(4)	7.84508(5)	7.86929(4)
c/Å	7.53685(4)	7.55078(5)	7.57389(4)
V/Å^3	228.997(3)	229.505(4)	230.103(3)
Gd *y*	0.27309(9)	0.2712(1)	0.26883(8)
Ba *y*	0.24999(9)	0.2495(1)	0.24910(9)
$Co_{Oct.}$ *z*	0.2523(3)	0.2513(3)	0.2523(2)
$Co_{Pyr.}$ *z*	0.2554(3)	0.2551(3)	0.2556(2)
O5 *z*	0.308(1)	0.312(1)	0.3140(9)
O6 *z*	0.273(1)	0.272(1)	0.2714(9)
O7 *y*	0.2423(6)	0.2399(8)	0.2390(6)
O7 *z*	0.2924(6)	0.2955(7)	0.2955(5)
R_p	0.0921	0.1087	0.0859
$R(F^2)$	0.0512	0.0524	0.0414
$Co_{Oct.}$-O2	1.9013(22)	1.8972(23)	1.9107(18)
$Co_{Oct.}$-O3	1.8672(22)	1.8782(23)	1.8763(18)
$Co_{Oct.}$-O6(*a*)	1.9456(7)	1.9434(8)	1.9358(6)
$Co_{Oct.}$-O7(*b*)	2.041(5)	2.0670(6)	2.0800(5)
D_{ab}/Å	0.0954(57)	0.1236(68)	0.1442(56)
$Co_{Pyr.}$-O1	1.9248(21)	1.9263(23)	1.9354(18)
$Co_{Pyr.}$-O5(*a*)	1.9802(16)	1.9848(19)	1.9806(16)
$Co_{Pyr.}$-O7(*b*)	1.9190(5)	1.9070(6)	1.9050(5)
D_{ab}/Å	0.0612(66)	0.0778(66)	0.0756(66)

Table B.2 *Refined structural parameters, Co-O bond distances and D_{ab} parameters for $GdBaCo_2O_{5+\delta}$ with δ=0.57(1) obtained at some selected temperatures. Space group Pmmm (#47). Atomic positions: Gd 2p (1/2 y 1/2), Ba 2o (1/2 y 0), $Co_{Oct.}$ 2r (0 1/2 z), $Co_{Pyr.}$ 2q (0 0 z), O1 1a (0 0 0), O2 1e (0 1/2 0), O3 1g (0 1/2 1/2), O4 1c (0,0,1/2) Occ.= 0.14, O5 2s (1/2 0 z), O6 2t (1/2 1/2 z), O7 4u(0 y z). The agreement factors R_p and $R(F^2)$ are also listed.*

	T=300K	*T*=320K	*T*=350K	*T*=380K	*T*=400K
a/Å	3.87864(1)	3.87706(1)	3.86343(1)	3.86369(1)	3.86412(2)
b/Å	7.82859(3)	7.83336(3)	7.85333(3)	7.85676(3)	7.86002(6)
c/Å	7.54085(2)	7.54669(3)	7.56837(2)	7.57171(2)	7.57488(5)
V/Å^3	228.973(2)	229.197(2)	229.631(2)	229.847(2)	230.065(4)
Gd *y*	0.27133(8)	0.27054(8)	0.26825(8)	0.26809(8)	0.26808(9)
Ba *y*	0.24996(8)	0.24972(9)	0.24930(1)	0.24945(9)	0.24948(9)
$Co_{Oct.}$ *z*	0.2520(2)	0.2517(3)	0.2523(2)	0.2523(2)	0.2524(2)
$Co_{Pyr.}$ *z*	0.2549(2)	0.2555(2)	0.2551(2)	0.2549(2)	0.2549(2)
O5 *z*	0.3114(8)	0.3111(9)	0.3121(9)	0.3123(9)	0.3120(9)
O6 *z*	0.2721(9)	0.273(1)	0.2722(9)	0.2721(9)	0.2729(9)
O7 *y*	0.2425(6)	0.2405(6)	0.2401(6)	0.2415(6)	0.2409(7)
O7 *z*	0.2935(5)	0.2929(6)	0.2945(5)	0.2955(5)	0.2948(5)
R_p	0.0815	0.0857	0.0769	0.0750	0.0776
$R(F^2)$	0.0342	0.0383	0.0365	0.0414	0.0423
$Co_{Oct.}$-O2	1.9004(18)	1.9005(19)	1.9005(17)	1.9106(18)	1.9120(19)
$Co_{Oct.}$-O3	1.8700(18)	1.8728(19)	1.8739(17)	1.8753(18)	1.8754(19)
$Co_{Oct.}$-O6(*a*)	1.9453(6)	1.9452(7)	1.9379(6)	1.9376(6)	1.9383(6)
$Co_{Oct.}$-O7(*b*)	2.040(5)	2.054(5)	2.059(5)	2.057(5)	2.062(5)
D_{ab}/Å	0.0947(56)	0.1088(57)	0.1211(56)	0.1194(56)	0.1237(56)
$Co_{Pyr.}$-O1	1.9227(17)	1.9284(19)	1.9312(14)	1.9301(18)	1.9315(18)
$Co_{Pyr.}$-O5(*a*)	1.9854(14)	1.9835(16)	1.9790(14)	1.9802(15)	1.9799(16)
$Co_{Pyr.}$-O7(*b*)	1.921(5)	1.907(5)	1.916(5)	1.922(5)	1.917(5)
D_{ab}/Å	0.0644(64)	0.0765(66)	0.0630(64)	0.0582(65)	0.0629(66)

Table B.3 *Refined structural parameters, Co-O bond distances and D_{ab} parameters for $GdBaCo_2O_{5+\delta}$ with δ=0.63(1) obtained at some selected temperatures. Space group Pmmm (#47). Atomic positions: Gd 2p (1/2 y 1/2), Ba 2o (1/2 y 0), $Co_{Oct.}$ 2r (0 1/2 z), $Co_{Pyr.}$ 2q (0 0 z), O1 1a (0 0 0), O2 1e (0 1/2 0), O3 1g (0 1/2 1/2), O4 1c (0,0,1/2) Occ.= 0.26, O5 2s (1/2 0 z), O6 2t (1/2 1/2 z), O7 4u(0 y z). The agreement factors R_p and $R(F^2)$ are also listed.*

	T=300K	*T*=350K	*T*=400K
a/Å	3.87981(8)	3.87436(2)	3.87498(2)
b/Å	7.80240(2)	7.81847(5)	7.82617(5)
c/Å	7.55551(2)	7.56980(4)	7.57849(4)
V/Å^3	228.725(1)	229.301(4)	229.827(4)
Gd *y*	0.26518(7)	0.2646(1)	0.26442(9)
Ba *y*	0.24976(8)	0.2496(1)	0.2496(1)
$Co_{Oct.}$ *z*	0.2524(2)	0.2522(2)	0.2526(2)
$Co_{Pyr.}$ *z*	0.2542(2)	0.2539(2)	0.2542(2)
O5 *z*	0.3086(8)	0.3099(9)	0.3103(9)
O6 *z*	0.2706(8)	0.271(1)	0.271(1)
O7 *y*	0.2401(6)	0.2406(7)	0.2411(7)
O7 *z*	0.2904(5)	0.2900(5)	0.2910(5)
R_p	0.0675	0.0821	0.0785
$R(F^2)$	0.0331	0.0397	0.0404
$Co_{Oct.}$-O2	1.9070(15)	1.9092(1)	1.9143(19)
$Co_{Oct.}$-O3	1.8708(15)	1.8757(19)	1.8750(19)
$Co_{Oct.}$-O6(*a*)	1.9448(5)	1.9427(6)	1.9424(6)
$Co_{Oct.}$-O7(*b*)	2.048(3)	2.048(6)	2.047(6)
D_{ab}/Å	0.1032(45)	0.1053(66)	0.1046(66)
$Co_{Pyr.}$-O1	1.9210(15)	1.9217(19)	1.9263(19)
$Co_{Pyr.}$-O5(*a*)	1.9830(13)	1.9830(16)	1.9835(16)
$Co_{Pyr.}$-O7(*b*)	1.894(3)	1.901(6)	1.908(6)
D_{ab}/Å	0.0890(53)	0.0820(76)	0.0755(76)

Pubblications

Mattia Allieta

M. Allieta, M. Scavini, L. Spalek, V. Scagnoli, H. C. Walker, C Panagopoulos, S. Saxena, T. Katsufuji, and C. Mazzoli, On the role of intrinsic disorder in the structural phase transition of magnetoelectric $EuTiO_3$, *Physical Review B*, submitted.

M. Allieta, C. Oliva, M. Scavini, S. Cappelli, E. Pomjakushina, and V. Scagnoli, Spin – lattice interaction in the insulator to metal transition of $GdBaCo_2O_{5+\delta}$, *Physical Review B*, accepted.

L. Lo Presti, M. Allieta, M. Scavini, P. Ghigna, L. Loconte, V. Scagnoli, M Brunelli, Crystal structure and structural phase transitions in the $GdBaCo_2O_{5.0}$ cobaltite, *Physical Review B* **84**, 104107 (2011).

M. Coduri, M. Scavini, M. Allieta, M. Brunelli, and C. Ferrero, Local disorder in yttrium doped ceria ($Ce_{1-x}Y_xO_{2-x/2}$) probed by joint X-ray and Neutron Powder Diffraction, *Journal of Physics: Conference Series*, accepted.

M. Allieta, M. Brunelli, M. Coduri, M. Scavini, and C. Ferrero, Differential Pair Distribution Function applied to $Ce_{1-x}Gd_xO_{2-x/2}$ system, *Zeitschrift für Kristallographie Proceedings* **1**, 15 (2011).

M. Scavini, M. Coduri. M. Allieta. L. Mollica, M. Brunelli, L. Malavasi, A. Lascialfari, and C. Ferrero, Effect of Local Disorder on the Transport Properties of Al-Doped $SmBa_2Cu_3O_{6+\delta}$ Superconductors, *Journal of Physical Chemistry C* **114**, 19509 (2010)

O. Bucheneva, I. Rossetti, C. Oliva, M. Scavini, S. Cappelli, B. Sironi, M. Allieta, A. Kryukov, and L. Forni, Effective Ag doping and resistance to sulfur poisoning of La-Mn perovskites for the catalytic flameless combustion of methane, *Journal of Materials Chemistry* **20**, 10021 (2010).

O. Bucheneva, I. Rossetti, C. Biffi, M. Allieta, A. Kryukov, and N. Lebedeva, La-Ag-Co perovskites for the catalytic flameless combustion of methane, *Applied Catalysis A-General* **370**, 24 (2009).